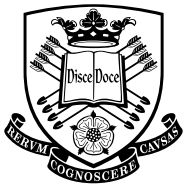

The University Of Sheffield.

Thin AlGaAsSb Avalanche Photodiodes with Low Excess Noise

L. L.G. Pinel

A thesis submitted in partial fulfilment of the requirements for the degree of

Doctor of Philosophy

The University of Sheffield

Faculty of Engineering

Department of Electronic and Electrical Engineering

November 2018

The University Of Sheffield.

Thin AlGaAsSb Avalanche Photodiodes with Low Excess Noise

By:

Lucas Laurent Gaston Pinel

A thesis submitted in partial fulfilment of the requirements for the degree of Doctor of Philosophy

The University of Sheffield
Faculty of Engineering
Department of Electronic and Electrical Engineering

1st November 2018

C’est là un bien grand mystère. Pour vous qui aimez aussi le petit prince, comme pour moi, rien de l’univers n’est semblable si quelque part, on ne sait où, un mouton que nous ne connaissons pas a, oui ou non, mangé une rose…

Regardez le ciel. Demandez-vous : le mouton oui ou non a-t-il mangé la fleur ? Et vous verrez comme tout change…

Antoine de Saint-Exupéry, *Le Petit Prince* (1943)

Contents

Acknowledgements

I would like to express my sincere gratitude to Prof Jo Shien Ng, and Prof Chee Hing Tan for their guidance and support throughout my PhD years.

I would like to thank my fellow PhD students, Salman Abdullah, Jonathan Petticrew, Vladimir Shulyak, Leh Woon Lim, and Xin Yi for their constant presence and kindness during the many hours spent in the laboratory.

This work would not have been possible without the wafers provided by the National Epitaxy Facility. The wafers used for the work presented in this thesis were grown by Dr Shiyong Zhang, whose expertise as grower is greatly appreciated.

I am greatly indebted to the European Commission, through its Marie Curie-Skłodowska Actions for funding this PhD, and allowing me to be part of this truly enriching experience. I also deeply appreciate the friendship of the other ESRs and member of the PROMIS consortium. I was lucky to travel to all corners of Europe to meet fifteen truly exceptional people from all over the planet.

My gratitude is extended to Dr Simon Dimler, Dr Anton Velychko, and Stephen Dorward for their kind support and advice in the laboratory.

I also wish to thank Dr Xinxin Zhou and Dr Xiao Meng for teaching me many experimental and analysis techniques that have come in handy during my PhD years.

Finally, special thanks should be given to my friends and family, especially to my parents for their unfaltering support during all my years of studies. This work is dedicated to all these people that have believed in me and without whom I would not be where I am today.

Abstract

In photon-starved or high-speed applications, such as optical communications or medical imaging, where detection of weak light signals is required, avalanche photodiodes (APDs) are widely used. APDs with thin avalanche regions have shown low excess noise characteristics and high gain-bandwidth products.

In this work, gain and excess noise of thin $Al_{0.85}Ga_{0.15}As_{0.56}Sb_{0.44}$ (lattice-matched to InP substrates) *p-i-n* and *n-i-p* diodes with 100 and 200 nm avalanche regions have been measured for different carrier injection conditions. Very low excess noise values were obtained in *p-i-n* devices under pure electron injection, with effective ionisation ratios $k_{eff} = 0.08 - 1$. The AlGaAsSb electron ionisation coefficient, α, was found to be higher than the hole ionisation coefficient, β. A significant dead-space effect has been observed in such thin layers, reducing the excess noise. Recurrence equations were used to extract the ionisation coefficients and ionisation threshold energies for the electrons and holes in AlGaAsSb.

In addition, simulations using recurrence equations were carried out to simulate gain and excess noise characteristics in *p-i-n* diodes with $k_{eff} = 0.1$, 0.01, and 0.001, for different light injection profiles. $F(M)$ characteristics were found to be higher for mixed injection conditions than for pure electron injection. However, for extremely low k_{eff} materials, excess noise remains low up to large gain values even for the most severe cases of mixed injection. Randomly-generated ionisation path lengths (RPL) simulations were also carried out to track the carriers initiating impact ionisation, and the sharp increase in $F(M)$ characteristics was attributed to an increase in the number of hole-initiated ionisation events. Signal-to-noise (SNR) and noise-equivalent power (NEP) were calculated for APDs with $k_{eff} = 0.1$, 0.01, and 0.001, highlighting the interest of using avalanche gain to increase the sensitivity of optical detectors.

Finally, a Separate Absorption and Multiplication (SAM) APD combining a

100 nm-thin AlGaAsSb avalanche region and a 1 μm InGaAs absorption region has been studied. Low dark currents and good photoresponse at 1550 nm wavelength have been demonstrated. The temperature dependence of gain was investigated for temperatures between 77 K and room temperature, and a temperature coefficient of breakdown voltage, C_{bd}, of -49 mV/K was obtained.

List of Publications

Journal publications

1. Xinxin Zhou, **Lucas L.G. Pinel**, Simon J. Dimler, Shiyong Zhang, Jo Shien Ng, and Chee Hing Tan, "Thin $Al_{1-x}Ga_xAs_{0.56}Sb_{0.44}$ diodes with low excess noise", *IEEE Journal of Selected Topics in Quantum Electronics*, vol. 24, no. 2, p. 3800105, Mar./Apr. 2018.

2. Salman Abdullah, Chee Hing Tan, Xinxin Zhou, Shiyong Zhang, **Lucas Pinel**, and Jo Shien Ng, "Investigation of temperature and temporal stability of AlGaAsSb avalanche photodiodes", *Optics Express*, vol. 25, no. 26, pp. 33610–33616, Dec. 2017.

3. **Lucas L.G. Pinel**, Simon J. Dimler, Xinxin Zhou, Salman Abdullah, Shiyong Zhang, Chee Hing Tan, and Jo Shien Ng, "Effects of carrier injection profile on low noise thin $Al_{0.85}Ga_{0.15}As_{0.56}Sb_{0.44}$ avalanche photodiodes", *Optics Express*, vol. 26, no. 3, pp. 3568–3576, Feb. 2018.

Open datasets

1. Xinxin Zhou, **Lucas Pinel**, Simon J. Dimler, Shiyong Zhang, Jo Shien Ng, and Chee Hing Tan, "Data for paper: Thin $Al_{1-x}Ga_xAs_{0.56}Sb_{0.44}$ diodes with low excess noise", *Figshare*, Jul. 2017, DOI: 10.15131/shef.data.5155822.

2. Salman Abdullah, Chee Hing Tan, Xinxin Zhou, Shiyong Zhang, **Lucas Pinel**, and Jo Shien Ng, "Data for paper: Investigation of temperature and temporal stability of AlGaAsSb avalanche photodiodes", *Figshare*, Jan. 2018, DOI: 10.15131/shef.data.5729079.

3. **Lucas Pinel**, Simon Dimler, Xinxin Zhou, Salman Abdullah, Shiyong Zhang, Chee Tan, and Jo Ng, "Data for paper: Effects of carrier injection profile on low noise thin $Al_{0.85}Ga_{0.15}As_{0.56}Sb_{0.44}$ avalanche photodiodes", *Figshare*, Jan. 2018, DOI: 10.15131/shef.data.5787318.

Conference talks

1. **Lucas L.G. Pinel**, Chee Hing Tan, Simon J. Dimler, Xinxin Zhou, Shiyong Zhang, and Jo Shien Ng, "Excess noise factors of thin $Al_{0.85}Ga_{0.15}As_{0.56}Sb_{0.44}$ diodes", UK Semiconductors, Sheffield, UK, Jul. 2017.

2. Salman Abdullah, Chee Hing Tan, **Lucas Pinel**, and Jo Shien Ng, "Temperature and temporal stability of avalanche gain for $Al_{0.85}Ga_{0.15}As_{0.56}Sb_{0.44}$

avalanche photodiodes", Semiconductor and Integrated Optoelectronics Conference, Cardiff, UK, Mar. 2018.

3. **Lucas L.G. Pinel**, Chee Hing Tan, and Jo Shien Ng, "Effect of carrier injection profile on avalanche noise characteristics", UK Semiconductors, Sheffield, UK, Jul. 2018.

4. **Lucas L.G. Pinel**, Chee Hing Tan, and Jo Shien Ng, "Investigation of avalanche properties of thin AlGaAsSb avalanche layers", Photonics by the Lake, Windermere, UK, Jul. 2018.

5. Salman Abdullah, Chee Hing Tan, **Lucas L.G. Pinel**, and Jo Shien Ng, "$Al_{0.85}Ga_{0.15}As_{0.56}Sb_{0.44}$ avalanche photodiodes with high immunity to temperature fluctuation", SPIE Optics + Photonics, San Diego, CA, USA, Aug. 2018.

Poster presentations

1. **Lucas L.G. Pinel**, Jonathan Petticrew, Xinxin Zhou, Salman Abdullah, Chee Hing Tan, and Jo Shien Ng, "Improving Wet Etching of InGaAs/AlGaAsSb Avalanche Photodiodes", 19th International Conference on Molecular Beam Epitaxy, Montpellier, France, Sep. 2016.

2. Salman Abdullah, **Lucas Pinel**, Chee Hing Tan, Jo Shien Ng, "Determining The Capacitance of Diodes with High Leakage Currents", 19th International Conference on Molecular Beam Epitaxy, Montpellier, France, Sep. 2016.

3. **Lucas L.G. Pinel**, Chee Hing Tan, and Jo Shien Ng, "Study of avalanche statistics in very low noise AlGaAsSb APDs using a multi-channel analyzer", SPIE Optics + Photonics, San Diego, CA, USA, Aug. 2018.

List of Acronyms and Symbols

Acronyms

APD	Avalanche Photodiode
CCD	Charge-Coupled Device
DUT	Device Under Test
FWHM	Full Width at Half Maximum
GBP	Gain-Bandwidth Product
LIA	Lock-in Amplifier
MBE	Molecular Beam Epitaxy
NEP	Noise-Equivalent Power
PDF	Probability Density Function
PECVD	Plasma-Enhanced Chemical Vapour Deposition
PMT	Photomultiplier Tube
RPL	Randomly-generated ionisation Path Lengths
SAM APD	Separate Absorption and Multiplication Avalanche Photodiode
SIMS	Secondary-Ion Mass Spectrometry
SMU	Source–Measurement Unit
SNR	Signal-to-Noise Ratio
TIA	Transimpedance Amplifier
TRIM	Transport of Ions in Matter

Symbols

A	Area of a diode

α	Ionisation coefficient of electrons
α^*	Effective (or enabled) ionisation coefficient of electrons
B_{eff}	Equivalent noise bandwidth
β	Ionisation coefficient of holes
β^*	Effective (or enabled) ionisation coefficient of holes
C	Capacitance
C_{bd}	Temperature coefficient of breakdown voltage
d	Dead-space value
d_e	Dead-space value for electrons
d_h	Dead-space value for holes
E	Electric field
E_g	Semiconductor bandgap
ε	Dielectric permittivity of semiconductor
$E_{th,e}$	Ionisation threshold energy for electrons
$E_{th,h}$	Ionisation threshold energy for holes
F	Avalanche excess noise factor
g	Avalanche gain for one absorption event
h	Planck constant
I	Current
I_d	Dark current of a diode
I_{diff}	Diffusion current
$I_{g\text{-}r}$	Generation recombination current
I_{ph}	Primary photocurrent of a diode
I_{pr}	Primary (unmultiplied) photocurrent of a diode
I_s	Saturation current of a diode
I_{tot}	Total current of a diode (dark + photocurrent)
I_{tunn}	Tunnelling current
J_b	Bulk dark current density of a diode
J_s	Surface dark current density of a diode

k	Ionisation rate ratio
k_B	Boltzmann constant
k_{eff}	Effective ionisation ratio
k_N	Excess noise setup calibration factor
λ	Light wavelength
M	Avalanche gain of a diode
n	Diode ideality factor
N	Density of charges
n_{amp}	Current-noise spectral density of amplifier
N_{APD}	Total APD shot noise power
n_e	Number of electron-induced impact ionisation events
n_h	Number of hole-induced impact ionisation events
n_i	Intrinsic carrier concentration
N_s	Unity gain shot noise power
P	Perimeter of a diode mesa
P_0	Incident light power
q	Electronic charge
R	Responsivity
R_s	Series resistance of a diode
T	Temperature
V	Voltage
V_b	Avalanche breakdown voltage
V_p	Punch-through voltage
w	Width of avalanche region
W	Depletion width of a diode

List of Figures

List of Tables

Chapter 1

Introduction

1.1 Motivations

Rising demands for optical communications have driven the need for ultra-fast optical receivers, able to detect very weak light signals. For optical communications, electrical signals are converted into light signals by an optical transmitter, and sent into optical fibres, made of silica (glass), over very long distances. At the other end, signals are detected by optical receivers and converted back into electrical signals. The optical losses of silica are minimum at 1310 (minimal dispersion loss) and 1550 nm (minimal absorption loss), making these the two wavelengths of choice for optical communications. The optical receiver includes an essential component, a photodetector, to convert the optical signal back into electrical signal. An ideal photodetector for long-range optical communications should have high sensitivity to light, fast response (high bandwidth), and low noise at the wavelengths of interest. Different types of photodetectors exist, with different advantages and drawbacks.

To detect low levels of light, Photomultiplier Tubes (PMTs) are often used. They are vacuum tubes in which incident photons eject electrons from a photocathode. Those electrons are then accelerated by a large electric field, and focussed on a series of dynodes, producing more and more electrons at each stage. PMTs offer a good detection sensitivity and can exhibit fairly high gains, lowering or even suppressing the need for amplification, thus reducing the noise. However, they need to be operated at very high voltages, which can be impractical for some applications. They are also bulky and sensitive to stray magnetic fields. They have

been replaced by semiconductor-based alternatives in most applications, including optical communications.

Semiconductors offer a very efficient and flexible alternative to PMTs. There are several types of such detectors, namely Charge-Coupled Devices (CCDs), *p-i-n* diodes and Avalanche Photodiodes (APDs). They all rely on the photoelectric effect, which consist in the creation of electron-hole pairs inside the material upon absorption of a photon. The significant advantage of APDs compared to other semiconductors detectors is that APDs exhibit internal gain, due to the impact ionisation phenomenon. This allows sensitive detection of photons, and suppresses the need for external amplifier, bringing therefore the system noise level down. APDs are also relatively cheap to produce and down-scalable to be included into integrated circuits.

The interest therefore lies in designing APDs combining all the desirable properties offered by semiconductor materials, to achieve good sensitivity and high speed. An ideal APD would have a good absorption efficiency, low dark current (dependent on the semiconductor bandgap and material quality), and good avalanche characteristics (low noise, temperature stability). These characteristics impose different, even conflicting requirements on the materials composing the diode, hence calling for a design where the absorption and the avalanche regions are separated, the so-called Separate Absorption and Multiplication Avalanche Photodiodes (SAM APDs).

The technology for commercial APDs is currently dominated by silicon detectors. They benefit from matured wafer growth and device fabrication maturity, enabling the mass production of thick, low-defect devices. However, silicon has an indirect bandgap, hence suffers from a low absorption efficiency if the photon energy is close to its bandgap. This means a detector thickness of several micrometres is necessary to achieve reasonable efficiency at wavelengths above the visible range. In addition, Si does not absorb at the optical communication wavelengths. The current trend is to develop thinner, faster diodes, ideally with a sub-micrometre multiplication region. To achieve this, it has been necessary to investigate other materials. III-V materials are also popular as they offer a large flexibility in the range of bandgaps and lattice constants. Among the very wide variety of such compounds, some of them are more relevant for designing low-noise APDs. A detailed review is carried out in Chap. 2.

So the motivations are clear, semiconductor researchers are looking for very low noise materials, exhibiting good avalanche characteristics, to design fast, efficient devices. These avalanche materials can then be combined with suitable absorption materials to detect photons at the wavelength of interest. As will be detailed in the following chapters, thin avalanche layers help to ensure low noise, and high speeds in APDs. Extensive research has therefore been carried out on novel materials capable of yielding low noise when used in thin avalanche layers. Among them, $Al_{0.85}Ga_{0.15}As_{0.56}Sb_{0.44}$ (thereafter referred as AlGaAsSb throughout this thesis) is particularly promising. Advantages of using thin AlGaAsSb layers to design low-noise APDs are presented in Chap. 2. For such low-noise materials however, how the light absorption profile and carrier injection conditions affect the gain and noise of APDs has not been extensively studied. In addition, for optimal efficiency, these low noise avalanche layers have to be coupled with absorption layers tailored to the wavelength of interest. This work is important since APDs have numerous applications besides optical communications, including medical imaging, light detection and ranging (LIDAR), and atmospheric pollution monitoring.

Areas requiring study have therefore been identified from the motivations described above. A detailed study of gain and excess noise in thin AlGaAsSb APDs is necessary to fully understand the avalanche characteristics of this novel material. Theoretical and simulation work is needed to investigate how carrier injection profiles affects the gain and noise of such devices. Finally, an experimental study of the performance of SAM APDs combining a thin AlGaAsSb multiplication layer and an InGaAs absorption region for efficient detection at 1550 nm wavelength has to be carried out.

1.2 Thesis structure

This work will study excess noise of a novel avalanche material, AlGaAsSb, that offers promising characteristics when used in thin multiplication layers. Simulations will be carried out to study the influence of light injection profile in low noise avalanche materials. Finally, a SAM APD comprising a thin AlGaAsSb avalanche layer coupled with InGaAs, a good absorber for the wavelengths used in optical

telecommunications, will be studied. The structure of the thesis is detailed below.

Chapter 2 presents a literature review on low-noise APDs and the background necessary to understand the motivations of this thesis.

In Chapter 3, the experimental techniques and setups that are used for the characterisation of the devices are described. These include current-voltage (I-V), capacitance-voltage (C-V), and low temperature measurements. The procedure to carry out the gain and excess noise measurements shown in Chapter 4 are also detailed. Finally, the recurrence equations used for simulations of gain and excess noise are presented.

Chapter 4 reports on the very low excess noise values obtained in thin AlGaAsSb p-i-n and n-i-p diodes. 100 and 200 nm-thin AlGaAsSb APDs are studied. Fabrication and electrical as well as material characterisation of the devices are detailed. Gain and excess noise are measured under several injection conditions, including pure electron or hole injection and mixed injection. The measured excess noise values are competitive with the best materials reported in literature. Finally, recurrence equations are used to extract the important impact ionisation parameters for AlGaAsSb, namely the ionisation coefficients and ionisation threshold energies for the electrons and holes.

Simulations and theoretical studies to understand the behaviour of low-noise avalanche materials are presented in Chapter 5. Again, recurrence equations are used to simulate gain and noise characteristics in very low noise materials under different light injection profiles. In addition, Randomly-generated ionisation Path Lengths (RPL) model is used to track the avalanche events inside the devices, providing an explanation for the shape of the noise characteristics. In addition, figures of merit for detector performances are derived, showing the interest of using APDs for the detection of small light signals.

Chapter 6 gives details about the fabrication and study of a SAM APD combining a thin AlGaAsSb multiplication region and InGaAs as absorption material. Values of dark current and photocurrent are measured. The temperature dependence of dark currents and gain is presented. A value for the temperature coefficient of breakdown voltage is extracted for this SAM APD structure.

Finally, Chapter 7 summarises the findings of the thesis and proposes suggestions

for future work.

Chapter 2

Background theory and literature review

This chapter introduces the key notions and background theory necessary to understand this work. The impact ionisation theory is presented, including details on avalanche gain and excess noise. An overview of the different simulations techniques used to predict the gain and excess noise of APDs are also shown. The second part of this chapter is a literature review on low-noise APDs for optical telecommunications, defining the scope and motivations for this work.

2.1 Impact ionisation theory

2.1.1 Avalanche gain

APDs produce internal gain, often called avalanche gain, due to impact ionisation. Impact ionisation takes place in reverse biased junction with high applied electric field. A charge carrier (electron or hole) can acquire enough energy from the electric field to trigger the creation of another electron-hole pair by collision with lattice atoms. The process is illustrated in the band diagram in Fig. 2.1. Each of the two newly created carriers can in turn impact ionise and create a new pair. This is a chain reaction that produces gain, as shown on Fig. 2.2. The point where the gain becomes infinite (the reaction diverges) is the avalanche breakdown voltage V_b. The mean length that a carrier can travel before initiating a collision is called ionisation path length. The avalanche characteristics of a given material are usually quantified

by the inverse of this quantity, the so-called ionisation coefficients, generally noted α for electrons and β for holes. Those quantities can be interpreted as the average number of created electron-hole pairs by a primary carrier per unit distance. They are dependant on the material, the temperature and the applied electric field. To satisfy the energy conservation rule, the initial energy of the primary carrier must be higher than the bandgap to initiate impact ionisation. The minimum distance travelled before reaching this energy threshold is called dead-space, d.

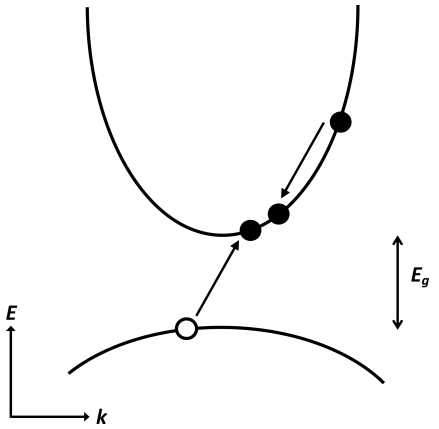

Figure 2.1: *Band diagram showing an electron-initiated impact ionisation event*

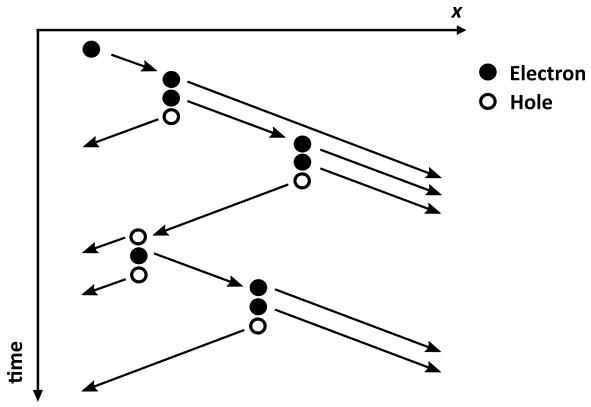

Figure 2.2: *Avalanche ionisation process, where an injected electron produces other carrier pairs by a chain reaction. In this example, a single electron is injected at one end of the avalanche region (top left corner of the schematic), and a total of 5 electrons are collected at the other end of the avalanche region, therefore producing a gain of 5.*

By the avalanche gain phenomenon, the device exhibits internal gain, which suppresses the need for external amplification processes. Gain enables the detected signal to rise above the noise floor. The gain of each event is defined as g. The

measured gain of an APD, M, is given by the average gain of all the events, so $M = \langle g \rangle$.

Fig 2.2 shows one electron injected into the p-region (left side), but it is obvious that the multiplication results will depend on the position where the carrier (or electron-hole pair) is injected. This injection position dependence is of prime importance and will be studied in details throughout this thesis.

2.1.2 Excess noise

Impact ionisation is a stochastic process: the value of individual gain for one event, g, fluctuates around a mean value, M. The variation of g from event to event introduces noise, called avalanche noise, or excess noise. The avalanche noise is characterised by the excess noise factor F, defined by

$$F = \frac{\langle g^2 \rangle}{\langle g \rangle^2} = \frac{\langle g^2 \rangle}{M^2}. \tag{2.1}$$

McIntyre [1] showed that the excess noise factor depends on the diode gain, and on the ratio of the ionisation coefficients $k = \beta/\alpha$. In the absence of dead-space, the so-called McIntyre's local model gives F as a function of M,

$$F(M) = kM + \left(2 - \frac{1}{M}\right)(1 - k). \tag{2.2}$$

This formula is valid for pure electron injection, however it still holds for pure hole injection, provided that k is replaced by $k' = \alpha/\beta$. From Eq. 2.2, it can be seen that a material with dissimilar ionisation coefficients for electrons and holes will achieve lower excess noise for a given M. The formula also shows that the type of carriers that ionises preferentially should be injected in majority into the device.

While the ionisation coefficients are intrinsic of materials, it is possible to engineer the devices to change the *effective* k. For example, having significant dead-space has been shown to reduce excess noise [2]. Devices with sub-micrometre avalanche regions exploit this effect.

2.1.3 Models and simulations

Several models can be used to describe impact ionisation. The simplest is the widely used McIntyre's local model, with Eq. 2.2 as a master expression. This model, however, fails to describe APDs with thin avalanche regions, as significant dead-space causes a reduction of the excess noise. Indeed, for sub-micrometre multiplication layer APDs, at a given M, F may decrease with decreasing avalanche region width, w. This trend cannot be explained by Eq. 2.2. To address this issue, several models that take dead-space into account have been developed.

One way to take the dead-space into account is to use the ionisation threshold energy of the carrier, E_{th}, which is the minimum energy that a carrier (electron or hole) needs to acquire to be able to impact ionise. In this case, d is simply

$$d = \frac{E_{th}}{qE}, \tag{2.3}$$

where E is the electric field. Since ionisation threshold energies are different for each type of carriers, there is a dead-space value for electrons, d_e, and a value for holes, d_h.

Using this definition of dead-space, Ong *et al.* proposed a model to simulate avalanche multiplication gain and excess noise in APDs using RPL [3]. This model calculates a Probability Density Function (PDF) of ionisation path lengths based on α, β, $E_{th,e}$, and $E_{th,h}$, for a given electric field. A random number is generated to decide the carrier's ionisation path length to make it stochastic. Results are obtained by averaging over a large number of trials.

Based on similar assumptions, and using the same type of PDF and dead-space model, Hayat *et al.* [4] developed coupled recurrence equations to determine the gain and excess noise factors for APDs. More details on recurrence equation simulations can be found in Chap. 3.

In these non-local models, the local ionisation coefficients, α and β, can be replaced by effective ionisation coefficients, α^* and β^*, that can be related to the local ones by

$$\alpha^* = \frac{1}{\frac{1}{\alpha} - d_e}. \tag{2.4}$$

An effective ionisation rate ratio $k_{eff} = \beta^*/\alpha^*$ can then be used. It is common practice

to use k_{eff} in Eq. 2.2 to compare experimentally obtained material characteristics. This will be used in Chap. 4.

The above models use a so-called hard threshold model for dead-space, where the ionisation probability is 0 below d, and decreases exponentially afterwards. A more refined "soft-threshold" model, assuming a progressive onset of impact ionisation around d, has been proposed by Tan *et al.* [5].

Both recurrence equation and RPL models are able to simulate $M(V)$ and $F(M)$ characteristics, taking only the electric field profiles, ionisation coefficients and threshold energies as input. They have the advantage of short simulation times, but are limited to devices with constant or slowly-varying electric fields.

These models have been verified experimentally, and give good results for common materials. Fig. 2.3, taken from Saleh *et al.* [6], shows a comparison between experimental excess noise values and simulated values using recurrence dead-space-multiplication theory (DSMT) from Hayat's recurrence equations on sub-micrometre GaAs (left) and InP (right) devices. The good agreement between experimental and simulated values indicates that the recurrence equations including dead-space can accurately predict excess noise characteristics for thin APDs. Similarly good results for InAlAs and AlGaAs are also presented in the paper. For the RPL model, Ong *et al.* [7] compared results from an RPL model using a hard dead-space approximation with data from a more elaborate analytical band Monte Carlo simulation (explained below) on GaAs diodes with thicknesses from 1 μm down to 50 nm. Fig. 2.4 shows excellent agreement in the gain characteristics given by both models, for both carrier injections and for all diode sizes (a). A good prediction of excess noise characteristics under electron (b) as well as hole (c) injection is also obtained for diodes down to 100 nm. For extremely thin diodes (50 nm), the RPL model predictions are slightly underestimating the excess noise values due to the hard-threshold treatment of the dead-space, whereas the more complex Monte Carlo simulation uses a more realistic ionisation PDF.

Finally, more complex models, based on Monte Carlo simulations have also been developed. Three distinct categories of Monte Carlo-based models exist. The Full-Band Monte Carlo model [8] is based on the full calculation of the material band structure. It requires the knowledge of all carrier transport parameters and scattering

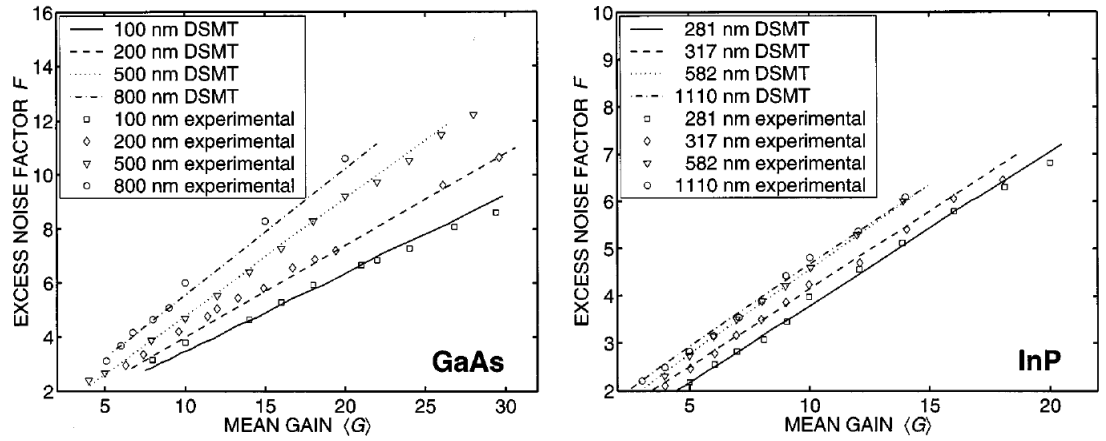

Figure 2.3: *Comparison of experimental data (symbols) and recurrence dead-space-multiplication theory (DSMT) simulation results (lines) for GaAs (left) and InP (right) devices. Figures from [6].*

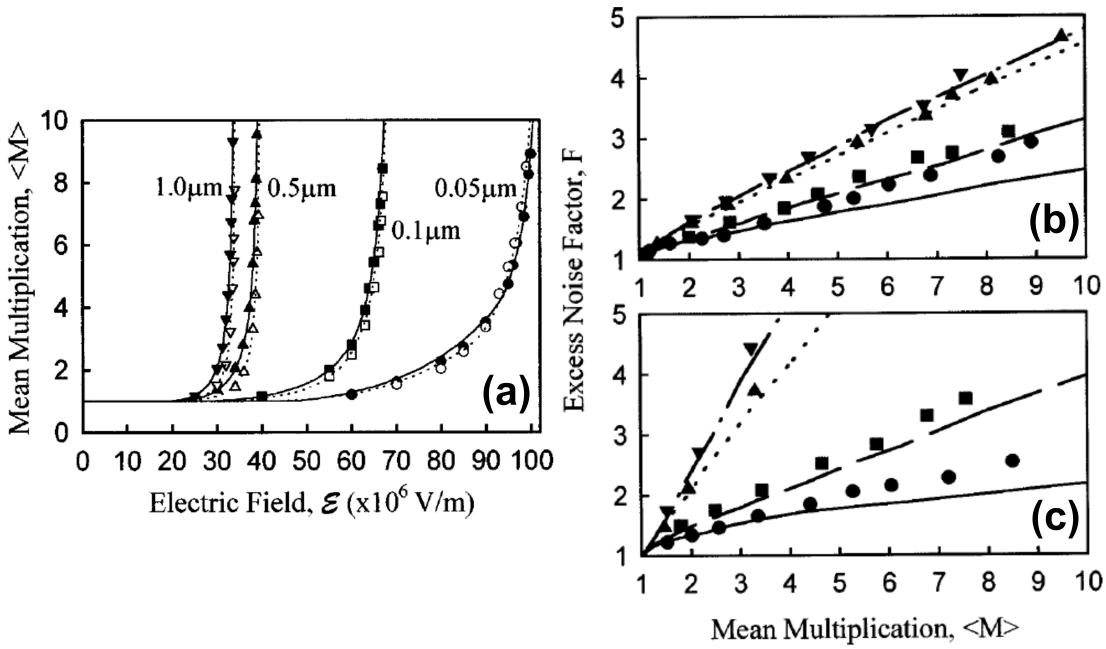

Figure 2.4: *(a) Multiplication as a function of electric field results from RPL simulations (solid lines for electron injection, dashed lines for hole injection) and Analytical Band Monte Carlo simulations (filled symbols for electron, open symbols for hole injection) for GaAs diodes of different thicknesses. Excess noise versus mean gain for (b) electron and (c) hole-initiated multiplication for 0.05 (solid line, ●), 0.1 (dashed line, ■), 0.5 (dotted line, ▲), and 1.0 μm (dot-dashed line, ▼) GaAs diodes. Lines are results from RPL simulations, symbols are results from Monte Carlo simulations. Figures from [7].*

mechanisms for all the bands, and is therefore limited to well-known materials such as Si, GaAs or InP. A simplification of this model is known as Analytical Band Monte Carlo [9]. It uses analytical approximations for the material band structure. Both

models can give very accurate results, at the expense of long computation times. They also require many material physical parameters, that are often unknown when dealing with novel materials. Finally, a simplified model, using only a single parabolic band to approximate the band structure is known as Simple Monte Carlo [10, 11]. Less computationally intensive, this model still requires the knowledge of certain parameters such as the carrier velocities and phonon energies, that are not necessary available for novel materials, such as quaternary materials. Due to the simple approximation on the band structures, this model also fails to model properly the carrier drift velocities at low electric fields.

In this thesis, recurrence equations will be used for the simulations in Chaps. 4 and 5. The RPL model will also be used in Chap. 5 for its ability to track the number of carriers for each impact ionisation event.

2.2 APD structures and development

Below is a review of research on APDs for optical communications. The different ways to obtain efficient, low noise, and fast optical detectors are discussed. State-of-the-art technologies are also presented.

2.2.1 Overview

The vast majority of commercial APDs are currently made of silicon, but compound semiconductor materials have also been explored since the late 60s. The development of III-V APDs was triggered by the telecommunication field. The need for faster, low noise detectors led to a considerable development of materials like InGaAs and InP, which operate in the range of interest for telecommunications (near infra-red). InGaAs APDs are also commercially available with providers such as Hamamatsu [12] or Thorlabs [13], but the narrow bandgap of InGaAs ($E_g = 0.75$ eV) limits the maximum applied electric field, and therefore the maximum gain.

A good APD should show efficient absorption at the wavelength of interest (1310 and 1550 nm in the case of optical communications), low noise and low dark current. The constantly increasing bit rate for the exchange of information also means that

fast photodetectors are desired.

A major milestone in the development of APDs is the design of SAM APDs. They allow better efficiency by using a narrow bandgap material as absorption layer (more effective photon absorption, and necessary to detect longer wavelengths) and a large bandgap material for the avalanche layer (lower dark current). Susa *et al.* [14] illustrated this in 1981 with their InGaAs/InP SAM APD. The use of InP ($E_g = 1.35$ eV) as multiplication layer, where the high field is present, separated from the narrow bandgap InGaAs absorption layer ($E_g = 0.75$ eV) made it possible to suppress the tunnelling current in the narrow energy gap layer, allowing them to obtain diodes with a gain around 60.

Several approaches to reduce excess noise and improve speed have been explored. One can act on the material itself or on the device structure, via impact ionisation engineering or exploitation of the dead-space effect.

2.2.2 Materials with large ionisation coefficient ratio

As can be seen from McIntyre's theory of impact ionisation, materials with dissimilar ionisation coefficients will yield lower excess noise. In addition, Emmons showed that a low k also improves the bandwidth of an APD [15]. The focus has therefore been set on investigating materials with such properties. One of the best candidates has been silicon. Many authors have reported largely dissimilar ionisation coefficients in Si APDs [16, 17]. Excess noise properties of Si are indeed excellent, with reported values of k_{eff} below 0.05 [18, 19]. However, Si being almost transparent to the optical communications wavelengths, 1310 and 1550nm, it is ill-suited for telecommunication purposes.

InGaAs, on the other hand, has excellent absorption properties in the near infrared, and is therefore widely used in optical communications. The problem is that its narrow bandgap limits the maximum electric field that can be sustained, hindering the multiplication capabilities. Nevertheless, impact ionisation coefficients can be found in literature [20]. The electron and hole ionisation coefficients are largely dissimilar over a wide range of electric fields, giving low excess noise.

InAs has also attracted much interest due to its narrow bandgap ($E_g = 0.354$ eV), allowing detection of light in the near-infrared. Impact ionisation in InAs is dominated

by electrons, with almost no hole ionising, yielding virtually $k = 0$. This means the excess noise factor F is mostly independent of the gain [21]. While these noise characteristics are a great advantage, InAs suffers from large bulk dark currents at room temperature. This, along with the high financial cost of InAs substrates, has prevented commercialisation of InAs APDs.

2.2.3 Bandgap engineering

As mentioned in section 2.1.1, the excess noise produced by the avalanche multiplication phenomenon can be reduced through impact-ionisation engineering. One example is the first superlattice APD designed by Capasso *et al.* in 1981 [22]. They used a stacking of 50 alternating GaAs (450 Å) and $Al_{0.45}Ga_{0.55}As$ (550 Å) layers, leading to an increased effective ionisation rate ratio of 8. This relies on the discontinuities in the conduction band edges between the two different materials. For each step, when an electron travelling through the wide-bandgap AlGaAs reaches the narrower-bandgap GaAs quantum well, it abruptly sees a change in energy due to the band-edge discontinuity and thus sees its ionisation energy increased by the band offset. This leads to an increased effective ionisation coefficient for the electrons. On the other end, the valence band discontinuities are much smaller, leaving the effective hole ionisation coefficient relatively unaffected, therefore increasing the effective ionisation rate ratio, k_{eff}. Unfortunately, the concept was limited by the choice of materials available at that time, and the AlGaAs/GaAs system did not offer sufficiently large conduction band edge offsets to provide good gain characteristics.

However, the concept was successfully reused in 2016 by Ren *et al.* [23] using alternating $Al_{0.7}In_{0.3}As_{0.31}Sb_{0.69}$ (wide bandgap of $\sim$ 1.16 eV) and $InAs_{0.91}Sb_{0.09}$ (narrow bandgap of $\sim$ 0.25 eV) layers. The principle is shown in the schematic in Fig. 2.5. In this case, they claim a gain of $\sim$ 2 for each step. The gain is repeatable from event to event, leading to a potentially very low excess noise.

2.2.4 Low excess noise in thin avalanche regions

Carrier transit time plays an important role in the speed of APDs, thus thin avalanche regions are more beneficial for high speed APDs. The problem is that, for thin avalanche regions and consequently high electric fields, the ionisation coefficients

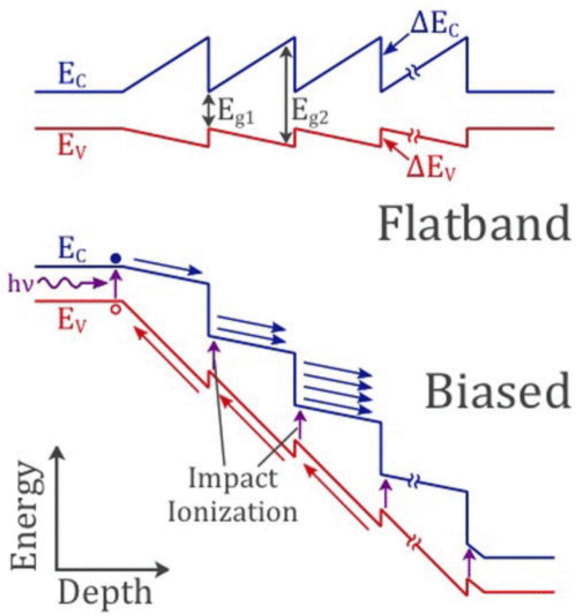

Figure 2.5: *Schematic band structure of the staircase APD by Ren et al. The electrons in the conduction band impact ionise (blue arrows) whereas the holes in the valence band do not (red arrows). Picture from [23].*

values for most semiconductor materials tend to converge towards each other, giving a k value closer to 1, and therefore one may expect the excess noise to increase. Fortunately, the dead-space effect comes into the picture, reducing excess noise values for thin avalanche regions [4, 24]. Efficient APDs can then be designed using ultra-thin avalanche regions. Below is a review of thin APDs showing very low noise characteristics.

One of the earlier reports of the exploitation of dead-space effect in silicon was by Tan *et al.* in 2000 [25]. They measured excess noise characteristics of thin Si p^+-i-n^+ diodes (avalanche widths w of 100, 150, and 290 nm) under pure electron, pure hole, and mixed injection conditions. They obtained excess noise values corresponding to $k_{eff} \simeq 0.2$ for these diodes under pure electron injection, with excess noise values nearly independent from w, showing the effect of dead-space on excess noise reduction, but also that for such thin avalanche layers in Si, the increase in β/α ratio value for increasing electric fields offsets the benefits on excess noise.

Widely used in telecommunications, InP can be combined with lattice-matched $In_{0.53}Ga_{0.47}As$ as absorber in SAM APD structures. The interest is that InGaAs, with its bandgap of 0.75 eV, absorbs in the wavelength of interest for telecommunications,

1550 nm. One particularity of InP as an avalanche material, is that its hole ionisation coefficient, β, is bigger than the electron one, α, meaning that pure hole injection should be achieved for best gain and noise performances. In 2000, Yuan *et al.* [26] showed the significant dead-space induced deviation in the $F(M)$ characteristics from the ones predicted by local model theory in InP diodes of widths $w < 1.2$ μm. The lowest k_{eff} values they obtained were around $0.2 - 0.25$, for 281 nm diodes under pure hole injection.

Another material of interest, $In_{0.52}Al_{0.48}As$, lattice-matched to InP, can be also be combined with $In_{0.53}Ga_{0.47}As$ absorption regions. In 2007, Goh *et al.* [27] measured excess noise characteristics corresponding to k_{eff} values of $0.15 - 0.25$ for a series of p^+-i-n^+ diodes with w ranging between 100 nm and 2.5 μm.

Grown on GaAs substrate, $Al_xGa_{1-x}As$ has attracted interest for its wide bandgap, that can be tuned varying x while staying lattice-matched to GaAs. For Al contents $x > 0.45$, the bandgap becomes indirect, reducing the direct band-to-band tunnelling and thus allowing for thinner devices. Exploiting this effect, in 2001, Tan *et al.* [28] used $Al_{0.6}Ga_{0.4}As$ (wide indirect bandgap around 2 eV) and were able to obtain APDs with multiplication region thickness, w, as thin as 26 nm, exacerbating the dead-space effect. k_{eff} slightly below 0.1 were obtained.

More recently, amongst extensive research to find very low noise materials, $AlAs_{0.56}Sb_{0.44}$ has been investigated. This material is of interest since it is latticed-matched to InP substrates, and its wide bangdgap ($E_g = 1.64$ eV) theoretically allows it to sustain higher electric fields than InP. In 2012, Xie *et al.* [29] obtained record-low k_{eff} values of 0.05 for 230 nm p^+-i-n^+ diodes.

But the lowest excess noise values so far have been reported by Ren *et al.* [30] in 2017, using $Al_xIn_{1-x}As_ySb_{1-y}$, grown by Molecular Beam Epitaxy (MBE) on GaSb substrates. Using the digital alloy technique, they managed to overcome the Al miscibility gap, allowing then to reach higher Al concentrations than were achieved before (up to Al fractions of 0.8). They reported k_{eff} values as low as 0.01 in $Al_{0.7}In_{0.3}As_{0.3}Sb_{0.7}$ p-i-n APDs with 890 nm multiplication region.

Fig. 2.6 summarises the k_{eff} values found in literature for the key materials used for designing low-noise APDs.

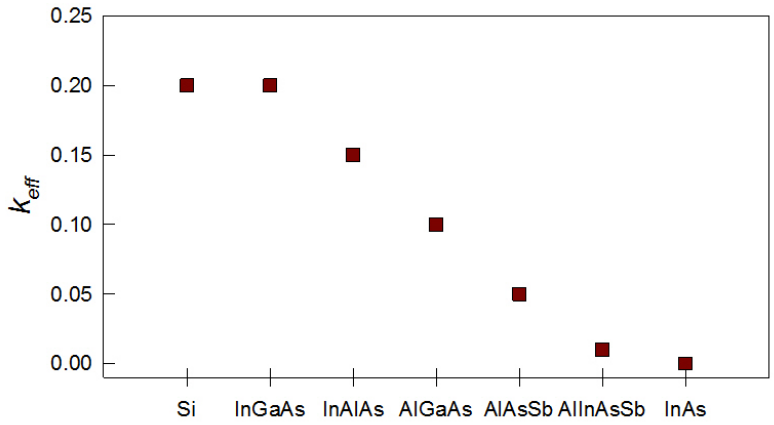

Figure 2.6: *Comparison of k_{eff} values found in the literature for thin APDs made of Si [25], InGaAs [26], InAlAs [27], AlGaAs [28], AlAsSb [29], AlInAsSb [30], and InAs [21]*

2.2.5 SAM APDs for optical communications

The common approach is therefore to combine the best possible avalanche material with the best possible absorber. As mentioned in part 2.2.1, in a SAM APD, the narrow-bandgap absorption region is separated from the wide-bandgap multiplication region. A highly doped 'charge sheet' separates the two regions, controlling the electric field in the device. A schematic of the electric field within a SAM APD is shown in Fig. 2.7. The electric field in the absorption is kept low to mitigate tunnelling currents, whereas high electric fields are required in the multiplication layer to initiate the impact ionisation process.

The most common APDs in optical telecommunications are InGaAs/InP offering good absorption at 1310 and 1550 nm, and high speeds, with Gain-Bandwidth Products (GBPs) ranging between 70 and 122 GHz [14, 31, 32, 33]. Those generally include a InGaAsP grading layer as a transition between InGaAs and InP.

Another popular combination is InGaAs/InAlAs. Both materials also benefit from mature growth and fabrication technologies. The good properties of InAlAs as avalanche material made possible the design of SAM APDs with improved GBPs compared to InGaAs/InAlAs APDs [34, 35]. GBPs up to 290 GHz have been demonstrated using resonant-cavity devices [36], designed to enhance light detection efficiency at 1550 nm.

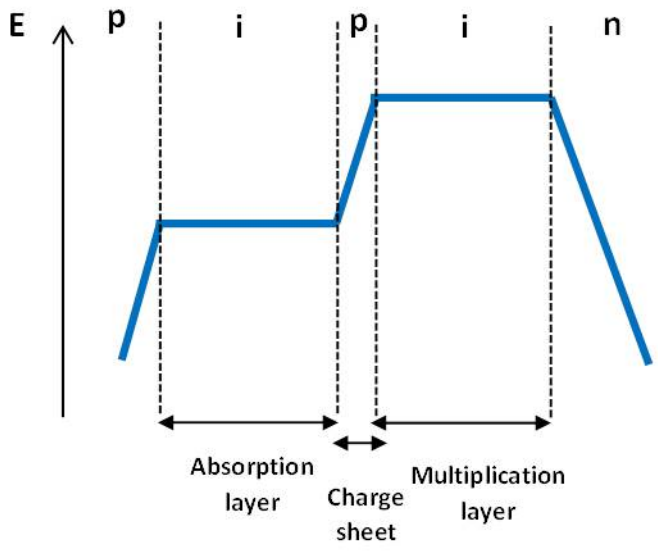

Figure 2.7: *Electric field profile within a SAM APD, showing the low-field absorption layer, the charge sheet controlling the electric field, and the high-field multiplication layer*

Germanium on silicon APDs have also been investigated, taking advantage of the low cost, high maturity and low noise characteristics of Si [37, 38]. Large GBP values of 340 GHz have been reported [39]. Germanium is used as the absorption layer, since its narrow bandgap (0.67 eV) allows it to absorb near infrared wavelengths. In these structures, the key part is the quality of the heterointerface between Si and Ge, as a large lattice mismatch prevents good epitaxy. However, if Ge-on-Si APDs perform well at 1310 nm, their capabilities are reduced at 1550 nm, due to a less efficient absorption in Ge. The absorption coefficient of Ge at 1550 nm is lower than that at 1310 nm by an order of magnitude at room temperature and by three orders of magnitude at 77 K [40].

Recently, SAM APDs utilising novel avalanche materials have been investigated. Using the ultra-low noise properties of AlAsSb, Tan *et al.* demonstrated InGaAs/AlAsSb APDs with $k_{eff} = 0.15$, yielding lower noise than InGaAs/InAlAs diodes ($k_{eff} = 0.2$), while showing high responsivity at 1.5 μm, and exhibiting gain up to $\sim$ 10 [41]. In 2015, Xie *et al.* reported InGaAs/AlAsSb with very small temperature coeficient of breakdown of 8 mV/K [42]. Finally, the highest GBP value reported was obtained by Xie *et al.* in 2016, using an InGaAs/$Al_{0.85}Ga_{0.15}As_{0.56}Sb_{0.44}$ SAM APD [43]. A GBP value of 424 GHz has been obtained. The GBP values for

the SAM APDs discussed in this part are summarised in Fig. 2.8.

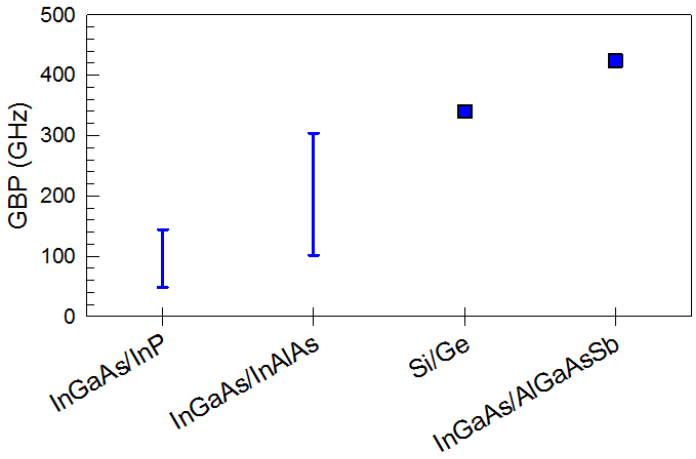

Figure 2.8: *Gain-Bandwidth Products for typical SAM APDs used in optical telecommunications, and for novel material SAM APDs [14, 31, 32, 33, 34, 35, 37, 38, 43]*

2.2.6 Advantages of AlGaAsSb and areas requiring study

The good results obtained with $AlAs_{0.56}Sb_{0.44}$ and $Al_{0.85}Ga_{0.15}As_{0.56}Sb_{0.44}$ as avalanche materials justify further studies. These two materials have a large, indirect bandgap ($E_g = 1.64$ and 1.56 eV respectively [44]), allowing them to sustain very large electric fields with insignificant band-to-band tunnelling currents. AlAsSb however, suffers from large surface leakage currents due the important oxidation of Al and Sb. It has been shown that adding Ga to reduce the Al content significantly reduces dark currents [44, 45]. AlGaAsSb is therefore a good candidate for realising efficient APDs with low dark currents, excellent thermal and temporal stability [46], and very high bandwidth [43]. However, more work is required on this material, for example excess noise characteristics are missing. If it is known that pure electron injection is favourable for materials with $\alpha > \beta$, the effect of carrier injection profile, and especially the case of mixed carrier injection on very low k_{eff} materials also needs to be investigated. More work also remains to be done on SAM APDs including an AlGaAsSb avalanche layer for optical communication applications, so that these devices can realise their full potential and become viable alternatives to current technologies.

Chapter 3

Experimental Techniques

This chapter will describe the setups and tools used throughout this thesis to characterise APDs, including current-voltage (I-V), capacitance-voltage (C-V), low temperature, gain, and excess noise measurements. The recurrence simulation method will also be described.

3.1 Current-voltage measurements

Electrical characterisation of our devices starts with current-voltage (I-V) measurements. To measure currents down to pA range, a HP 4140B picoammeter, a Keithley 236 Source–Measurement Unit (SMU) or an Agilent B1505A Device Analyser were used.

Under forward bias, the current in a diode can be modelled by:

$$I(V) = I_s \exp\left[\frac{q(V - IR_s)}{nk_BT} - 1\right], \tag{3.1}$$

where I_s is the saturation current, depending on the materials properties and R_s is the series resistance induced by the metal contacts and the metal/semiconductor interfaces. k_B is the Boltzmann constant, and T is the temperature. n is the ideality factor of the diode ($1 \leq n \leq 2$), its value gives an indication of the dominant current mechanism: 1 for diffusion current, 2 for generation-recombination current. An ideality factor close to 2 indicates that the current is dominated by generation-recombination mechanisms, revealing the presence of an important concentration of impurities and electron traps in the material bulk.

When a diode is reverse-biased, the I-V characteristic gives the value of the avalanche breakdown voltage V_b. A variation of V_b across devices from a given sample can indicate premature edge breakdown, which is undesirable.

The change in the I-V characteristic between dark and when the diode is illuminated also shows the photoresponse of the device.

The dark current density has a bulk (J_b) and a surface (J_s) components such as

$$I_d = J_b A + J_s P,$$

with A and P being respectively the area and perimeter of the device. By measuring different-sized diodes, it is possible to determine whether the dark current scales with area or perimeter and therefore deduce if the mechanism is bulk or surface dominated.

Surface leakage currents are due to surface states. The devices studied in Chaps. 4 and 6 have mesa structures, obtained by chemical etching. The etching process creates damages in the surface of mesa walls, and exposure to air can lead to the oxidation or contamination of the mesa edges, introducing surface states.

The bulk leakage current is the sum of the diffusion current of the carriers I_{diff}, the generation-recombination current due to defects in the material $I_{g\text{-}r}$ and the tunnelling current I_{tunn}. The generation-recombination current, which is dominant at low voltage can be modelled by [47]

$$I_{g\text{-}r} \cong \frac{q n_i A W}{\tau_{eff}} \left[1 - \exp\left(-\frac{qV}{2k_B T} \right) \right], \tag{3.2}$$

where n_i is the intrinsic carrier concentration, τ_{eff} is the effective carrier lifetime and W is the depletion width of the junction.

For the tunnelling current, dominant at higher bias [48],

$$I_{tunn} \cong \frac{(2m^*)^{\frac{1}{2}} q^3 E V A}{h^2 E_g^{\frac{1}{2}}} \exp\left[-\frac{2\pi\sigma_T (2m^*)^{\frac{1}{2}} E_g^{\frac{3}{2}}}{qhE} \right]. \tag{3.3}$$

Here m^* is the electron effective mass, E the maximum electric field in the junction and σ_T is a constant that depends on the shape of the tunnelling barrier. It is worth noting the dependence with material bandgap E_g, making tunnelling currents

particularly significant in narrow bandgap semiconductors.

Since the different dark current mechanisms vary differently with temperature, the temperature dependence of dark I-V characteristics can give clues to the main physical phenomenon at stake.

Dark currents degrade the performances of photodetectors, it is therefore of prime importance to assess the dark current levels and detect their mechanism of origin.

3.2 Capacitance-voltage measurements

Capacitance-voltage (C-V) measurements are performed in complement to I-V data. It is possible to deduce further information about the device structure, the material properties and electric field profiles. A HP 4275A Multi-Frequency LCR meter or an AGILENT B1505A Device Analyser equipped with a Capacitance Measurement Unit (CMU) are used. They can deduce the capacitance of the diode from impedance measurements. Electric field in the device can also be estimated from the C-V data.

The capacitance of the diode is related to the depletion width (W) in the diode by

$$C(V) = \frac{\varepsilon A}{W(V)}, \tag{3.4}$$

where ε is the dielectric permittivity of the semiconductor and A is the diode area. Eq. 3.4 also shows that the capacitance scales with the device area. For mesa diodes, this can be experimentally checked to confirm the good quality of the mesas. A poor scaling indicates an undercut in the mesa profiles (the mesa section is not constant).

Using Poisson's equation

$$\frac{dE}{dx} = -\frac{qN}{\varepsilon}, \tag{3.5}$$

with q the electronic charge and N the density of charge (fixed and mobile) in the material region, it is possible to estimate the doping level and electric field profile in the different materials of the diode, by fitting the C-V data.

3.3 Gain and excess noise measurements

3.3.1 Description of the setup

Excess noise measurements were carried out using a setup described by K.F. Li [49]. A schematic of the setup is presented in Fig. 3.1. The Device Under Test (DUT), reverse-biased with a KEITHLEY 2400 SMU, is illuminated by a light source chopped at a frequency $f \sim 180$ Hz. The resulting photocurrent (I_{ph}) is converted to voltage, V_{ph}, by a Transimpedance Amplifier (TIA), with a gain of 2200 V/A. This photocurrent value is subsequently measured by a Lock-in Amplifier (LIA), synchronised to the light chopping frequency. For the excess noise measurement, the voltage signal representing the modulated photocurrent, V_{ph}, is filtered using a bandpass filter of frequency range 8-12 MHz, and amplified, before being measured by a power-meter. A second LIA is used to give the noise signal value at the frequency f. An attenuator is inserted before the power-meter to prevent saturating the power-meter. The output of the measurement is therefore a set of photocurrent and noise signal values versus bias voltage.

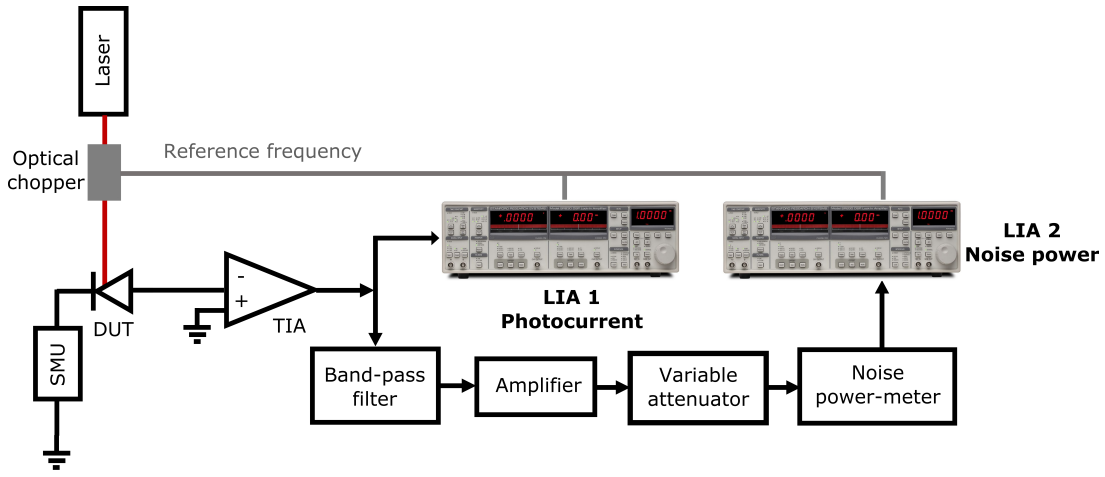

Figure 3.1: *Excess noise setup schematic*

3.3.2 Gain values

To obtain the avalanche gain M, the photocurrent values are divided by the primary photocurrent values, I_{pr}, such as

$$M = \frac{I_{ph}}{I_{pr}}. \tag{3.6}$$

I_{pr} is estimated from the values of photocurrent at low voltage biases (where no multiplication takes place). Due to the increase of collection efficiency because of depletion edge movement, the values of I_{pr} increase slightly with voltage even before the onset of multiplication. I_{pr} therefore needs to be corrected in order to obtain the true value of the gain. At low voltages, the increase in I_{pr} can be described by [17]

$$\frac{I_{pr}(V)}{I_{pr}(0)} = \frac{1}{\cosh(L(V)/L_d)}, \tag{3.7}$$

where $L(V)$ is the characteristic distance between where the absorption took place and the depletion edge, and L_d is the diffusion length of the carriers contributing to the photocurrent. In the diodes studied in Chap. 4, the highly-doped cladding layers are thin (a few hundred nm), it is therefore possible to assume that $L_d \gg L(V)$ for all voltages, thus Eq. 3.7 can be approximated as

$$I_{pr}(V) = aV + b,$$

where a and b are fitting parameters.

3.3.3 Noise power

For an APD, the impact ionisation process introduces extra noise, quantified by the excess noise factor F. The shot noise power is

$$N_{APD} = 2qI_{ph}MFB_{\mathit{eff}} = 2qI_{pr}M^2FB_{\mathit{eff}}, \tag{3.8}$$

where B_{eff} is the equivalent noise bandwidth. For an ideal non-avalanching photodiode (with no extra noise, *i.e.* $F = 1$), the ideal noise power would be

$$N_{ideal} = 2qI_{pr}B_{eff}. \tag{3.9}$$

Consequently, the noise of an APD is

$$N_{APD} = N_{ideal}M^2F. \tag{3.10}$$

To obtain the excess noise factor of the DUT, the system first needs to be calibrated using a commercial silicon non-avalanching photodiode (BPX 65 from CENTRONIC [50]), which is assumed to be an ideal diode at low reverse biases. The setup described in part 3.3.1 is designed to output a noise power value N_{meas} proportional to the photocurrent. In this case,

$$N_{meas} = N_{ideal} = k_N I_{pr} \tag{3.11}$$

since $M = 1$ (no gain). The calibration factor, k_N is obtained by linearly fitting the N_{ideal} versus I_{ph} curves (Fig. 3.2), obtained by varying the incoming light intensity with an optical attenuator, for a fixed reverse bias. Note that k_N is dependent on the light source and the circuit.

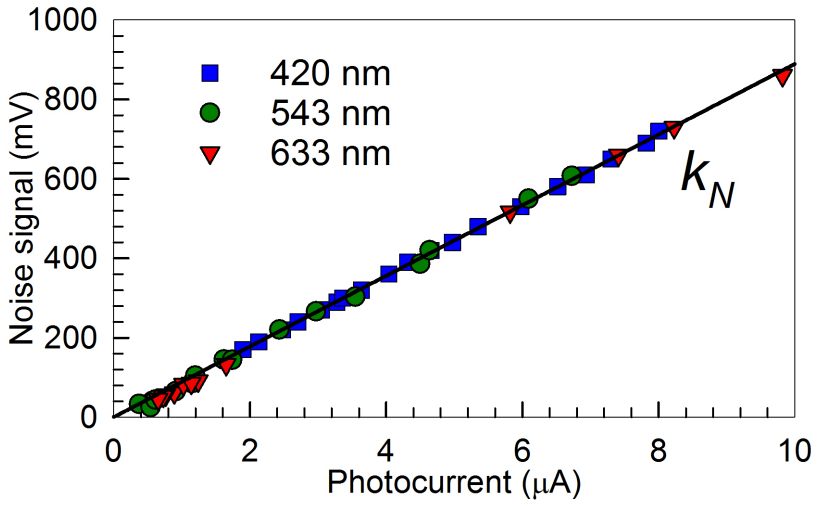

Figure 3.2: *Determination of k_N coefficient for excess noise measurements*

Consequently, substituting Eq. 3.11 into Eq. 3.10 gives

$$F = \frac{N_{APD}}{k_N I_{pr} M^2}. \tag{3.12}$$

However, the equivalent noise bandwidth depends on the device capacitance, and it is therefore necessary to apply a correction factor to the measured noise,

$$N_{APD} = N_{meas} \times \frac{B_{\mathit{eff}}(C_{Si})}{B_{\mathit{eff}}(C_{APD})}, \tag{3.13}$$

where C_{Si} is the capacitance of the Si calibration diode at the fixed calibration voltage, and C_{APD} is the capacitance of the DUT at the measurement voltage. Note that this correction procedure becomes less reliable for DUT capacitance greater than ~ 30 pF [51]. The excess noise factor is finally given by

$$F = \frac{N_{meas}}{k_N I_{pr} M^2} \times \frac{B_{\mathit{eff}}(C_{Si})}{B_{\mathit{eff}}(C_{APD})}. \tag{3.14}$$

3.4 Low-temperature measurements

For measurements at lower temperatures, a JANIS ST-500 probe station is used. Fig. 3.3 shows a picture of the probe station. The samples are placed on a cold plate cooled down by liquid nitrogen. A temperature controller allows measurements between liquid nitrogen temperature (77K) and room temperature. The probe station has two DC probe arms and a multimode optical fibre, enabling I-V and photocurrent measurements.

3.5 Recurrence equations model

The simulations carried out in the following chapters use the recurrence equations from Hayat *et al.* [4], as stated in Chap. 2.

In this model, one injected electron travels at a constant velocity v_e over a random distance X_e before initiating an impact ionisation event. It is therefore replaced by two electrons and one hole. Each electron is treated independently in the same statistical manner. The hole travels in the opposite direction at a velocity v_h over a

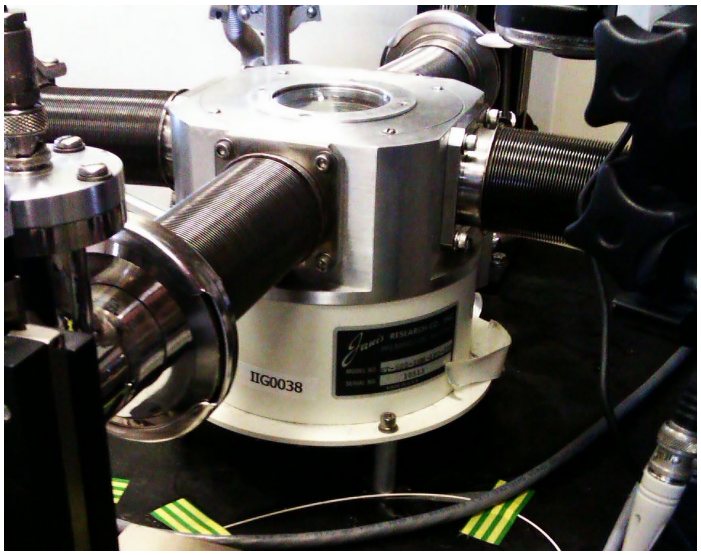

Figure 3.3: JANIS *ST-500 probe station*

distance X_h before initiating an impact ionisation event, giving two holes and one electron.

The PDF of X_e and X_h are $h_e(x_e)$ and $h_h(x_h)$, expressed as

$$h_e(x_e) = \begin{cases} 0 & \text{for } x_e < d_e \\ \alpha^* e^{-\alpha^*(x_e - d_e)} & \text{for } x_e \geq d_e \end{cases}, \tag{3.15}$$

and

$$h_h(x_h) = \begin{cases} 0 & \text{for } x_h < d_h \\ \beta^* e^{-\beta^*(x_h - d_h)} & \text{for } x_h \geq d_h \end{cases}, \tag{3.16}$$

where α^* and β^* are the ionisation coefficients for the electrons and holes that have travelled beyond the dead-space (also called effective, or enabled ionisation coefficients), d_e and d_h are the electron and hole dead-space values. The multiplication event finishes when all electrons reach the n-side ($x = w$) and all holes reach the p-side ($x = 0$). The model is illustrated in the schematic in Fig. 3.4 (a). Fig. 3.4 (b) plots the PDF for electrons.

Consider an electron-hole pair injected at a position x within the multiplication region. Due to impact ionisation, the electron will create a random number of electron-hole pairs, $Z(x)$, while the hole will generate $Y(x)$ pairs. We note $z(x) = \langle Z(x) \rangle$ and $y(x) = \langle Y(x) \rangle$ the ensemble average of $Z(x)$ and $Y(x)$. The mean multiplication

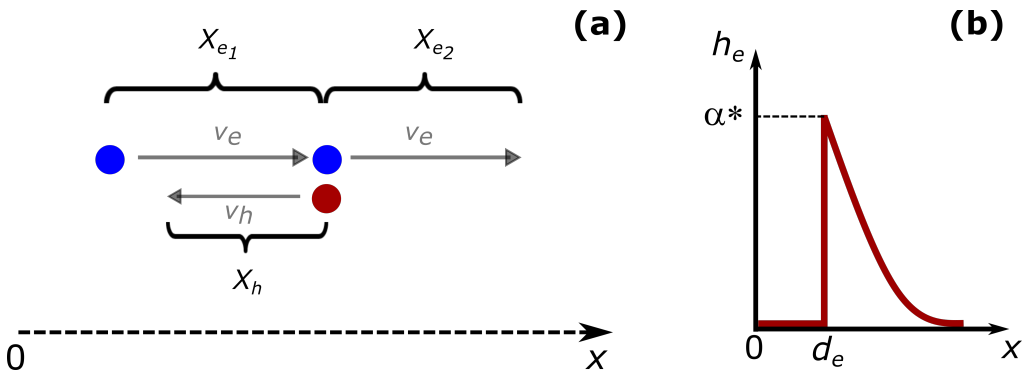

Figure 3.4: *(a) Schematic illustrating the recurrence model. (b) PDF for electrons in the recurrence model.*

$\langle M(x) \rangle$ due to the electron-hole pair injected at x is therefore

$$\langle M(x) \rangle = \frac{1}{2} \left(z(x) + y(x) \right). \tag{3.17}$$

The excess noise factor is defined as

$$F(x) = \frac{\langle M^2(x) \rangle}{\langle M(x) \rangle^2} = \frac{z_2(x) + 2z(x)y(x) + y_2(x)}{\left(z(x) + y(x) \right)^2}, \tag{3.18}$$

where $z_2(x) = \langle Z(x)^2 \rangle$ and $y_2(x) = \langle Y(x)^2 \rangle$ are the second moments of $Z(x)$ and $Y(x)$. F and M can therefore be derived from $z(x)$, $y(x)$, $z_2(x)$, and $y_2(x)$. Using statistical considerations, Hayat *et al.* showed that $z(x)$ and $y(x)$ can be derived as (Eq. (10) and (11) in [4])

$$z(x) = \left[1 - H_e(w - x) \right] + \int_x^w \left[2z(\xi) + y(\xi) \right] h_e(\xi - x) d\xi, \tag{3.19}$$

where

$$H_e(x) = \int_{-\infty}^{x} h_e(\xi) d\xi.$$

Similarly,

$$y(x) = \left[1 - H_h(x) \right] + \int_0^x \left[2y(\xi) + z(\xi) \right] h_h(x - \xi) d\xi, \tag{3.20}$$

with

$$H_h(x) = \int_{-\infty}^{x} h_h(\xi) d\xi.$$

$z_2(x)$ and $y_2(x)$ are given by Eqs. (18) and (19) in [4]:

$$z_2(x) = [1 - H_e(w - x)] + \int_x^w \left[2z_2(\xi) + y_2(\xi) + 4z(\xi)y(\xi) + 2z^2(\xi)\right] h_e(\xi - x)d\xi, \tag{3.21}$$

and

$$y_2(x) = [1 - H_h(x)] + \int_0^x \left[2y_2(\xi) + z_2(\xi) + 4z(\xi)y(\xi) + 2y^2(\xi)\right] h_h(x - \xi)d\xi. \tag{3.22}$$

The coupled recurrence equations (Eqs. 3.19, 3.20, 3.21, and 3.22) are then solved numerically by iterative methods, and used to solve Eqs. 3.17 and 3.18. The result is a set of M and F values for a carrier pair injected at a position x, for a given reverse bias. The full derivation can be found in [4].

Chapter 4

Thin AlGaAsSb APDs with very low excess noise

As mentioned in the previous chapter, AlGaAsSb offers possibilities of large GBPs [43] and benefits from excellent thermal and temporal stability of avalanche gain [46]. However, as for now, only very limited excess noise results are available. Zhou *et al.* [52] reported partial excess noise results on *p*-*i*-*n* diodes with $\sim$ 110 nm avalanche regions, but limited by experimental conditions, pure electron injection has not been achieved. Nevertheless, these results showed that thin AlGaAsSb APDs display very low excess noise, with k_{eff} values potentially lower than 0.1.

In this chapter, the excess noise studies on AlGaAsSb are extended to *p*-*i*-*n* and *n*-*i*-*p* diodes with 100 and 200 nm nominal thicknesses. Gain and excess noise data are obtained under pure electron injection in the *p*-*i*-*n* diodes and pure hole injection in the *n*-*i*-*p* diodes. Mixed injection conditions were also covered for both types of diodes. This chapter presents details about the fabrication and characterisation of the AlGaAsSb devices, including *I*-*V*, *C*-*V*, gain and excess noise measurements. Recurrence simulations were also carried out to estimate the electron and hole ionisation coefficients, as well as the dead-space values.

4.1 Device structures and fabrication

The wafers used in this chapter are four $Al_{0.85}Ga_{0.15}As_{0.56}Sb_{0.44}$ diode structures, two *p*-*i*-*n* (PIN 1 and PIN 2) and two *n*-*i*-*p* diodes (NIP 1 and NIP 2), with nominal

i-region thicknesses of 100 nm (for PIN 1 and NIP 1) and 200 nm (for PIN 2 and NIP 2). The wafers were grown by MBE on semi-insulating (SI) InP substrate by the National Epitaxy Facility in Sheffield. The wafer numbers are SF0921, SF0922, SF0926, and SF0929 for PIN 1, NIP 1, PIN 2, and NIP 2, respectively. Details of the layer structure for the 200 nm p-i-n diode are given in Fig. 4.1 (a). In each p-i-n diode wafer, the undoped i-region is sandwiched between a top 300 nm p-AlGaAsSb and a bottom 200 nm n-AlGaAsSb layers. Be atoms are used for p-doping, and Te atoms are used for n-doping. Heavily doped lattice-matched $In_{0.53}Ga_{0.47}As$ top and bottom layers are included to achieve good ohmic contact. The n-i-p diode wafers have identical structures, except that the p- and n-layers are replaced with n- and p-layers, respectively.

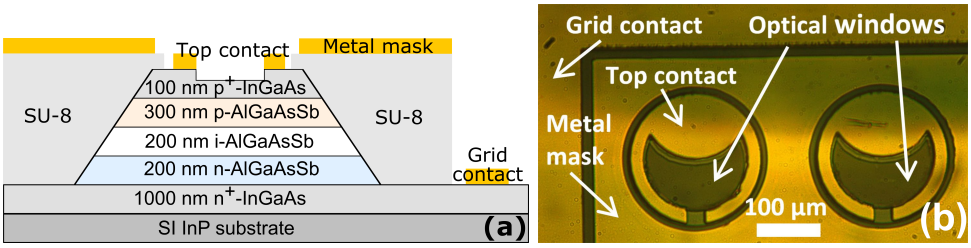

Figure 4.1: *(a) Cross-sectional schematic diagram and (b) top-view photograph of devices fabricated from the p-i-n wafers*

The wafers were fabricated into circular mesa diodes of radii 60, 110 and 210 μm using UV photolithography and wet chemical etching. The etchants used were solutions of citric acid ($C_6H_8O_7$):hydrogen peroxide (H_2O_2) in a ratio of 2:1 for InGaAs and hydrochloric acid (HCl):H_2O_2:de-ionised water in a ratio of 5:1:50 for AlGaAsSb. Ti-Au metal contacts were deposited onto the p^+ and n^+ InGaAs layers to provide ohmic contacts to the diodes. The devices were passivated using a $\sim 1 - 1.2$ μm-thick SU-8 5 resist layer (from MICROCHEM). SU-8 is an epoxy-based resist showing high mechanical and thermal stability when cured, and that can be easily spun onto the device. While it does not chemically passivate the mesa walls (*i.e.* no reduction of leakage currents is observed), it provides long-lasting protection to devices against degradation over time by preventing further oxidation of the mesa walls. To prevent side injection of light that could generate an unintended mixed carrier injection profile, a layer of metal was deposited onto the SU-8 covering the mesa sidewalls as illustrated in Fig. 4.1 (a). This is essential when the light spot

is large, such as when using an LED as the light source. Finally, to increase the collection efficiency of photo-generated carriers (and hence the photocurrent) for a given optical power of incoming light, the thickness of the top InGaAs cladding within the optical windows was reduced by etching. Examples of the fabricated devices are shown in Fig. 4.1 (b).

While the vast majority of commercial devices have a planar structure, these geometries require ion implantation and the design of specific sets of masks. Several implantation trials and numerous fabrication steps are necessary to obtain good devices. The mesa structures presented here have the advantage of more straightforward fabrication procedures, at the expense of increased dark currents due to surface leakage from the mesa walls.

4.2 Current-voltage measurements

Characterisation of the devices started with dark current measurements as a function of bias voltage. The reverse I-V characteristics from the four wafers are shown in Fig. 4.2. The devices show low dark current values, confirming the good quality and potential for AlGaAsSb as an avalanche material. The I-V characteristics in Fig. 4.2 exhibit an abrupt increase in dark current, indicating dominance of avalanche breakdown. For a given wafer, the values of dark current do not scale with device area, suggesting that at low biases, surface leakage is not completely suppressed. From their forward I-V characteristics, most of the 60 μm diodes exhibited relatively high series resistances due to the small size of the metal contact. The 60 μm diodes where therefore excluded from the subsequent excess noise measurements. From these I-V characteristics, robust devices were selected for the $F(M)$ measurements.

4.3 Capacitance-voltage measurements

Capacitance-Voltage measurements were then performed on the selected devices. The $C(V)$ values are necessary for the $F(M)$ characteristics extraction in part 4.5.3, as explained in part 3.3.3. C-V curves for all four wafers are shown in Fig. 4.3 (a).

The 210 μm devices, exhibiting high capacitance, are excluded from $F(M)$

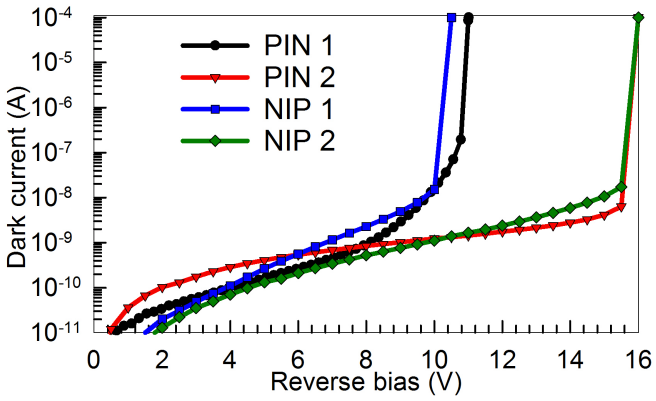

Figure 4.2: *Dark current versus reverse bias of 110 μm radii diodes for all 4 wafers*

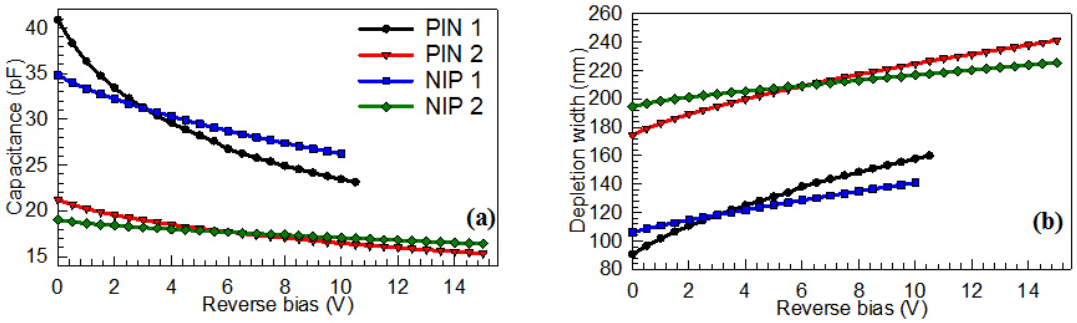

Figure 4.3: *(a) Capacitance-voltage data and (b) calculated depletion width of 110 μm radii diodes of the AlGaAsSb wafers*

measurements due to the limitations on capacitance imposed by the excess noise setup calibration procedure described in part 3.3.3. The depletion widths estimated using Eq. 3.4 are also shown in Fig. 4.3 (b). For all four wafers, the calculated depletion widths are larger than the nominal w values, indicating some depletion into the p- and n-layers. To estimate avalanche layer values, w, the C-V curves are fitted using a 3-layer model assuming a constant doping in each of the p-, i-, and n-layers. The fitted C-V and estimated electric field profiles (using the 3-layer model) at $0.95V_b$ are shown in Fig. 4.4. Values of w obtained from C-V modelling are compared with the corresponding nominal values for each wafer in Table 4.1. Fitted w values are lower than the nominal w values, indicating diffusion of the doping atoms from the p- and n-layers into the i-layer for all four wafers. The precise

doping profiles and actual layer structures will be investigated in part 4.4.

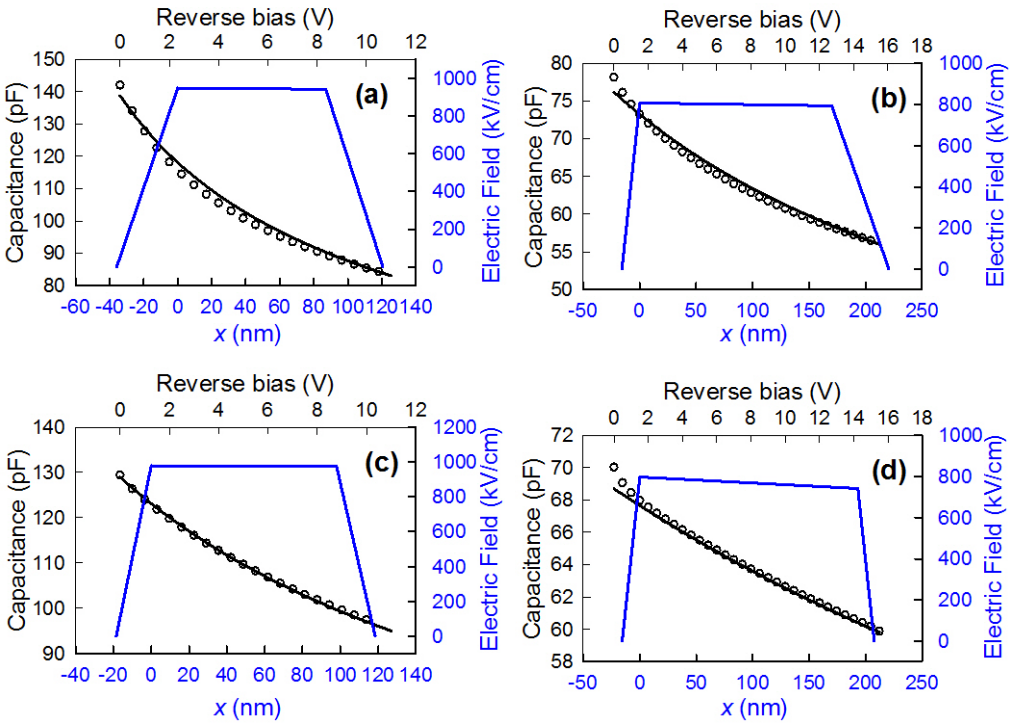

Figure 4.4: *Fitted (black line) vs. experimental (open symbols) C-V. Electric field profile at $0.95V_b$ (blue line) in this model.*

Table 4.1: *Breakdown voltages, nominal and modelled w, capacitance at $0.95V_b$ (for 110 µm radii diodes), and depletion width at $0.95V_b$ of the four AlGaAsSb wafers*

Wafer number	**Wafer name**	V_b **(V)**	**Nominal** w **(nm)**	**Modelled** w **(nm)**	C **at** $0.95V_b$ **(pF)**	**Depletion width at** $0.95V_b$ **(nm)**
SF0921	PIN 1	11.0	100	87	23	160
SF0926	PIN 2	15.9	200	170	15	240
SF0922	NIP 1	10.6	100	98	26	145
SF0929	NIP 2	15.9	200	193	16	225

4.4 SIMS results

To obtain complementary data, Secondary-Ion Mass Spectrometry (SIMS) has been performed on the four bare wafers by Loughborough Surface Analysis. SIMS is a technique that consists in sputtering an incident focussed primary ion beam onto the wafer and analysing the ejected elements by mass spectrometry.

4.4.1 Implanted samples for reference

In order to quantify the SIMS measurements, two calibration samples have been prepared. Those samples were from an undoped InGaAs/AlGaAsSb on InP wafer grown in Sheffield by the National Epitaxy Facility (wafer number SF0993). Layers details are shown in Table 4.2. Prior to implantation, a SiO_2 layer of 19 nm has been deposited onto the wafers by Plasma-Enhanced Chemical Vapour Deposition (PECVD).

Table 4.2: *Layers details for the undoped implanted sample*

20 nm InGaAs cap
500 nm AlGaAsSb undoped
200 nm InGaAs buffer
SI InP wafer

Two pieces of this wafer have been implanted by Prof R. Webb at the Surrey Ion Beam Centre, one with Be atoms, one with ^{130}Te atoms, with the conditions detailed in Table 4.3. The aim was to reach a peak doping concentration of about 5×10^{18} cm^{-3} at around 200 nm from the surface for both doping species. The implant conditions in Table 4.3 were obtained using a Transport of Ions in Matter (TRIM) simulation software [53].

Table 4.3: *Implantation conditions for the Be and the Te implanted samples*

Implanted species	**Implant energy**	**Dose**
Beryllium (Be)	50 keV	1.1×10^{14} cm^{-2}
^{130}Tellurium (Te)	500 keV	7.4×10^{13} cm^{-2}

After removing the SiO_2 layer, the two samples have been analysed by SIMS by Loughborough Surface Analysis. For both the Be and the Te samples, results (Fig. 4.5) show that the implanted species remain within the AlGaAsSb layer, with a peak concentration at about 193 nm below the surface for Be, and 123 nm for Te. Assuming the implant doses are correct, peak concentrations are found to be 5.1×10^{18} cm^{-3} for Be and 4.2×10^{18} cm^{-3} for Te. Those data offer precious information, and are used to relate the number of sputtered ions to an actual doping concentration within AlGaAsSb in the following SIMS results.

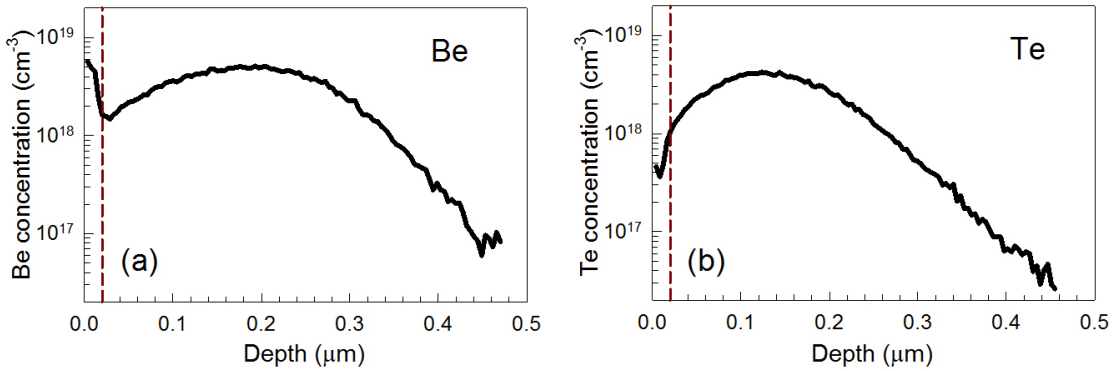

Figure 4.5: *Doping profiles of implanted samples as measured with SIMS. (a) Be implanted sample (b) Te implanted sample. The dotted line indicates the limit of the InGaAs capping layer.*

4.4.2 Doping profiles results

The 100 and 200 nm *p*-*i*-*n* and *n*-*i*-*p* diodes have been analysed using Cs^+ primary ion bombardment and negative secondary ion detection, to optimise the sensitivity to Te. For Be, good sensitivity was obtained using the same conditions, by monitoring the $BeAs^-$ polyatomic species. Two isotopes of Te, ^{126}Te and ^{128}Te, are monitored, and the total concentration of Te atoms is reconstructed taking into account the natural abundance of all Te isotopes. The profiles thus obtained for all four wafers are presented in Fig. 4.6 (a-d).

Thanks to the SIMS calibration described in part 4.4.1, the profiles in Fig. 4.6 give an accurate value of the doping concentrations in the different layers of the wafers. It is to note however that SIMS detects all of the doping atoms inside the wafer. Not all of the doping atoms are electrically active, hence the difference between the doping concentration given by SIMS and the effective doping deduced from *C*-*V* fitting in part 4.3. As a consistency check, the dashed blue lines in Fig. 4.6 show the *i*-region position as obtained from *C*-*V* fitting in part 4.3, showing a good agreement between the fitting and the SIMS results, despite the simplicity of the 3-layer model used. For all four wafers, the SIMS data also show noticeable diffusion of doping atoms into the *i*-layer, consistent with an actual w smaller than the nominal w value for all four wafers.

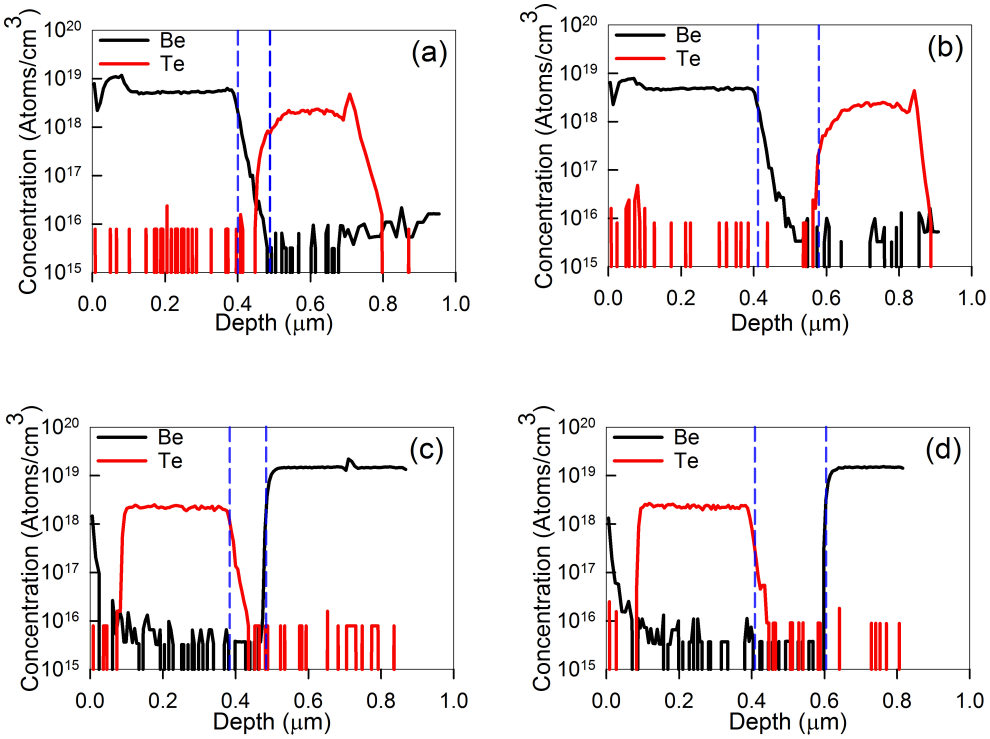

Figure 4.6: *SIMS profile for Be and Te doping for PIN 1 (a), PIN 2 (b), NIP 1 (c), and NIP 2 (d). The dashed line indicates the width of the i-region as deduced from C-V modelling (in 4.3).*

4.5 Gain and excess noise characteristics

4.5.1 Light injection

In this work, three different light sources were used, two He-Ne lasers emitting at wavelengths 633 and 543 nm, and an LED emitting at 420 nm, with 15 nm Full Width at Half Maximum (FWHM) [54]. The different light wavelengths were needed to produce different carrier injection profiles (pure electron, pure hole, or mixed carrier) within the DUT.

To estimate the carrier injection profile for each wavelength, absorption coefficients of AlGaAsSb at 633, 543, and 420 nm wavelengths were estimated by linearly interpolating absorption coefficients of four binary materials, AlAs [55], AlSb [56], GaAs [57], and GaSb [57]. Table 4.4 shows the estimated absorption coefficients and percentage of light absorbed in the top AlGaAsSb cladding layer.

Note that carriers generated by photon absorption in the top InGaAs layer are

Table 4.4: *Estimated AlGaAsSb absorption coefficients and percentage of light absorbed in the top cladding layer for all three wavelengths used*

Wavelength (nm)	**Estimated absorption coefficient (cm^{-1})**	**Percentage of incoming light absorbed in the top AlGaAsSb layer**
633	1.7×10^4	39.7 %
543	5.8×10^4	82.4 %
420	3.0×10^5	99.99 %

excluded from consideration. This is because carriers generated by photon absorption within this InGaAs layer are unlikely to contribute to the photocurrent, due to the large InGaAs/AlGaAsSb conduction band offsets. The reported large conduction band offset between InGaAs and AlAsSb ranges from 0.85 [58] to 1.74 eV [59]. Although the bandgaps of AlGaAsSb [44] are smaller than that of AlAsSb, the conduction band offsets between InGaAs/AlGaAsSb are likely to remain.

From the estimated absorption coefficients in AlGaAsSb, light absorption profiles within the AlGaAsSb layer can be generated, as shown in Fig. 4.7. At 420 nm, pure electron (respectively hole) injection has been achieved in the *p-i-n* (respectively *n-i-p*) APDs.

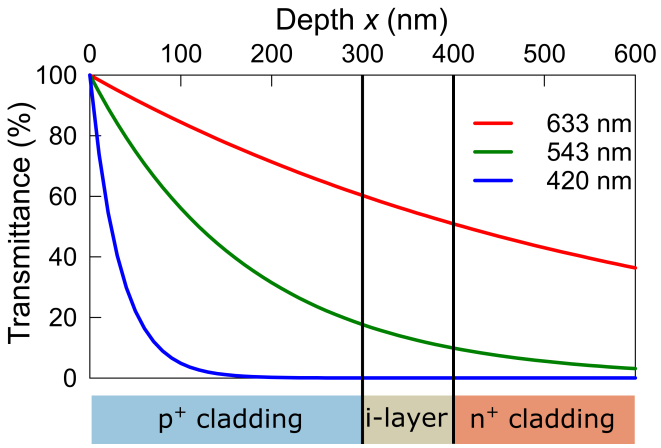

Figure 4.7: *Estimated light absorption profiles within the 100 nm p-i-n device for all three wavelengths*

4.5.2 Avalanche gain

Gain and excess noise were measured using the procedure described in 3.3.1. Data of avalanche gain versus reverse bias for all four wafers, obtained using the

three different wavelengths are compared in Fig. 4.8.

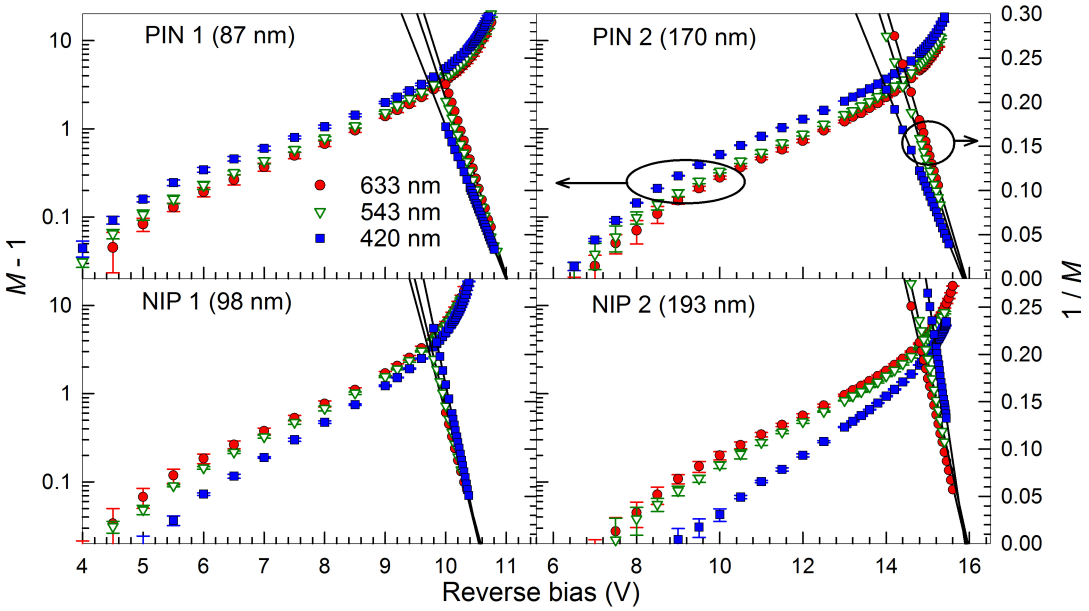

Figure 4.8: *Avalanche gain versus reverse bias characteristics of the four wafers, obtained using wavelengths of 633 (●), 543 (▽), and 420 nm (■). 1/M curves (right axis) are extrapolated to zero to extract V_b.*

The data (taken from 3 to 6 devices per wafer per wavelength) are presented as mean values with error bars indicating the standard deviation. For a given wafer and reverse bias, M increases as the illumination wavelength decreases in the p-i-n diodes, whereas the opposite trend is observed in the n-i-p diodes. In the p-i-n diodes, as the wavelength decreases from 633 to 420 nm, the carrier injection profile changes from mixed carrier injection to pure electron injection, producing larger M. This strongly indicates that the electron ionisation coefficient, α, is greater than the hole ionisation coefficient, β, i.e. $\alpha > \beta$, consistent with [52]. We noted, in particular, that the reduction in M from mixed injection (using 543 and 633 nm), in comparison to pure hole injection (using 420 nm), is more pronounced in diodes with thicker avalanche regions.

Values of breakdown voltages are determined by extrapolating values of $1/M$ to 0, as shown in Fig. 4.8 (right axis), giving $V_b \sim 11.00$, 10.6, 15.9, and 15.9 V for PIN 1, NIP 1, PIN 2, and NIP 2, respectively. These breakdown voltages coincide with voltages where there are abrupt increases in the dark currents in Fig. 4.2.

4.5.3 Excess noise

$F(M)$ characteristics for all four wafers, again obtained using three wavelengths, are shown in Fig. 4.9. In the p-i-n diodes, as the wavelength decreases from 633 to 420 nm, eventually producing pure electron injection profile, the excess noise factor decreases. The opposite trend is observed in the n-i-p diodes. These observations indicate that $\alpha > \beta$, consistent with the data in Fig. 4.8 and prior work [52].

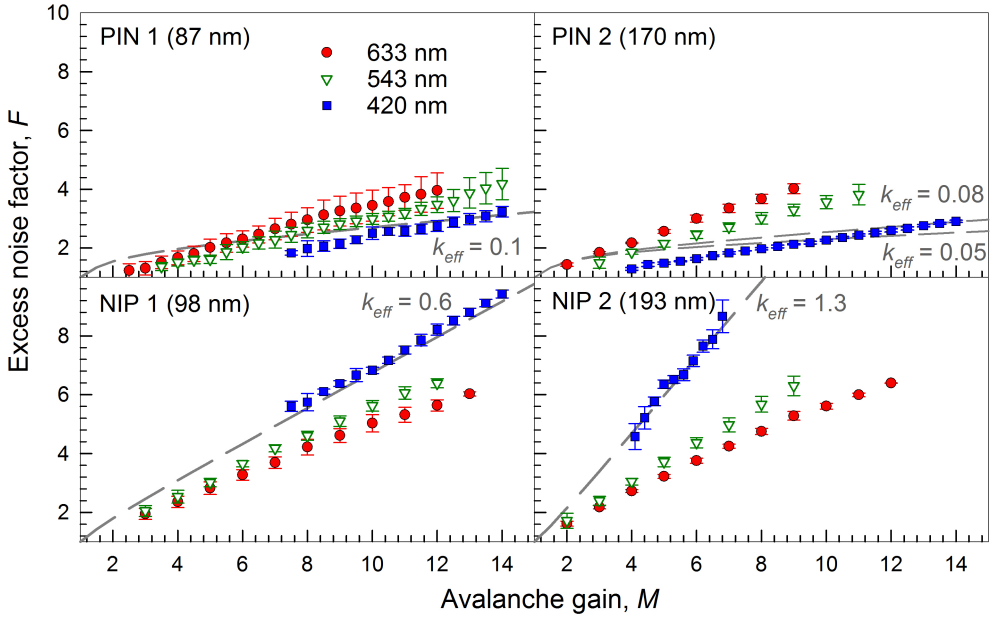

Figure 4.9: *Excess noise factor versus avalanche gain characteristics of the four wafers, obtained using wavelengths of 633 nm (●), 543 nm (▽), and 420 nm (■)*

To aid comparison, data obtained using the 420 nm wavelength light (*i.e.* those with pure electron injection in p-i-n diodes and pure hole injection in n-i-p diodes) are fitted using McIntyre's expression, Eq. 2.2. where k_{eff} was used as adjustable parameter. Reasonable fits were obtained using k_{eff} of 0.1, 0.6, 0.08, and 1.3, for PIN 1, NIP 1, PIN 2, and NIP 2, respectively. As expected from $\alpha > \beta$, the p-i-n diodes under pure electron injection conditions produced the smallest $k_{eff} \sim 0.08$ (best $F(M)$ characteristics). The n-i-p diodes exhibited much higher avalanche noise. Hence, when incorporating AlGaAsSb avalanche regions into SAM APDs, the designs should ensure pure electron injection into the avalanche regions.

Before further $F(M)$ analyses, it is worth recalling the following. The local impact ionisation theory by McIntyre [1] does not include the effects of dead-space,

d. When d is insignificant compared to w, $F(M)$ data obtained from pure electron injection and pure hole injection will yield k_{eff} and $1/k_{eff}$, respectively [1]. Our $F(M)$ data do not conform to this trend. For example, using 420 nm wavelength illumination on PIN 1 produced $F(M)$ data with $k_{eff} = 0.1$, whereas those of NIP 1 yielded $k_{eff} = 0.6$, much smaller than 10 (the value expected from the local impact ionisation theory). This deviation is attributed to the effect of ionisation dead-space in our diodes. Significant effects of non-local impact ionisation (in the form of ionisation dead-space) in narrow avalanche regions have been observed widely (see [24] for review). An attempt of quantification of the dead-space effect is the object of part 4.6.

4.6 Determination of ionisation coefficients

In this part, recurrence equations developed by Hayat *et al.* (as described in part 3.5) were used to simulate the ionisation coefficients for AlGaAsSb using the gain and excess noise results shown above. A simulation programme implementing the recurrence equations was used for the fittings. This programme, written in C language, was already available at Sheffield (written previously by Chee Hing Tan and adapted for this work). The programme is able to generate $M(V)$ and $F(M)$ curves for pure electron and pure hole injection, taking into account the electric field profile of the devices and the ionisation coefficients. The model used is that of *p-i-n* or *n-i-p* diodes with tapered electric field (constant doping in each of the regions). The electric field profiles used are the ones obtained previously in section 4.3 from the C-V fittings, with w values of 87, 170, 98, and 193 nm for PIN 1, PIN 2, NIP 1, and NIP 2 respectively.

The ionisation coefficients for electrons and holes, α^* and β^*, are expressed as

$$\alpha^* = A_e \exp\left[-\left(\frac{B_e}{E}\right)^{C_e}\right],$$

and

$$\beta^* = A_h \exp\left[-\left(\frac{B_h}{E}\right)^{C_h}\right].$$

For a given electric field profile, the programme outputs pure injection $M(V)$

and $F(M)$ characteristics from the values of the eight free parameters, A_e, B_e, C_e, A_h, B_h, C_h, $E_{th,e}$, and $E_{th,h}$. Using the same set of eight parameters, the M and F characteristics of the four wafers, PIN 1, PIN 2, NIP 1, and NIP 2 are generated (*i.e.* eight curves in total). The values of the eight free parameters were adjusted until all eight simulated M and F curves agreed with the experimental results data at 420 nm (*i.e.* pure injection) of all four wafers. Results are shown in Fig. 4.10.

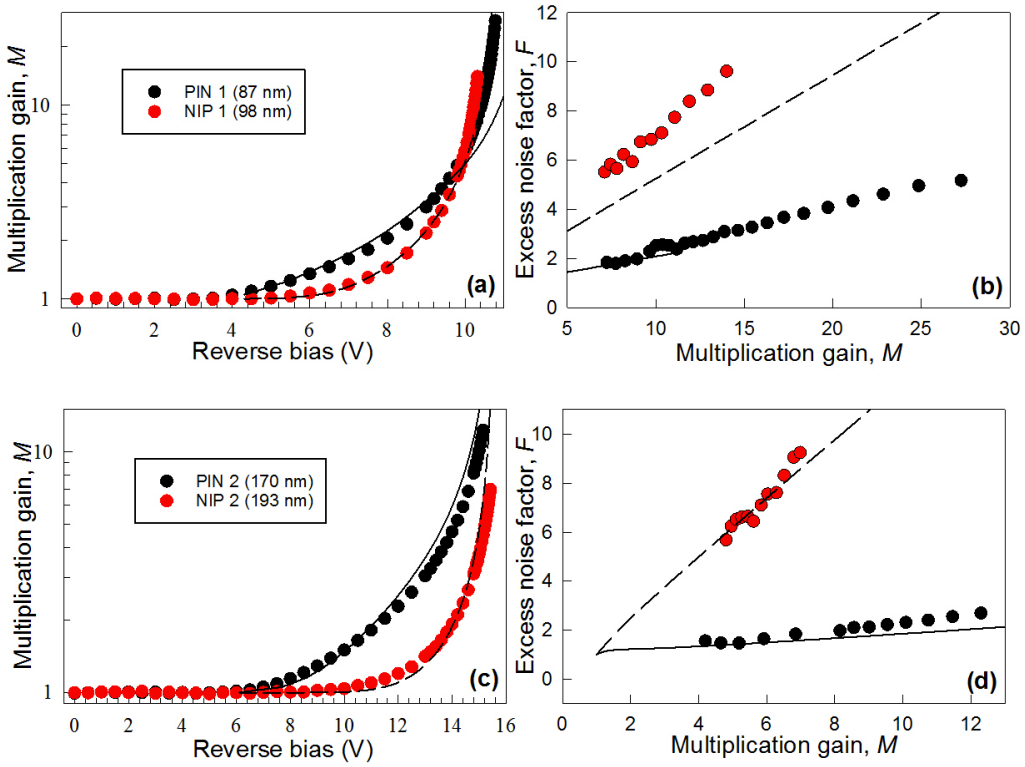

Figure 4.10: *Experimental (symbols) and simulated (lines) M(V) and F(M) results for the 100 nm (a-b) and the 200 nm (c-d) p-i-n and n-i-p devices*

Fig. 4.10 shows reasonably good fits for the 200 nm devices for both $M(V)$ and $F(M)$ data. For the thinner layers, a perfect fit cannot be achieved, and the model slightly underestimates the values of gain and noise. This can be explained by the fact that for thinner layers, a greater uncertainty is present in the electric field and layer thicknesses values obtained from the C-V fitting. Errors of a few nanometres in avalanche thicknesses also have relatively more serious repercussions in very thin layers than in thicker layers. The fact that the same set of eight parameters fails to exactly describe the ionisation coefficients in both the 100 nm and the 200 nm layers also indicates that the simplified model using tapered electric field profiles used here

is to be improved. Nevertheless, the fittings give a good estimate of the ionisation coefficients. Table 4.5 lists the values of the fitting parameters.

Table 4.5: *Parameters used for the fitting*

Parameter	Fitted value
A_e	3.0×10^6 cm^{-1}
B_e	1.25×10^6 V/cm
C_e	1.9
A_h	1.3×10^6 cm^{-1}
B_h	1.35×10^6 V/cm
C_h	2.3
$E_{th,e}$	3.3 eV
$E_{th,h}$	3.4 eV

The coefficients thus extracted are the effective, or enabled ionisation coefficients, α^* and β^*, since the recurrence simulation takes into account the dead-space, via the threshold ionisation energies $E_{th,e}$ and $E_{th,h}$. The local ionisation coefficients, α and β, can be retrieved using the formula in Eq. 2.4. Fig. 4.11 shows the values of α and β extracted from the fitting (black lines). The ionisation coefficients of Si [16] (red circles) and InP [60] (blue lines) are also shown for comparison. In AlGaAsSb, the β/α ratio is remarkably low for the lower end of the field range (right hand side of the figure), with a difference in coefficients of about 2-3 orders of magnitude. This is similar to silicon for this range of fields, consistent with the very low measured excess noise values. This indicates that for thicker devices, AlGaAsSb could possibly yield extremely low excess noise, competing with silicon. For higher fields, k tends to 1, so the very low F values obtained are due to a strong dead-space effect. In comparison, InP has an ionisation rate ratio of $\sim$ 1.5 throughout this range of electric fields. This shows the potential of AlGaAsSb to replace InP for the next generation of low noise APDs. One of the most extreme α/β ratio is found in InAs, with β close to 0 (not plotted here since data are only available for field values $<$ 100 kV/cm). In InAs' case, the very low β value is due to a markedly flat valence band, preventing holes from acquiring enough energy to impact ionise. More knowledge of the band structure of AlGaAsSb (especially at higher energies) is needed to better understand the behaviour of the ionisation coefficients.

In addition, from the fitted values of $E_{th,e}$ and $E_{th,h}$, the values of dead-space can be estimated using Eq. 2.3. Table 4.6 shows the dead-space values for electrons and

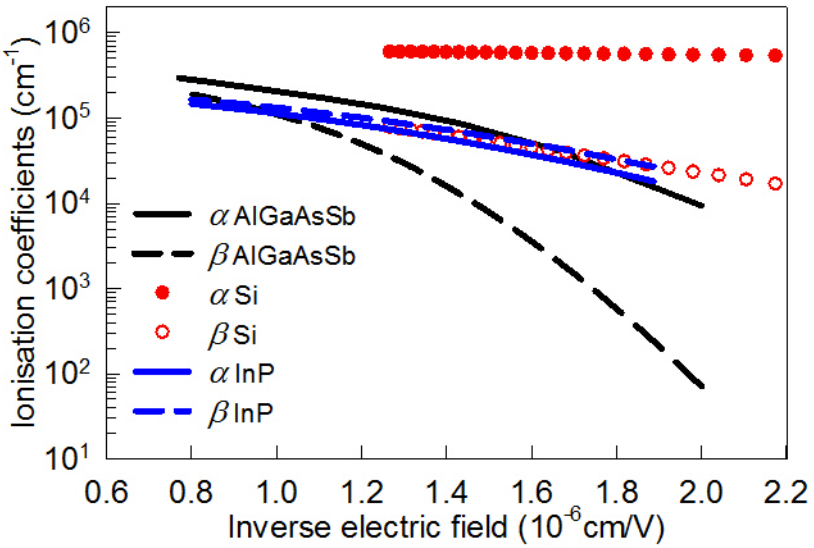

Figure 4.11: *Ionisation coefficients α and β (black lines) obtained from recurrence simulation fitting of the experimental M(V) and F(M) results, plotted versus inverse electric field. Data for Si [16] (red circles) and InP [60] (blue lines) are also shown for comparison.*

holes in nm for all four wafers at $0.9V_b$.

Table 4.6: *Dead-space values for all four wafers, calculated at $0.9V_b$ using the ionisation threshold energies $E_{th,e}$ and $E_{th,h}$ obtained from the fitting*

Device	d_e **at 0.9**V_b **(nm)**	d_h **at 0.9**V_b **(nm)**
PIN 1	29.0	29.9
PIN 2	39.2	40.4
NIP 1	33.9	34.9
NIP 2	44.5	45.9

From Table 4.6, it can be observed that the dead-space values, of about 30-45 nm, account for 23-40 % of the total avalanche width. This significant dead-space explains the small excess noise values measured in the four wafers, and the deviation from McIntyre's law observed in part 4.5.3.

The ionisation coefficients thus obtained need to be interpreted with caution. First, the model used is quite simple, consisting of *p-i-n* and *n-i-p* diodes with constant doping in each layers. The SIMS results in part 4.4 show that the electric field is not perfectly constant in the avalanche region, due to dopant diffusion. The actual electric field is somewhat 'rounded'. To fully take this effect into consideration, more elaborate modelling, such as Monte Carlo simulations could be used. Such

simulations are much more complex and require a number of physical parameters of AlGaAsSb that are not known at the moment.

It is also worth noting that ionisation coefficients are only valid within a certain range of electric fields. In this work, we are limited to the 500 kV/cm to 1.3 MV/cm range, due to the device thicknesses. For a more comprehensive electric field range, a set of thicker diodes would be necessary.

4.7 Conclusions

In this chapter, ultra-thin $Al_{0.85}Ga_{0.15}As_{0.56}Sb_{0.44}$ APDs have been studied. The devices showed low dark currents, and the ability to reach gains up to 20. The influence of carrier injection profile on gain and noise has also been studied, showing that the ionisation coefficient for electrons, α, is greater than that of holes, β.

The 200 nm p-i-n device demonstrated one of lowest excess noise values ever recorded, with $k_{eff} = 0.08$. The graph in Fig. 4.12 shows a comparison of the excess noise factor values at avalanche gain $\sim$ 10 from this work with relevant work based on other avalanche materials. From this graph, it can be seen that thin AlGaAsSb APDs exhibit excess noise values lower than the best values for InP, $In_{0.52}Al_{0.48}As$, and Si, and competitive with $AlAs_{0.56}Sb_{0.44}$ and $Al_{0.7}In_{0.3}As_{0.3}Sb_{0.7}$.

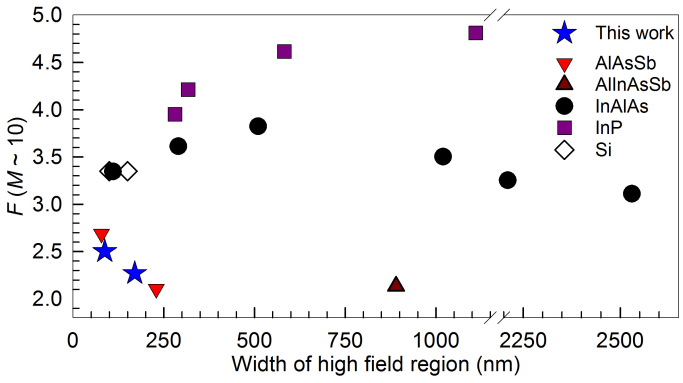

Figure 4.12: *Comparison of excess noise factors at avalanche gain $\sim$ 10 of avalanche diodes made with AlGaAsSb (this work), AlAsSb [29], $Al_{0.7}In_{0.3}As_{0.3}Sb_{0.7}$ [30], InAlAs [27], InP [26], and Si [25]*

In addition, the first ever ion implantation in AlGaAsSb has been reported,

yielding valuable SIMS calibration wafers to obtain doping profiles in this material. This is significant because the implanted samples are of good quality and therefore can serve as a reference for further studies on AlGaAsSb doping. Moreover, this implantation study including TRIM simulations, implant of p- and n-type doping species into a thick undoped layer, and SIMS analysis is a standard procedure that can be reused when moving towards the development of planar diodes. In that case, implantation in InGaAs would be necessary and would have to be studied. Details on the design of planar APDs will be discussed in part 7.2.

Finally, using recurrence simulations, it has been shown that for such thin avalanche region thicknesses, the dead-space effect plays an important role in the reduction of the excess noise.

The combination of low dark current, low excess noise, and high reachable gains, make $Al_{0.85}Ga_{0.15}As_{0.56}Sb_{0.44}$ a suitable material to replace InP and InAlAs avalanche layers in optical communication APDs.

Chapter 5

Effect of carrier injection profile on avalanche noise characteristics

The results presented in the previous chapter demonstrate very low excess noise values ($k_{eff} = 0.08$) for $Al_{0.85}Ga_{0.15}As_{0.56}Sb_{0.44}$ diodes on InP substrate. While these results are of great interest for novel avalanche materials, the effect of carrier injection profile on excess noise factors in such low noise materials has not been studied theoretically.

In this chapter, recurrence equations have been used to generate $F(M)$ characteristics for very small k_{eff} values, and study the influence of light absorption profile on APD noise.

5.1 Study of carrier injection position influence

In this part we study the influence of injection position on excess noise. As a preliminary study, the case of a perfect p-i-n diode with i-region width $w = 1\ \mu m$ and $k_{eff} = 0.01$ is considered. Using recurrence equations (Eqs. 3.17-3.22) from Chap. 3, $F(M)$ was calculated for one electron-hole pair injected at various initial positions (depth) x within the i-region. Fig. 5.1 shows the different injection positions used. No dead-space is used in this model. For a carrier injection at $x = 0$ (*i.e.* at the p/i junction), the characteristic is that of pure electron injection. The case of injection at $x = w$ is equivalent to pure hole injection. Several mixed carrier injection cases are then simulated by injecting an electron-hole pair at $x/w = 0.1, 0.2, ..., 0.5$.

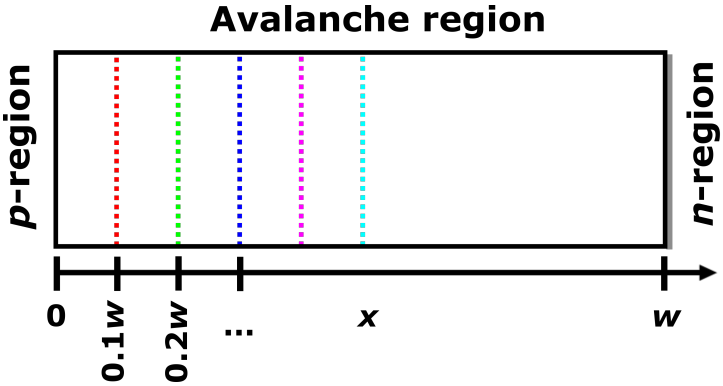

Figure 5.1: *Schematic showing the different injection positions used for the simulations*

For each injection position x, $F(M)$ characteristics have been simulated. The simulated $F(M)$ characteristics are presented in Fig. 5.2. The pure electron injection case, $x = 0$, offers the lowest $F(M)$ values, whereas the pure hole injection case gives the maximum F values. As the injection position increases, more holes (and fewer electrons) are able to initiate impact ionisation events, leading to an increase of the $F(M)$ characteristics. This is consistent with McIntyre's local model theory [1].

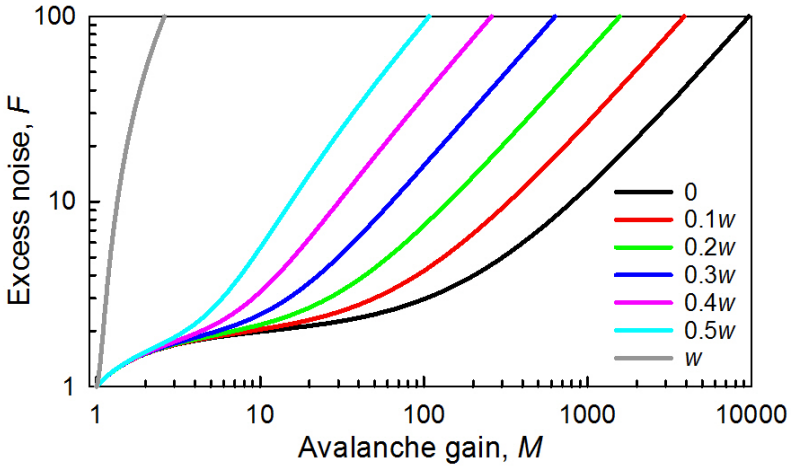

Figure 5.2: *Excess noise factor versus avalanche gain for different injection positions within the i-region of a 1 μm p-i-n diode with $k_{eff} = 0.01$*

As a preliminary check, simulations results for pure electron (injection at $x = 0$) and pure hole injection (injection at $x = w$) are compared with analytical results given by McIntyre's local theory in Fig 5.3. Here again, we use McIntyre's equation, Eq. 2.2. In Eq. 2.2, k_{eff} values of 0.1, 0.01, and 0.001 have been used for pure electron injection. For the pure hole injection case, the corresponding $k' = 1/k_{eff}$

have been used. Fig 5.3 shows perfect agreement between the simulated results and the analytical results in the simple case of pure injection.

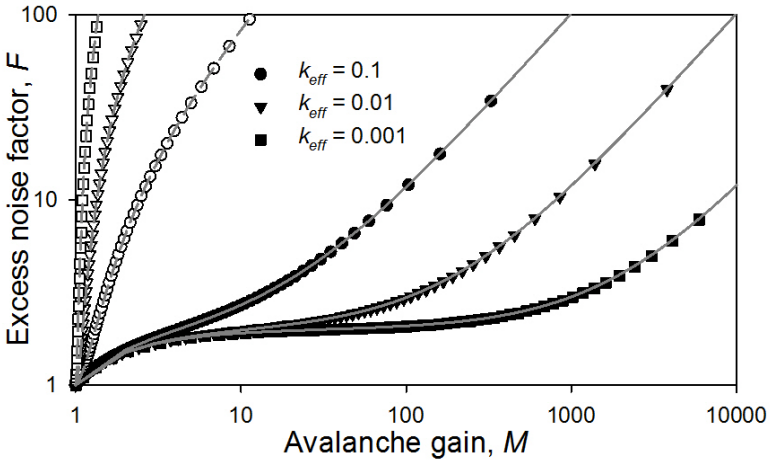

Figure 5.3: *Recurrence simulations for pure electron (closed symbols) and pure hole (open symbols) injection, and McIntyre analytical local model (lines) for k_{eff} = 0.1, 0.01, and 0.001, showing perfect agreement*

5.2 Influence of light absorption profile

To model the wavelength dependence of M and F, the light absorption profile within the p-i-n structure is considered. Since APDs operate at reverse bias and therefore the minority carriers are the ones contributing to the current, photons absorbed in the p-region will be responsible for electron injection, holes will be injected in n-region, and mixed injection will take place in the i-region. The contribution of the i-region is the most critical in the total gain and excess noise.

For incident light at a wavelength λ, the total M and F are calculated by considering all the $M(x)$ and $F(x)$ injection at all positions x within the 3 layers of the device, weighted by the absorption probability, determined by the light absorption profile.

Consider an incident light entering at a rate of A_0 photons/s/unit area from the p^+-side of a p^+-i-n^+ device with p^+, i, and n^+-regions widths of X_p, w, and X_n, as illustrated in Fig. 5.4. Assuming the optical absorption coefficient is ϕ for all three regions, the light decays with x exponentially as given by $A_0 \exp(-\phi x)$.

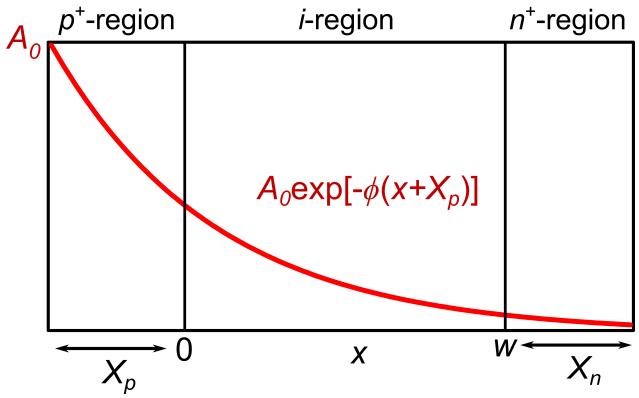

Figure 5.4: *Light absorption in a p^+-i-n^+ device*

The generation rate of carriers within the p^+-region and n^+-region are A_p and A_n, respectively. They are given by [5]

$$A_p = A_0 \left[1 - \exp(-\phi X_p)\right]$$

and

$$A_n = A_0 \exp\left[-\phi(X_p + w)\right] \left[1 - \exp(-\phi X_n)\right].$$

The total multiplied rate of carrier in the diode, A_{total} is the sum of the contributions for all 3 regions, as given by

$$A_{total} = A_p M(0) + \int_0^w M(x) A_0 \phi \exp[-\phi(X_p + x)] dx + A_n M(w),$$

where $M(x)$ and $F(x)$ are the outputs of recurrence simulations used previously. The total mean multiplication M_t is therefore

$$M_t = \frac{A_{total}}{A_{gen}}$$

where A_{gen} is the total unmultiplied carrier rate generation, given by

$$A_{gen} = A_0 \left[\exp\left[-\phi(X_p + w + X_n)\right]\right].$$

For the excess noise, the shot noise of an APD is considered, and the total mean excess noise factor can be similarly derived. The full derivation can be found in [5]

and [61].

The diffusion lengths of the carriers are assumed to be larger than the cladding layers widths so that all the electrons created in the p-region, and all the holes created in the n-region diffuse into the i-region.

In this part, the simulated device is a p^+-p^--n^+ diode with tapered electric field (constant doping level in each of the layers). Layer characteristics are shown in Table 5.1. No dead space is used.

Table 5.1: *Layer characteristics of simulated devices*

p^+-layer	p^--layer	n^+-layer
$X_p = 300$ nm	$w = 1$ μm	$X_n = 100$ nm
Doping 5×10^{18} cm^{-3}	Doping 5×10^{15} cm^{-3}	Doping -5×10^{18} cm^{-3}

The electron ionisation coefficient α is arbitrarily taken to be

$$\alpha = 0.78 \times 10^8 \exp\left[-\left(\frac{1.25 \times 10^8}{E}\right)^{1.5}\right] \text{cm}^{-1}$$

whereas the hole ionisation β coefficient is

$$\beta = k_{\mathit{eff}}\alpha.$$

Three absorption profiles within the devices, corresponding to three wavelengths, 633, 543, and 420 nm, are considered. These three different absorption profiles will create three different carrier injection conditions within the simulated devices. These profiles are shown in Fig. 5.5. They are based on the estimated absorption coefficients of $AlAs_{0.56}Sb_{0.44}$ (extrapolated from the binary compounds as in part 4.5.1), namely 358, 2.52×10^4, and 2.67×10^5 cm^{-1} for $\lambda = 633$, 543, and 420 nm respectively.

The simulated $F(M)$ characteristics for $k_{\mathit{eff}} = 0.01$ are compared in Fig. 5.6. For a fixed avalanche gain, F decreases as the wavelength decreases. The light absorption profile for 420 nm wavelength produces nearly pure electron injection, hence its $F(M)$ characteristics is undistinguishable from that of pure electron injection. Even with the most severe mixed injection (633 nm wavelength), very small excess noise factors were obtained ($F < 5$ for gains up to 30), owing to the very low value of k_{eff}.

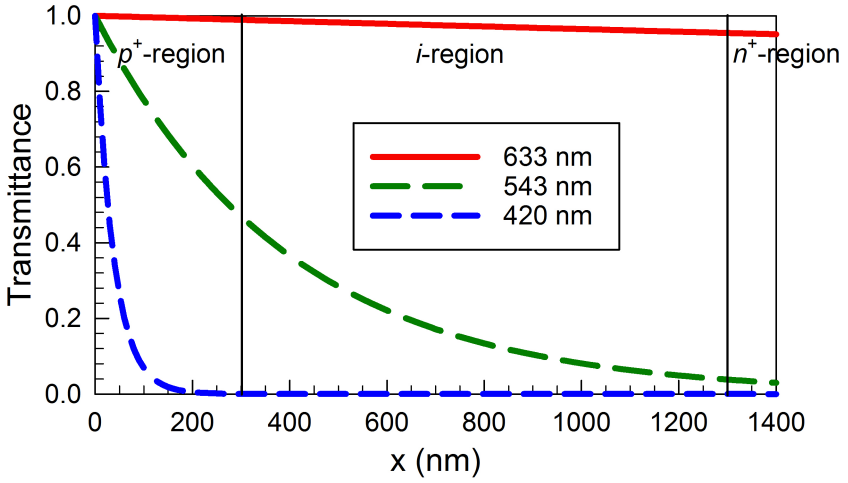

Figure 5.5: *Three absorption profiles used in the simulations of F(M) characteristics*

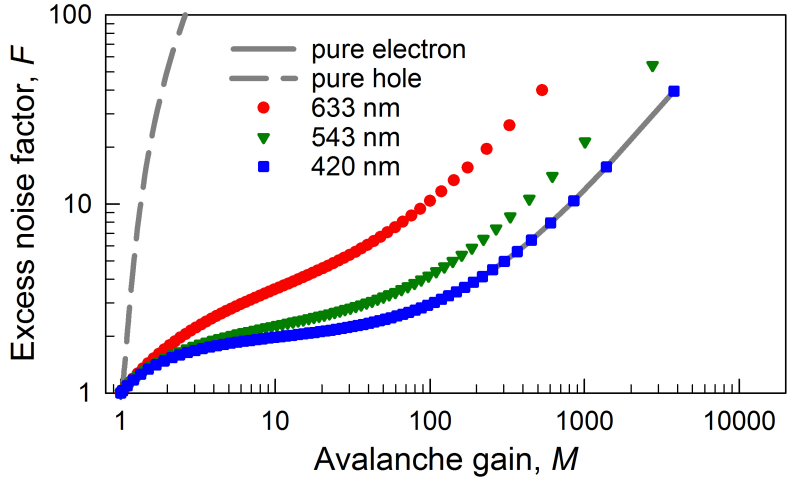

Figure 5.6: *Simulated excess noise factors versus avalanche gain for three different light absorption profiles, for k_{eff} = 0.01. Results for pure electron and hole injections are included for reference (lines)*

.

Fig. 5.7 shows $F(M)$ characteristics for k_{eff} = 0.1, 0.01, and 0.001 for the three different wavelengths. For pure electron injection (λ = 420 nm), the excess noise remains relatively constant with M up to $\sim$ $1/k_{eff}$, before increasing sharply. The mixed injection curves differ markedly from the pure injection ones. The reason for this difference in the $F(M)$ curves is investigated in the next part.

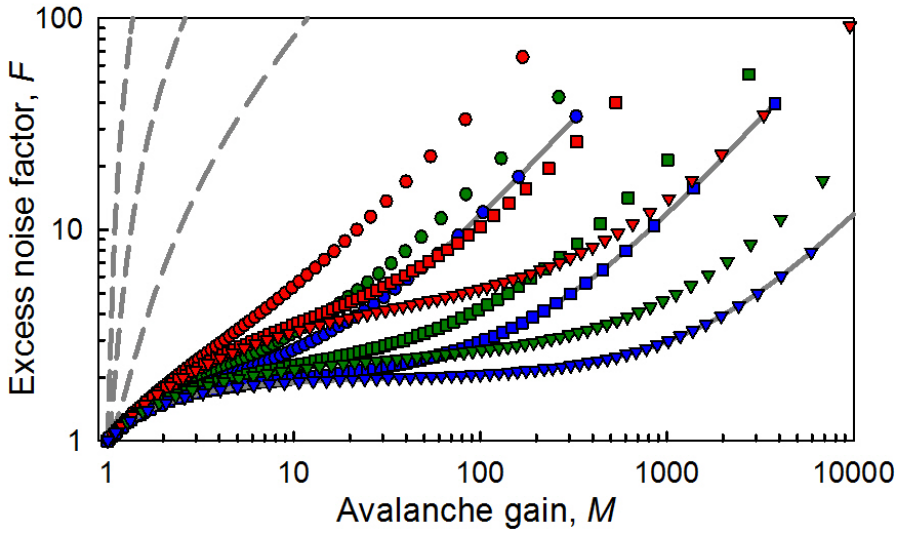

Figure 5.7: *Simulated excess noise factors versus avalanche gain for k_{eff} = 0.1 (●), 0.01 (■), and 0.001 (▼). The colours correspond to the wavelength (red=633 nm, green=543 nm, blue=420 nm). Results for pure electron and hole injections are included for reference (lines)*

5.3 Influence of ionising carrier type on excess noise

In this part, a RPL model is used [3], to complement the recurrence simulation results. This model assumes the same PDFs for the carriers than the recurrence equations (see part 3.5), but instead of using statistical considerations globally on the carriers, each carrier is assigned a random survival probability, leading to a random ionisation path length, x_e, given by

$$x_e = d_e - \frac{\ln(r)}{\alpha^*}$$

for electrons, where r is a random number ($0 < r < 1$). A similar value for the holes is also obtained, using x_h, d_h, and β^* instead of x_e, d_e, and α^* respectively. For each trial, the number of carriers is counted and the programme outputs M and F as the average values over many trials.

In a RPL model the number of carriers collected at the terminals are tracked for each trial to produce the M value. Using additional counters, the RPL model was modified to track the number of impact ionisation events initiated by electrons, n_e,

or by holes, n_h. Since in the simulations the ionisation coefficients have been chosen such that $\alpha \gg \beta$, electrons will ionise much more easily than holes, and therefore contribute significantly less to the excess noise.

The pure injection simulations from the previous part were repeated, this time using the RPL model. Fig. 5.8 shows the output of the simulations for $k_{eff} = 0.1$, 0.01, and 0.001. Each graph plots the value of the simulated excess noise (right axis, blue lines) and the number of electron-induced (n_e) and hole-induced (n_h) ionisation events as a ratio (left axis, black lines) versus M. As a comparison, the theoretical $F(M)$ curve for $k_{eff} = 0$ is added to each plot (dashed grey curve).

It can be seen in Fig. 5.8 that, for the same gain M, the ratio n_h/n_e becomes smaller as k_{eff} gets smaller, as expected since the discrepancy between the ionisation coefficients α and β becomes greater.

Fig. 5.8 also clearly shows, for a given k_{eff}, that the ratio of ionising holes to ionising electrons increases with M. For the small M values, the ratio is very small, indicating impact ionisation events are mostly initiated by electrons (that ionise more easily due to a greater α). Hence F closely follows the theoretical $F(M)$ curve for $k_{eff} = 0$. For $M > 1/k_{eff}$, the ratio of ionising carriers rises, so $F(M)$ starts to increase and diverge from the $k_{eff} = 0$ curves, as more and more holes start to ionise.

5.4 Consequences on performances of APD-based detection circuits

In sections 5.2 and 5.3, the simulations explored the $F(M)$ characteristics for materials with very low k_{eff}. Effects of these very low $F(M)$ characteristics on the Signal-to-Noise Ratio (SNR) of a detection circuit utilising such APDs are investigated here.

The SNR of an APD-based detection circuit is given by [62]

$$SNR = \frac{(P_0 R)^2 M^2}{N_s M^2 F(M) + N_{amp}}, \tag{5.1}$$

where P_0 is the incident light power, R is the APD responsivity, N_{amp} is the amplifier

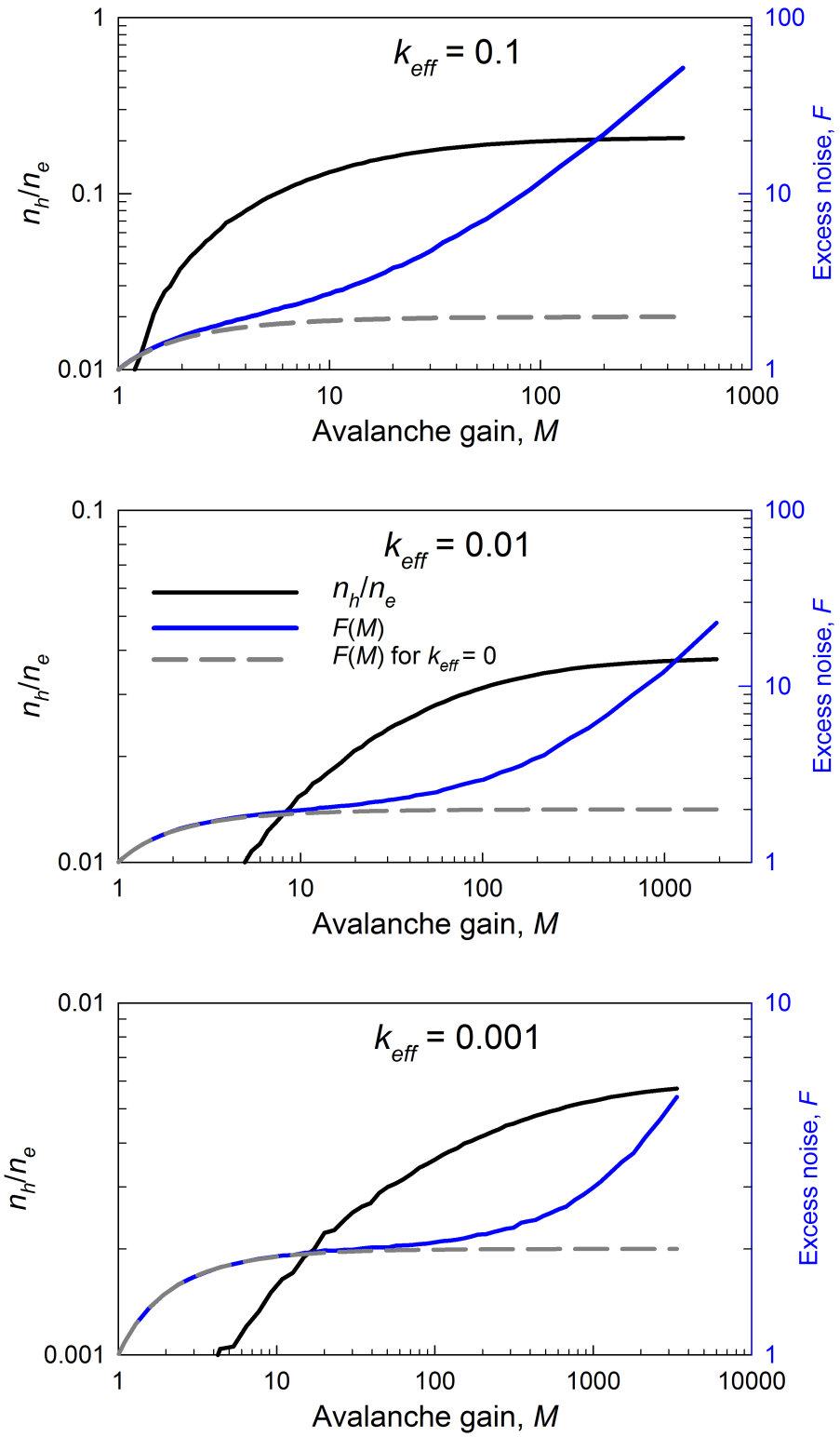

Figure 5.8: *Ratio of hole-initiated to electron-initiated impact ionisation events (left axis, black lines), and simulated excess noise versus avalanche gain (right axis, blue lines) for k_{eff} = 0.1, 0.01, and 0.001. F(M) for k_{eff} = 0 has been included for reference (grey dashed line).*

(TIA) noise, and N_s is the diode shot noise at unity gain, given by

$$N_s = 2q(I_d + I_{pr})B_{eff}. \tag{5.2}$$

Using Eqs. 5.1 and 5.2 and rearranging the terms, the SNR can be written as

$$SNR = \frac{(P_0 R)^2}{2qB_{eff}(I_d + I_{pr})F(M) + N_{amp}/M^2}. \tag{5.3}$$

Generally, amplifier noise levels are characterised using current-noise spectral density, n_{amp}, given as

$$n_{amp} = \sqrt{\frac{N_{amp}}{B_{eff}}},$$

with unit A/$\sqrt{\text{Hz}}$.

From Eq. 5.3, low excess noise is beneficial for achieving a large SNR. For high speed applications, the term N_{amp} usually dominates, thus operating APDs at high gains improves the SNR (by reducing the N_{amp}/M^2 term). For example, for optical communications, efforts have been made to develop TIAs performing at 40 Gb/s with the lowest possible noise. For these high speed devices, typical amplifier noise levels are 10s of pA/$\sqrt{\text{Hz}}$. Typical values found in literature range between 14 pA/$\sqrt{\text{Hz}}$ [63, 64] and 55.7 pA/$\sqrt{\text{Hz}}$ [65]. Researchers are also preparing the next generation optical communications operating at 100 Gb/s. Amplifiers for this ultra-high speed technology are already available [66], but keeping the noise level low is challenging.

Using Eq. 5.3 and pure electron injection $F(M)$ characteristics from Fig. 5.8 (k_{eff} = 0.1, 0.01, and 0.001), values of SNR versus M were calculated. Fig. 5.9 shows the estimated SNR (normalised to the bandwidth, with $(I_d + I_{pr})$ fixed at 1 nA), plotted for n_{amp} = 1, 10, and 100 pA/$\sqrt{\text{Hz}}$.

The results show that the overall SNR decreases when the amplifier noise increases, as expected. The SNR decreases by about an order of magnitude when the amplifier current-noise increases by an order of magnitude. We also note that the maximum SNR value occurs at higher M as the amplifier noise increases. For k_{eff} = 0.001, the SNR reaches its maximum value at respectively $M \sim$ 180, 890, and 4100 for amplifier current-noises of 1, 10, and 100 pA/$\sqrt{\text{Hz}}$. This highlights the importance

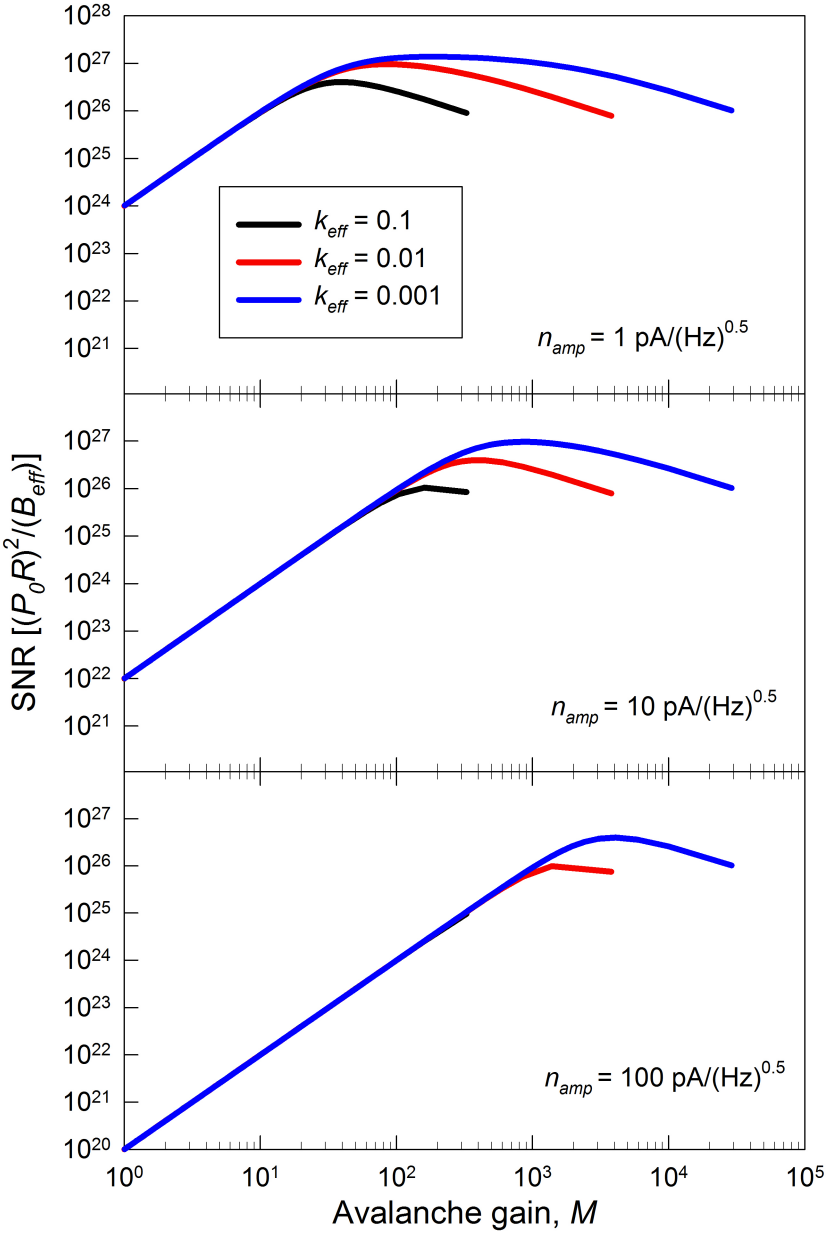

Figure 5.9: *SNR values for k_{eff} = 0.1, 0.01, and 0.001, for 3 different values of amplifier noise n_{amp} = 1, 10, and 100 pA/$\sqrt{Hz}$ (top, middle, and bottom)*

of using avalanche gain to compensate amplifier noise.

Advantages of very low k_{eff} materials clearly show at higher avalanche gains: the decrease of SNR values at high gains is slower for materials with low k_{eff}. For the lowest amplifier noise level, at $M = 10^3$, the SNR for $k_{eff} = 0.001$ is about one order of magnitude higher than that for $k_{eff} = 0.01$.

The SNR, however, is not the most commonly used figure of merit to quantify the performances of APDs. A more used quantity is the Noise-Equivalent Power

(NEP), defined as the optical signal power giving a SNR of 1 in a 1 Hz output bandwidth. It is therefore the minimum detectable light power, normalised to the detector bandwidth. This means that the lower the NEP value is, the more sensitive the detector. Equating Eq. 5.3 to 1 yields

$$NEP = \frac{P_0}{\sqrt{B_{eff}}} = \frac{1}{R}\left(\sqrt{2q(I_d + I_{pr})F + \frac{{n_{amp}}^2}{M^2}}\right), \tag{5.4}$$

with NEP in units $\mathrm{W}/\sqrt{\mathrm{Hz}}$. The NEP corresponding to the SNR values calculated in Fig. 5.9 are shown in Fig. 5.10. The responsivity R is assumed to be 1 A/W.

The NEP has opposite variations from the SNR, reaching a minimum for M values for which the SNR is maximum, as expected. NEP can reach minimum values of the order of 10^{-14} $\mathrm{W}/\sqrt{\mathrm{Hz}}$ at the optimal avalanche gain. Values found in literature corroborate these estimates. For example, the Si-on-Ge SAM APD discussed in Chap. 2 exhibits a NEP of 1×10^{-14} $\mathrm{W}/\sqrt{\mathrm{Hz}}$ at 1310 nm when cooled to 100 K, and operating in the so-called Geiger mode (biased over V_b with short voltage pulses) [37]. Values as low as 6×10^{-16} $\mathrm{W}/\sqrt{\mathrm{Hz}}$ have been reported in InGaAs/InP devices, also operating in a Geiger (photon counting) mode [67]. This was favoured by very low dark current values (a few pA) when cooled down to 200 K, and good photon absorption properties.

The experimental results in Chap. 4 as well as the simulation results in 5.2 show that the NEP is strongly dependent on the wavelength, via the carrier injection profile dependence of M and F. Optimal NEPs are therefore conditioned to pure electron injection in materials with $\alpha > \beta$, meaning shorter wavelengths are beneficial. However, the responsivity R of semiconductor materials tends to drop sharply at shorter wavelengths, due to absorption of incident light closer from the surface of the material, degrading the NEP. This is not an issue for SAM APDs, for which the absorption material and the multiplication material are distinct. In that case, the responsivity value R appearing in the formulas in Eq. 5.3 and 5.4 takes into account the absorption efficiency of the absorber and the efficiency of the charge transfer between absorption and avalanche material. According to the context and applications, the responsivity values can be given as part of the quantum efficiency (QE), or single-photon detection efficiency (SPDE) in the case of single-photon

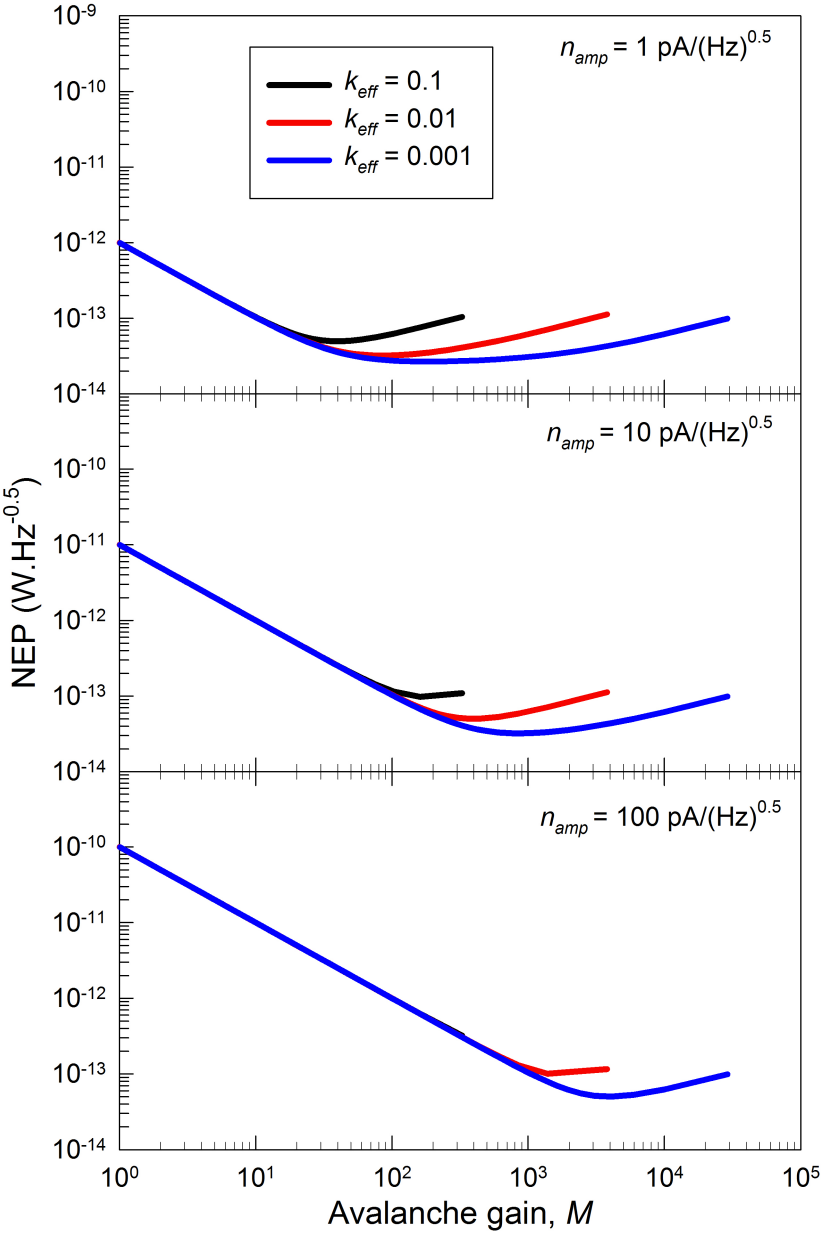

Figure 5.10: *NEP values for k_{eff} = 0.1, 0.01, and 0.001, for 3 different values of amplifier noise n_{amp} = 1, 10, and 100 pA/$\sqrt{Hz}$ (top, middle, and bottom)*

detectors.

5.5 Conclusions

In this chapter, the influence of carrier injection profile on the excess noise of very low k_{eff} materials have been investigated, using recurrence simulations. Results show that avalanche materials with very low k_{eff} values can produce very good

excess noise characteristics even under non-optimal injection conditions. The shape of the $F(M)$ characteristics has been explained using RPL simulations, tracking the number of carrier pairs created during successive impact ionisation events. The results indicate that for very small values of k_{eff}, the $F(M)$ characteristics remain close to the theoretical curves for $k_{eff} = 0$ at low gains, since impact ionisation events are initiated mostly by electrons. For higher gain, more holes are able to impact ionise, inducing a fast increase in excess noise. Finally, SNR and NEP values have been calculated using the previously simulated F and M values, highlighting the interest of using very low excess noise APDs for the detection of very weak light signals.

Since low k_{eff} materials are the focus of interest and actively sought by researchers, a better understanding of their behaviour at high gains is necessary. This chapter was therefore aimed to provide a graphic way to visualise the interdependence relationship between gain, noise, and detection efficiency of APDs using low k_{eff} materials.

These simulation results also provide abacus-like reference curves for the SNR and the NEP (displayed in Figs. 5.9 and 5.10), to guide the user in the choice of APD/preamplifier systems according to the desired applications. Knowing data like $F(M)$ characteristics of APDs and noise level of preamplifiers, that can be easily found in the manufacturer's data sheet, SNR and detection efficiency can be obtained using the curves in Figs. 5.9 and 5.10.

The wavelength-dependent calculations performed here also further highlight the fact that design of APDs should focus on ensuring pure electron injection (if $\alpha > \beta$). This is especially significant for optical telecommunications APDs, since 1550 nm wavelength light can be absorbed in several layers of the device other than the absorber due to its low energy, and therefore induce mixed injection into the avalanche layer. APDs for optical communications are normally SAM APDs, with two distinct materials for the absorption and the avalanche layers. A thick absorber needs to be designed and care has to be taken to avoid the absorption of light into the avalanche layer (or other layers), to reduce mixed injection to a minimum. Fortunately, avalanche regions normally use wide-bandgap materials that cannot absorb long wavelengths. The next chapter presents details on the design and operation of such a device. An InGaAs/AlGaAsSb SAM APD designed to operate

at 1550 nm, comprising a thick absorption region and a thin avalanche layer for optimum performances, will be studied.

Chapter 6

Temperature dependence of InGaAs/AlGaAsSb SAM APDs

As demonstrated in Chap. 4, thin AlGaAsSb avalanche regions exhibit very low excess noise values. For efficient absorption at 1550 nm, $In_{0.53}Ga_{0.47}As$ (lattice-matched to InP) is a material of choice. InGaAs/AlGaAsSb SAM APDs have actually demonstrated record high GBPs of more that 400 GHz [43]. In this chapter, the temperature dependence of dark current and gain of an InGaAs/AlGaAsSb SAM APD with a 100 nm avalanche region is studied.

6.1 Device structure and fabrication

The wafer used is a SAM APD structure, with a 1000 nm $In_{0.53}Ga_{0.47}As$ (thereafter InGaAs) absorber, and a 100 nm $Al_{0.85}Ga_{0.15}As_{0.56}Sb_{0.44}$ (thereafter AlGaAsSb) avalanche layer. It was grown by MBE on semi-insulating InP substrate by the National Epitaxy Facility in Sheffield. The wafer number is SF0837. A highly doped charge sheet in between the absorption and the multiplication layers is designed to control the electric field, keeping it low in the narrow-bandgap absorption region to avoid tunnelling currents, and high inside the multiplication layer to initiate impact ionisation. Two AlGaInAs grading layers are inserted in between the $In_{0.52}Al_{0.48}As$ (InAlAs) cladding and the absorber, and in between the absorber and the charge sheet to gradually reduce the bandgap step between InGaAs and InAlAs. Finally, a 100 nm InGaAs capping layer protects against oxidation from air. Details of the

layers are given in Table 6.1.

Table 6.1: *Layer structure of the SAM APD wafer*

Layer	Material	Thickness (nm)
p^+ cap	InGaAs	100
p^+ cladding	InAlAs	300
Grading	InAlAs	50
	AlGaInAs	25+25
Absorber	InGaAs	1000
Grading	AlGaInAs	25+25
	InAlAs	25
	AlGaAsSb	25
p^+ charge sheet	AlGaAsSb	47
i multiplication	AlGaAsSb	100
n^+ cladding	AlGaAsSb	200
n^+ etch stop	InGaAs	300

A schematic of the structure and intended electric field profile is shown in Fig. 6.1. Details about the design choices of this structure are given below. The design of this SAM APD includes a very thin 100 nm AlGaAsSb avalanche region, to benefit from the very low excess noise demonstrated in Chap. 4.

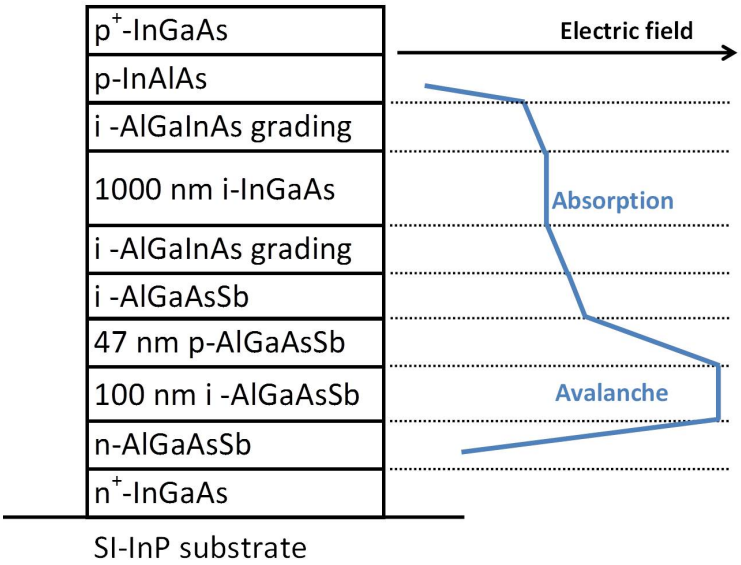

Figure 6.1: *Mesa structure diagram and intended electric field profile*

The absorption layer needs to be thick enough to efficiently absorb the incoming light at 1550 nm. However, a thick layer will introduce more bulk dark currents due to the increasing number of defects within the materials. Also, a thicker device will

be slower, reducing the bandwidth. In addition, with too thick an absorption layer, there is a risk of the device not being fully depleted if low background doping is not achieved. So a trade-off is necessary in the choice of the absorption layer thickness. Fig. 6.2 shows the percentage of 1550 nm light absorbed in InGaAs as a function of material thickness, using absorption coefficients given in [68]. The choice of 1 μm was made, offering a good compromise between good absorption efficiency (55% of incoming light is absorbed) and relatively small thickness (therefore retaining high speed capacities).

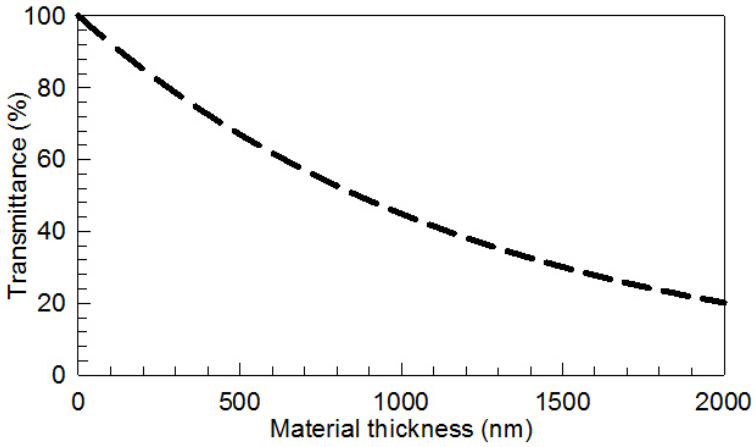

Figure 6.2: *Absorption of 1550 nm light in InGaAs as a function of material thickness*

The electric field level in the absorption region is also of prime importance. Given the narrow bandgap of InGaAs, band-to-band tunnelling will increase the dark current in the device if the electric field is too high. Previous studies on InGaAs diodes showed that the dark current due to band-to-band tunnelling becomes significant, with calculated level around 0.4 A/m^2 (= 40 μA/cm^2), for electric fields as low as 200 kV/cm in InGaAs layers of thickness around 1 μm [69]. The electric field in the absorption region therefore needs to be kept below that value.

The values of V_p and V_b are also important. Avalanche breakdown should take place at a reasonably low voltage for practical use. V_p and V_b must also be far enough apart to ensure the device is fully depleted when the electric field in the avalanche region reaches the breakdown value. The electric field in the absorption region should indeed be sufficient to ensure carrier transportation across the device. However, as seen earlier, the electric field value in the absorption region should stay below

200 kV/cm to avoid high tunnelling currents. Therefore, the design of the charge sheet is highly critical. Considering all the above restrictions, stringent requirements are placed upon the design of the charge sheet. To aid design, simulations can be done beforehand to determine the correct thickness and doping level of the charge sheet.

The electric field profile in the device can be modelled using Poisson's equation (Eq. 3.5). Fig. 6.3 shows modelled values of V_p and V_b, as well as the electric field value in the absorption region calculated for different charge sheet thicknesses (a), and doping levels (b), using the nominal values of thicknesses and doping levels for all the other layers, as in Table 6.1. For Fig. 6.3 (a), the doping level is set constant at 1.0×10^{18} cm^{-3}, in Fig. 6.3 (b), the thickness is set constant at 47 nm. V_b has been taken to be the voltage for which the electric field value in the avalanche region reaches 1 MV/cm, consistently with results obtained on 100 nm AlGaAsSb devices in Chap. 4. Fig 6.3 shows that a variation of 2 nm in the charge sheet thickness from 47 to 49 nm leads to a drop of more than 15% in the absorption region electric field (from 254 to 221 kV/cm). Even more critically, an error of 10% in the charge sheet doping level (1.1 instead of 1.0×10^{18} cm^{-3}) induces a 30% error (a drop from 254 to 177 kV/cm) in the absorption layer electric field. The layer thickness-doping level product is therefore critical for the SAM APD design. Note that the values of thickness and doping level chosen for the design of the charge sheet, namely 47 nm and 1.0×10^{18} cm^{-3}, yield to a simulated electric field in the absorption region of 250 kV/cm. This is higher than the 200 kV/cm limit discussed above, and is intended to be a safety margin to avoid incomplete depletion of the device in case of a discrepancy between the nominal parameters and the real values after growth.

As stated previously, a large conduction band offset exists between InGaAs (E_g = 0.75 eV) and InAlAs (E_g = 1.55 eV) that could impede the transport of electrons across the device. To reduce the energy barrier, two undoped AlGaInAs grading layers are inserted in between InGaAs and InAlAs layers. Fig. 6.4 shows the position of the quaternary alloy $Al_xGa_yIn_{1-x-y}As$ in a bandgap versus lattice constant chart (red zone). To be lattice-matched to InP, the coefficients in $Al_xGa_yIn_{1-x-y}As$ must satisfy the relation $1 - x - y = 0.53$ [70]. This is illustrated by the red dashed line in Fig. 6.4. Along this line, two intermediate alloy compositions, namely

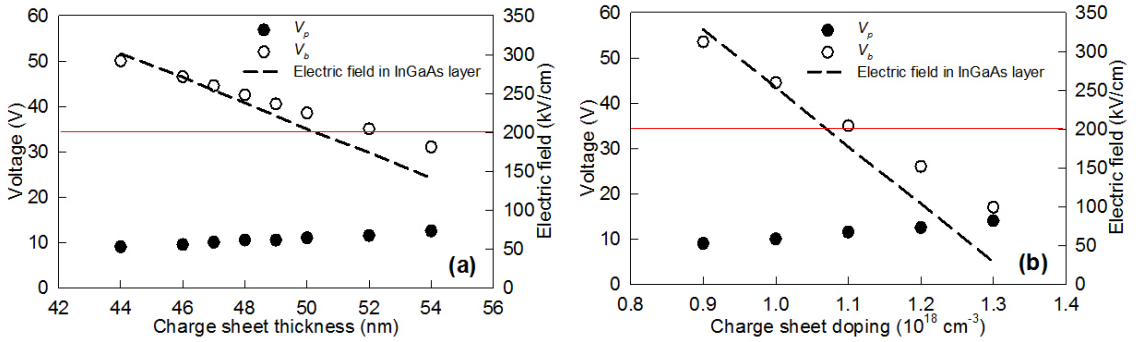

Figure 6.3: *Simulated V_b, V_p, and electric field level in absorption region for different (a) charge sheet thicknesses and (b) doping levels*

$Al_{0.13}Ga_{0.34}In_{0.53}As$ ($E_g \sim 0.95$ eV [70]) and $Al_{0.27}Ga_{0.2}In_{0.53}As$ ($E_g \sim 1.17$ eV [70]), in between InGaAs and InAlAs (shown by the blue dots) have been chosen to provide two intermediate bandgap layers to reduce the energy step for the electrons, thus helping a smoother transition between narrow and wide-bandgap materials. A flat-band diagram detailing the different grading layers (in between the absorption layer and the charge sheet) is shown in Fig. 6.5, summarising the bandgap values of the different materials. The reported conduction band offset between InGaAs and InAlAs is around 0.5 eV [71]. Note that the values of the conduction band offsets are not known precisely for the quaternary materials, nor are the valence band steps, consequently the diagram is not to scale.

Finally, it is worth noting that, given the wide bandgaps of AlGaAsSb ($E_g \sim$ 1.56 eV) and InAlAs ($E_g = 1.55$ eV), their cut-off wavelengths are close to 800 nm. Therefore, light at 1550 nm is only absorbed in the InGaAs absorption layer. Under reverse bias, the design ensures that only the electrons created in the InGaAs absorption region are swept toward the avalanche layer. Electron injection into the avalanche layer is therefore ensured. This is highly desirable according to the results in the previous two chapters.

The wafer is fabricated, using chemical etching, into mesa devices of four different radii, namely 210, 110, 60, and 35 μm, as in Chap. 4. Different etching solutions were used for the different materials, as summarised in Table 6.2. Ti-Au metal contacts were also deposited, as in Chap. 4. No passivation layer or anti-reflective coating were applied to the devices.

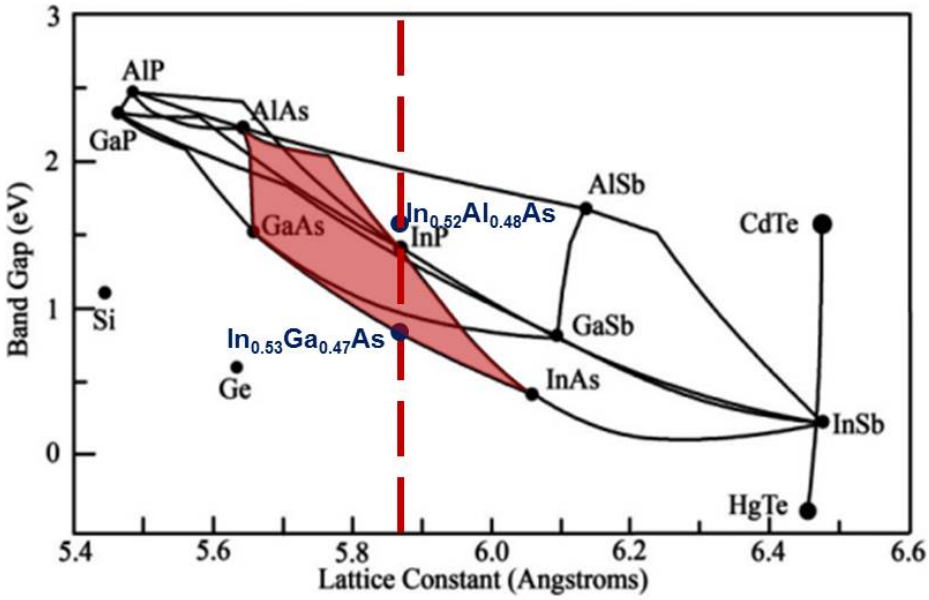

Figure 6.4: *Bandgap versus lattice constant diagram for common semiconductors. The red area corresponds to $Al_xGa_yIn_{1-x-y}As$, the red dashed line shows the lattice constant of InP.*

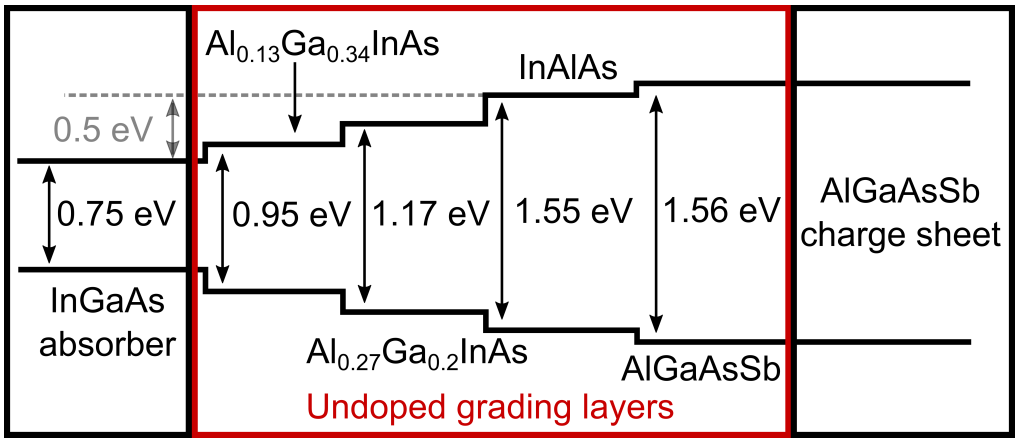

Figure 6.5: *Flat-band diagram of the different materials used in the successive grading layers between the InGaAs absorption layer and the AlGaAsSb charge sheet*

Table 6.2: *Etching solutions used for each material. DIW stands for de-ionised water.*

Material	Etching solution
InGaAs	$C_6H_8O_7$:H_2O_2 (2:1)
InAlAs	H_2SO_4:H_2O_2:DIW (1:8:80)
AlGaAsSb	HCl:H_2O_2:DIW (5:1:50)

6.2 Room temperature *I-V* and *C-V*

To assess the quality of the devices, I-V measurements were performed on several diodes of each size, using an AGILENT B1505A Device Analyser. The I-V characteristics obtained are shown in Fig. 6.6. The I-V curves show two different regimes under reverse bias. At low voltages (below 16 V) the I-V characteristics tend to scale with device perimeter, indicated surface-related leakage, whereas for voltages greater than 16 V, the devices exhibit good scaling with area, indicating bulk-dominated effects. The point where the regime changes is the so-called punch-through voltage, V_p, corresponding to the voltage at which the undoped absorption layer becomes depleted. Under forward bias, the I-V curves scale well with area. A significant bending of the curve after $\sim$ 1.4 V indicates a non-negligible series resistance.

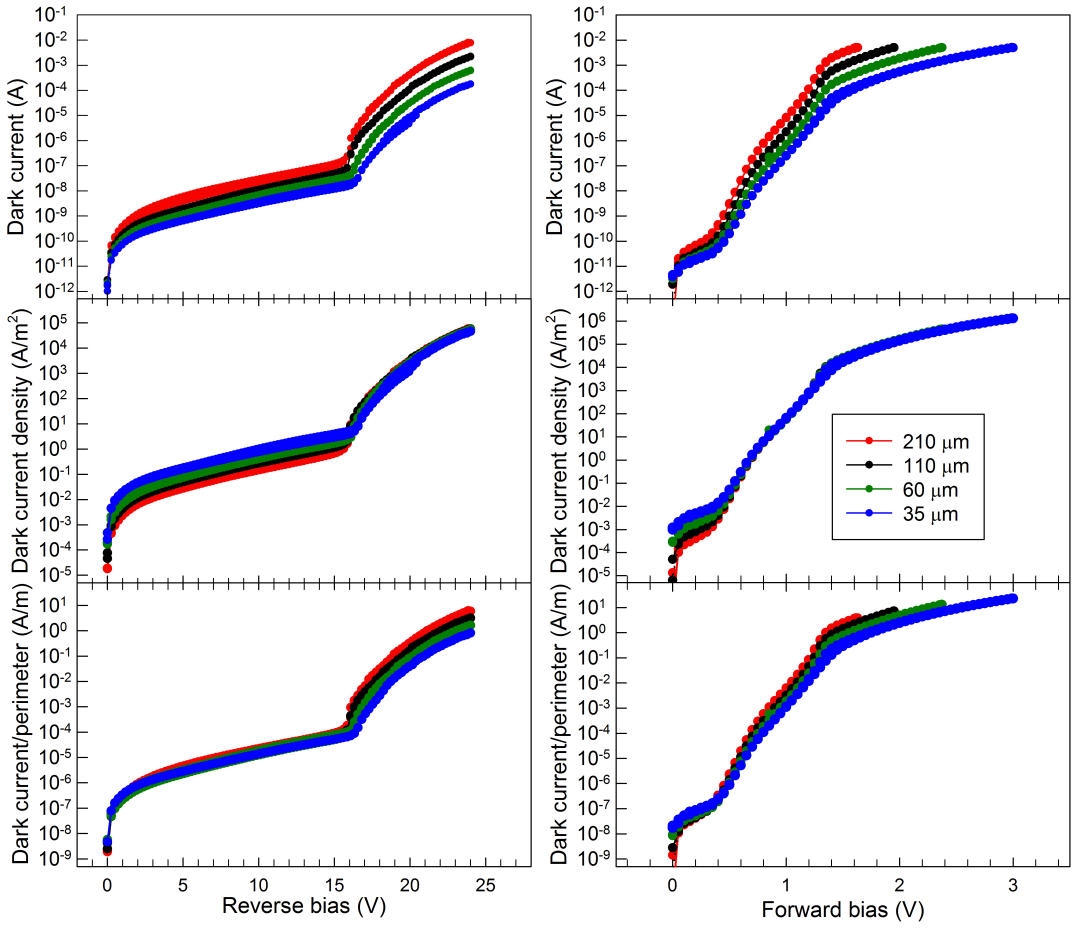

Figure 6.6: *Dark current at room temperature for devices of all four sizes. Scaling of dark currents with diode mesa area (middle) and perimeter (bottom) are also shown.*

C-V measurements were performed on the devices. Fig. 6.7 shows the C-V characteristics of a 110 μm diode. A sharp drop in the capacitance value at $\sim$ 15.9 V confirms the punch-through.

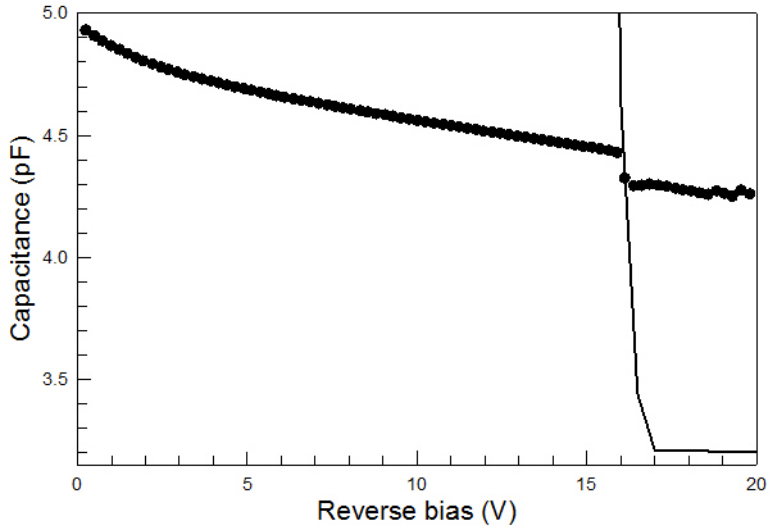

Figure 6.7: *Capacitance-Voltage characteristics for a 110 μm device. Symbols are experimental data, the line is the result of V_p modelling.*

An attempt to model the C-V with a single depletion region (the usual assumption) was not successful. This is attributed to unintentional background doping of opposite signs within the absorption and the avalanche regions. This results in depletion starting from several junctions across the wafer, and then joining when bias increases. This has already been observed in other wafers. In addition, after punch-through, the phase angle, indicating the quality of the C-V measurements drops significantly due to a high level of dark currents, the measured capacitance is therefore unreliable for further analyses. However, SIMS measurements from similar wafers showed that the thickness of the layers were well controlled during wafer growth, giving actual material layer thicknesses accurate to within 10 % variation from the nominal values. Nevertheless, the value of the punch-through voltage V_p is strongly dependent on the charge sheet thickness and doping, as well as the unintentional doping in the absorption and avalanche regions. The fact that the value of V_p is consistent from the I-V and the C-V measurements allows for a partial fitting of the C-V data. Values of thicknesses and doping in the C-V modelling programme were adjusted until the modelled V_p agreed with the experimental values,

as shown in Fig. 6.7. The thicknesses and doping values for the simulated layers are shown in Table 6.3.

Table 6.3: *Nominal and fitted values of thicknesses and doping of the SAM APD layers*

Layer	**Thickness (nm)**		**Doping (cm^{-3})**	
	Nominal	**Fitted**	**Nominal**	**Fitted**
InAlAs p^+ cladding	300	300	5.0×10^{18}	5.0×10^{18}
Grading	100	95	1.0×10^{15}	1.0×10^{15}
InGaAs absorber	1000	900	1.0×10^{15}	1.0×10^{15}
Grading	100	90	1.0×10^{15}	2.0×10^{15}
AlGaAsSb p^+ charge sheet	47	48	1.0×10^{18}	1.2×10^{18}
AlGaAsSb avalanche	100	100	1.0×10^{15}	1.0×10^{15}
AlGaAsSb n^+ cladding	200	200	-1.0×10^{18}	-5.0×10^{17}

From the values in Table 6.3, the electric field profile within the SAM APD can be estimated, as shown in Fig. 6.8. The figure shows that the electric field in the absorption region is lower than intended, whereas it is higher than designed in the avalanche region. This is due to a higher doping level than expected in the charge sheet. The charge sheet is also thought to be slightly thicker than designed. This exacerbates the difference in electric field values between the avalanche and the multiplication regions. Despite the very low calculated field in the absorption region, the devices still undergo a punch-through, as confirmed by the I-V and C-V data (Figs. 6.6 and 6.7). This shows the interest of the safety margin on the absorption layer electric field (designed to be higher than optimal to avoid incomplete depletion) described in part 6.1. In addition, the different grading layers on either side of the absorber are sensitive to impurities yielding unintentional doping. Table 6.3 actually shows a higher doping level than intended in one of the grading layers. The total thickness of each grading region (100 nm) is not negligible, making it difficult to control the electric field around the absorber. It would therefore be beneficial to the SAM APD to reduce the thickness of the grading layers. This should to be taken into consideration for future design.

6.3 Temperature dependence of dark currents

Temperature-dependant I-V and gain measurements were performed using a Janis ST-500 probe station (see part 3.4). The probe arms were connected to a

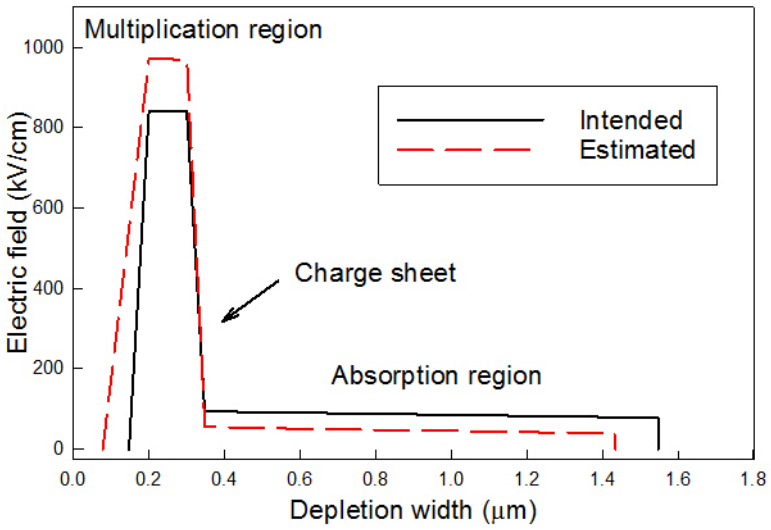

Figure 6.8: *Intended electric field profile (solid black line) and estimated field profile modelled from fitted values (dashed red line) at 22 V reverse bias*

KEITHLEY 2400 SMU for the measurements. The I-V curves are shown in Fig. 6.9.

For a given reverse bias, the dark current is found to reduce significantly with temperature. Between room temperature and 77 K, a reduction of 2-3 orders of magnitude is observed. The scaling between the different device sizes as discussed in part 6.2 is mostly retained down to 150 K. For even lower temperatures, the scaling is less good, due to the different temperature dependence of the leakage mechanisms involved. Note that dark current at higher reverse biases also drops significantly with temperature, indicating that band-to-band tunnelling current are not dominating, since according to Eq. 3.3 tunnelling currents are only weakly dependent on temperature. This is consistent with the low electric field value inside the absorption region deduced in part 6.2.

6.4 Temperature dependence of gain

The gain measurements were also carried out using the JANIS probe station. The devices were illuminated via the probe station fibre, with a 1550 nm semiconductor laser. In this part, five devices of radii 210 and 110 μm are measured. Note that given the wide bandgaps of InAlAs and AlGaAsSb (1.55 and 1.56 eV respectively), the 1550 nm laser light can only be absorbed in the InGaAs layer.

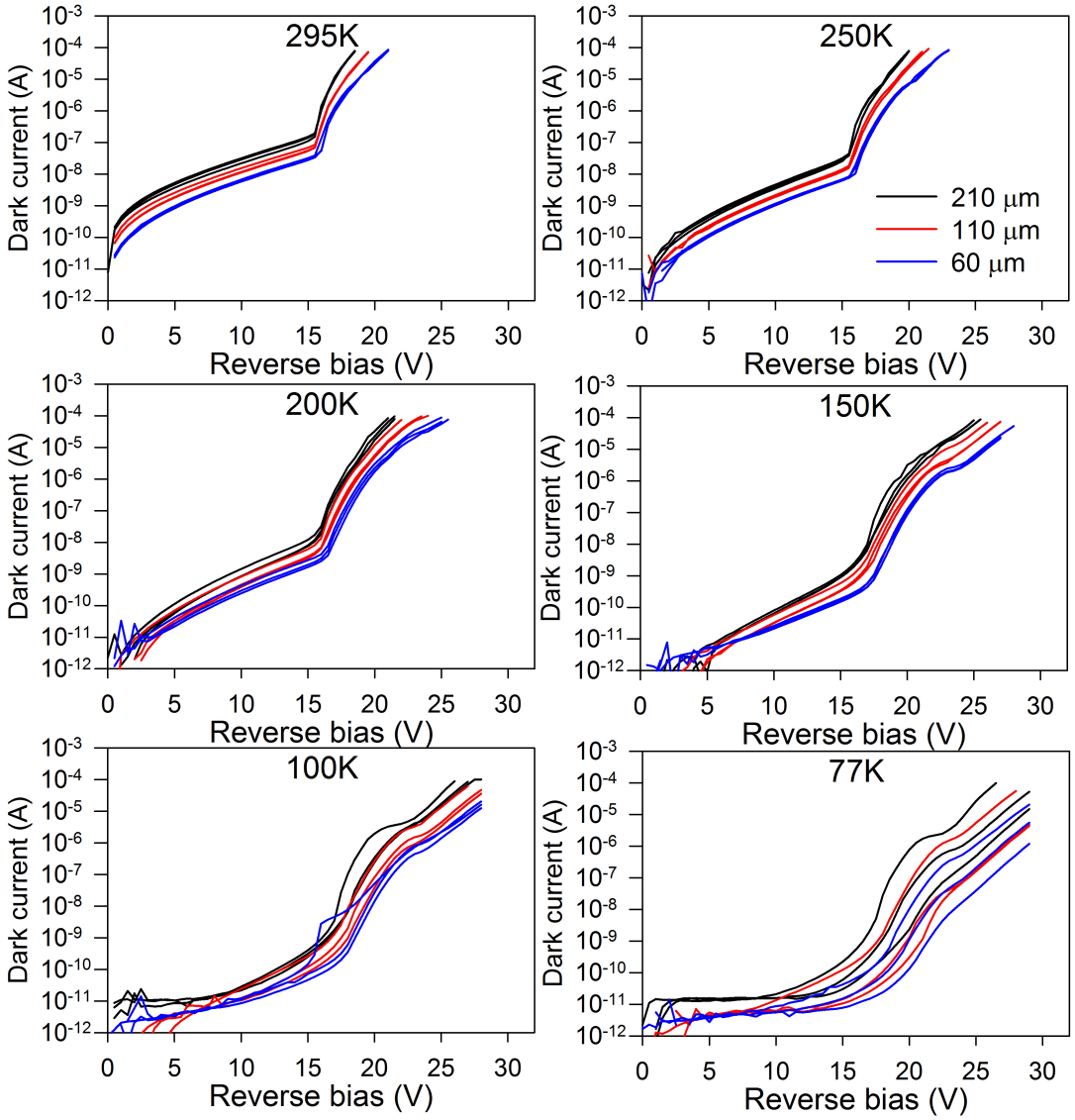

Figure 6.9: *Dark current characteristics of 60 (blue), 110 (red) and 210 µm (black) radii diodes at temperatures between 77 K and room temperature*

In an APD, the primary photocurrent will be multiplied by the gain. The total current from an illuminated diode is therefore

$$I_{tot} = M \times (I_d + I_{pr}). \tag{6.1}$$

There are two ways to measure the photocurrent, direct current (DC) and alternating current (AC) measurements.

The DC photoresponse is measured by shining a laser on the device using an optical fibre. The I-V characteristic is recorded in these conditions by a KEITHLEY

236 SMU. The photocurrent is the difference between this signal (total current) and the dark current of the device. This technique can only be used when the photocurrent is significantly larger than the dark current (several orders of magnitude). When dark and photocurrent are both high, their difference becomes less meaningful and this technique cannot be used.

When the dark current of the device is significant, the AC photocurrent is measured with the phase sensitive detection method, using a LIA. The laser beam is internally modulated at a frequency f, which is given as the reference frequency of the LIA. The LIA performs a low-noise voltage measurement across a load resistor R_L, taking only into account the signal at the frequency f, therefore excluding contributions other than the response to laser light. This measurement is more precise than the DC gain measurement described above, and should therefore be preferred.

Among the measured devices, two of them are selected for comparison, one of 210 μm radius, DEV 1, and one of 110 μm radius, DEV 2. The temperature dependence of dark current and DC photocurrent characteristics for these two devices are shown in Fig. 6.10.

Fig. 6.10 shows that no photocurrent is present before the structure is fully depleted (*i.e.* below V_p), since the total current is not distinguishable from the dark current. At the punch-through voltage, V_p, the absorption layer becomes depleted, and therefore the collection efficiency suddenly improves, giving a sudden rise in the photocurrent. V_p varies slightly from device to device, but stays within the 15.5-16.5 V range. For a given device, V_p seems to be independent of temperature. This indicates that the dopant activation and hence the electric field profile has not been affected by the decreasing temperature.

For the lowest two temperatures (77 K and 100 K), and to a lesser extent at 150 K, the increase in photocurrent around V_p becomes slightly less sharp. This can be attributed to the lower thermal energy of the electrons, that therefore have more difficulty to hop the energy barrier between the conduction band edges of the different layers (described in part 6.1).

After V_p, the total current ($I_d + I_{ph}$) increases slowly with voltage. Solely from DC measurements, it is hard to distinguish from the curve whether the devices show

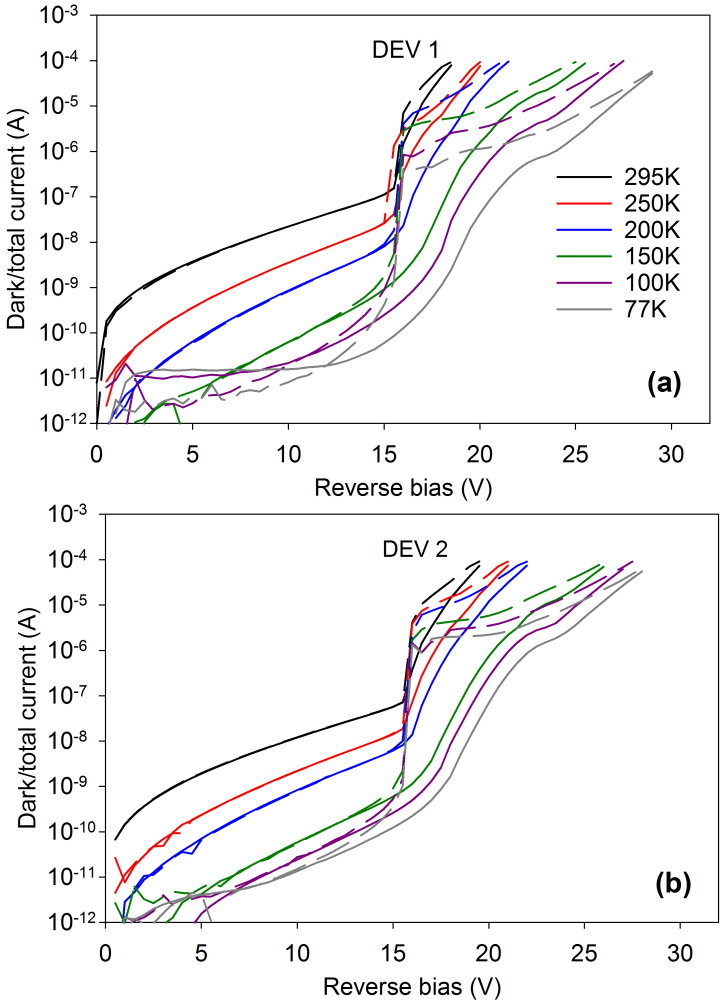

Figure 6.10: *Dark current (solid lines) and total current (I_d + I_{ph}) under 1550 nm illumination (dashed lines) for (a) DEV 1 and (b) DEV 2, for temperatures between 77 K and room temperature*

some gain, since both I_{tot} and I_d increase simultaneously. However, gain can be estimated using the following considerations.

For the lowest temperatures (77, 100, and 150 K), the photocurrent ($I_{tot} - I_d$) for most devices exhibit a flat region after V_p (for example in between V_p and $\sim$ 21 V at 150 K, and in between V_p and $\sim$ 24 V at 77 K). In this region, I_{ph} is constant, before the onset of gain. This region therefore defines the gain $M = 1$. For the higher temperatures (200, 250, and 295 K), this region of constant I_{ph} is not present, and the unity gain is simply taken to be at V_p. Therefore, for all devices and at all

temperatures, the gain is defined as

$$M(V) = \frac{I_{ph}(V)}{I_{ph}(V_p)}. \tag{6.2}$$

This is aided by the fact that V_p is sharp, and does not change with the temperature.

Photocurrent measurements were repeated using the phase-sensitive detection technique, and AC gain was calculated similarly. The results for all devices are shown in Fig. 6.11. It shows that the onset of gain seems to occur at higher voltages as temperature decreases. This is in contradiction to what is expected from AlGaAsSb behaviour [46].

Noticeably, the maximum gain obtained from AC measurements stays relatively low, around 4-6. This may seem a bit low to be of interest for practical devices. However, for this set of experiments, the current compliance within the diodes was set to 100 μA to prevent damage to the devices. The devices can however sustain higher currents, and consequently, higher gains could be obtained by increasing the current compliance, to allow for measurements at higher voltages. Also, the current compliance was kept the same for all temperatures for consistency. At lower temperature, the dark current is very low and therefore the photocurrent is dominant. Simply reducing the incident light power (set relatively high at a few 100 μW in the current measurements) would reduce the photocurrent below compliance, making it possible to work at higher voltages. Higher gains can therefore be expected, especially at lower temperatures, by reducing the incident light power and increasing the current compliance. With gains potentially higher than 6, the devices presented here are therefore of great interest for future applications.

For comparison, gain values deduced from DC and AC measurements for DEV 1 and DEV 2 are presented in Fig. 6.12. It can be seen that the DC gain is almost always overestimated. For the DC gain, some of the highest voltage points have been removed whenever I_{ph} is less than twice the value of I_d, where the experimental error would be large.

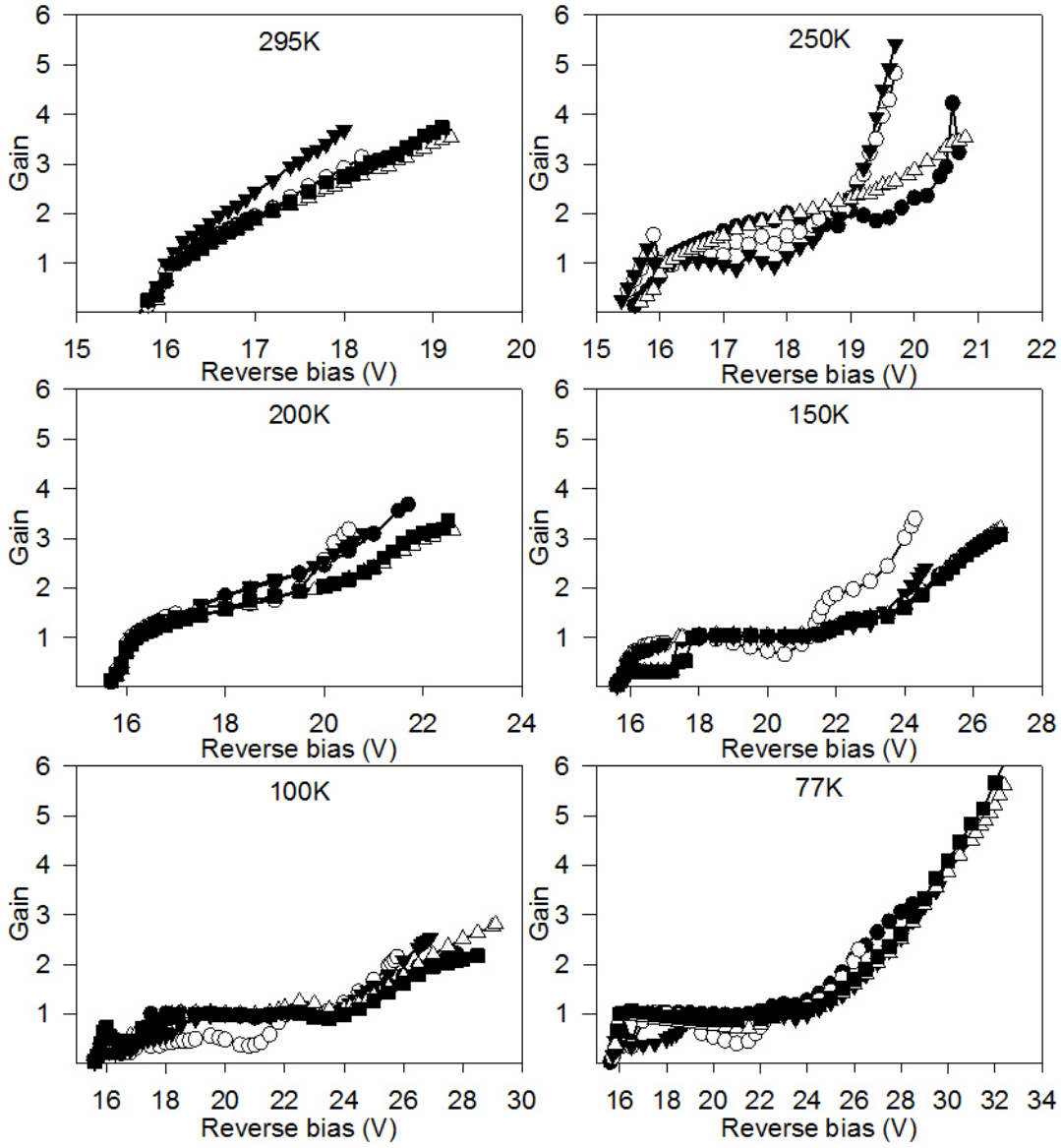

Figure 6.11: *Gain obtained by AC measurements, for temperatures between 77 and 295 K*

6.5 Discussion

To quantify the temperature dependence of gain, researchers often cite the temperature coefficient of breakdown voltage, C_{bd}, defined as the variation of V_b over the variation of temperature,

$$C_{bd} = \frac{\Delta V_b}{\Delta T}.$$

To determine the breakdown voltage, V_b, the values of $1/M$ are plotted versus reverse bias, and extrapolated to 0, as shown on Fig. 6.13. For clarity, only $1/M$

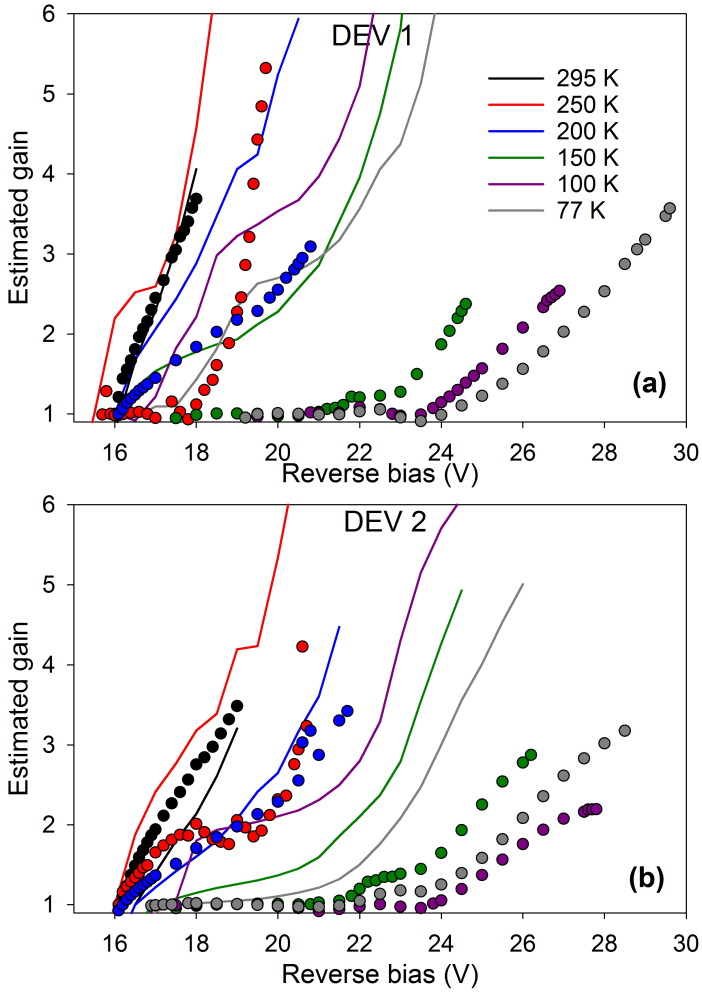

Figure 6.12: *AC (symbols) and DC (lines) gain of (a) DEV 1 and (b) DEV 2, for temperatures between 77 K and room temperature*

values for four temperatures (295, 200, 150, and 77 K) are plotted. Note that for each temperature, the fitting is done for the average value of $1/M$ of all devices. The highest voltage points are excluded from the fitting, since they correspond to higher currents, and can therefore be affected by series resistance (a bending of the curves can be noticed). The values of V_b are obtained by the intersection of the fitted line and the horizontal axis. V_b values extracted from Fig. 6.13 are compared in Table 6.4. Given the spread in gain values from device to device, an error of 5-8 % is associated with the values of V_b. Note that the gain being low, especially for the lowest temperatures, the fitting in Fig. 6.13 and the values in Table 6.4 are mostly indicative, and therefore are to be considered carefully. However, despite the uncertainty in values, the strong negative temperature dependence is clearly visible.

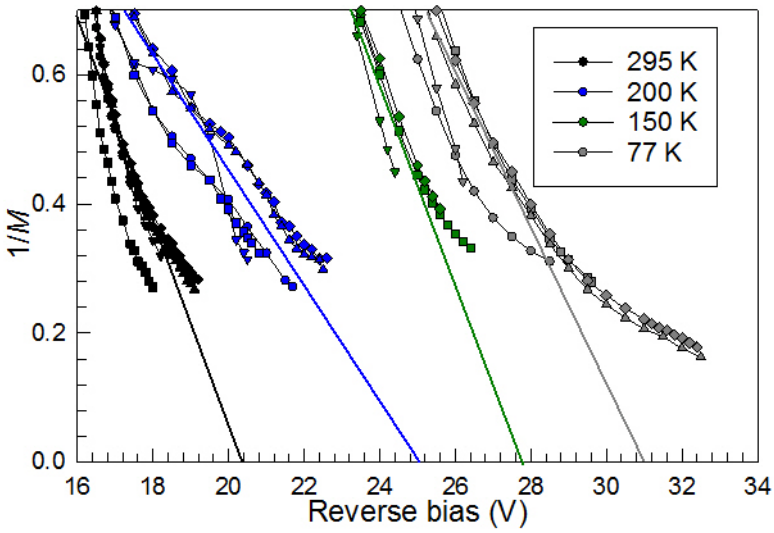

Figure 6.13: *Extrapolation of 1/M to 0 at temperatures of 295, 200, 150 and 77 K*

Table 6.4: *Extracted values of V_b at different temperatures*

Temperature (K)	V_b **(V)**
295	20.4
200	25.0
150	27.8
77	31.0

From the values in Table 6.4, the temperature coefficient of breakdown, C_{bd}, between 77 and 295 K is

$$C_{bd} = -49 \ \pm \ 4 \text{ mV/K}.$$

Due to the uncertainty in the determination of breakdown voltages, C_{bd} has an error margin of 8 %. This value is to be compared with a C_{bd} of +1.60 mV/K demonstrated in 100 nm AlGaAsSb *p-i-n* diodes [46]. Table 6.5 presents C_{bd} values of *p-i-n* diodes and SAM APDs for some relevant III-V materials. For a given material, C_{bd} is strongly dependant on the avalanche layer thickness.

In a 2013 paper, Xie *et al.* [42] observed that the C_{bd} of an InGaAs/AlAsSb SAM APD comprising a 50 nm AlAsSb avalanche region and a 500 nm InGaAs absorber was much larger than the C_{bd} of a simple homojunction AlAsSb *p-i-n* diode of $\sim$ 80 nm despite its thinner avalanche region (see Table 6.5). This shows that the InGaAs absorber has an influence on the overall C_{bd} of the SAM APD. In their case, the C_{bd} value of the SAM APD stayed positive.

Table 6.5: *C_{bd} values for relevant p-i-n diodes and SAM APDs*

AlGaAsSb [46]	100 nm *p-i-n*	+1.60 mV/K
InGaAs/AlGaAsSb (this work)	**AlGaAsSb 100 nm, InGaAs 1 μm**	**-49 mV/K**
AlAsSb [72]	200 nm *p-i-n*	+1.47 mV/K
	80 nm *p-i-n*	+0.95 mV/K
InGaAs/AlAsSb SAM APD [42]	AlAsSb 50 nm, InGaAs 500 nm	+8mV/K

For AlGaAsSb, as for the vast majority of semiconductors materials, V_b shows a positive temperature dependence, *i.e.* its value increases with temperature. This is because carriers will lose more energy to phonon scattering as the temperature increases, and therefore will have less energy to impact ionise. Unusually, Ng *et al.* demonstrated that InGaAs shows a negative temperature dependence of breakdown at low fields ($<$ 200 kV/cm) [73]. They showed that the electron ionisation coefficient α does actually decrease with temperature at electric fields below 200 kV/cm, whereas the hole coefficient β is only weakly affected by variations of temperature. Therefore, V_b increases when temperature decreases. Fig 6.14, taken from [73], illustrates this peculiar behaviour. Below a cross-over point (marked with a circle on the curves), the avalanche gain due to electron multiplication, M_e, decreases with temperature at a given voltage. For higher voltages, *i.e.* higher electric fields, M_e increases when the temperature decreases. The cross-over corresponds to an electric field around 200 kV/cm. This effect is not observed for the hole multiplication in *n-i-p* diodes, M_h, that varies monotonically and positively with temperature.

In the SAM APD studied in this chapter, Fig. 6.8 shows that due to the high doping in the charge sheet, the electric field in the InGaAs absorption region remains well below 200 kV/cm for a large range of reverse biases (contrary to the InGaAs/AlAsSb SAM APD demonstrated by Xie *et al.* discussed previously, where the electric field in the InGaAs absorption layer was estimated to be around 300 kV/cm, and thus retaining InGaAs' positive temperature dependence). For such low fields, impact ionisation events occurring in InGaAs will exhibit this negative temperature dependence shown by Ng *et al.* The narrow bandgap of InGaAs means that the ionisation threshold energies for the carriers are small, and therefore impact ionisation can still occur despite the low electric field maintained in the absorption region. The

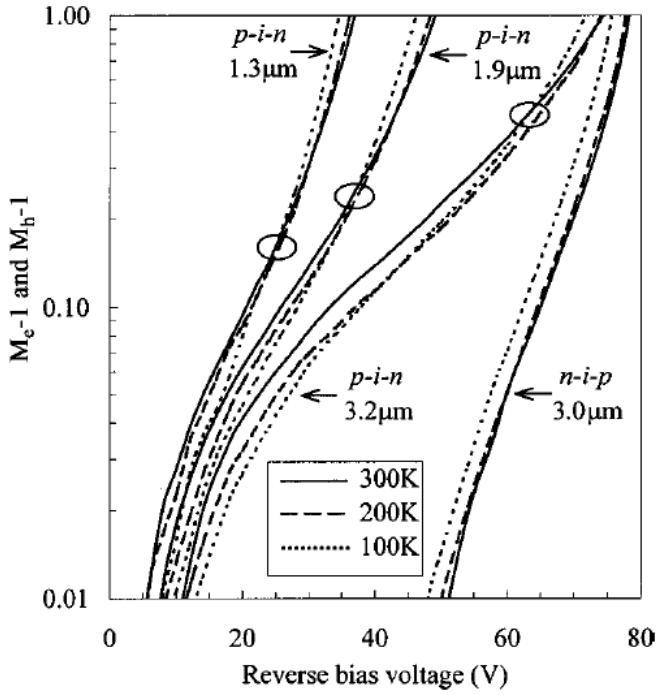

Figure 6.14: *Avalanche gain versus reverse bias voltage for InGaAs p-i-n and n-i-p diodes at 100, 200, and 300 K. The circle indicates the cross-over points for the 3 p-i-n diodes. Figure from [73].*

absorption region being ten times thicker than the avalanche region, the effect of InGaAs impact ionisation can actually become significant. This competition between impact ionisation in the InGaAs absorption layer and in the AlGaAsSb avalanche layer may explain the peculiar temperature dependence of gain observed in this SAM APD.

6.6 Conclusions

In this chapter, a SAM APD combining a 100 nm-thin AlGaAsSb avalanche region with a 1 μm-thick InGaAs absorption layer has been studied. The temperature dependences of dark current and gain have been reported. AC and DC gain measurements were compared, and the DC measurement technique was found to be less precise and to frequently yield overestimated gain values. A negative C_{bd} value of -49 mV/K has been obtained. The negative value means that the avalanche breakdown voltage increases when the temperature decreases, unlike the vast majority of semiconductors. This peculiar behaviour was attributed to impact ionisation occurring not only in

the avalanche layer, but also to some extent in the InGaAs absorption layer, since negative temperature dependence has been reported for InGaAs at electric fields below 200 kV/cm.

Chapter 7

Conclusion and future work

7.1 Summary of findings

In this thesis, low noise APDs have been studied. AlGaAsSb devices with thin avalanche regions have been investigated, and very low excess noise values have been reported. The influence of light absorption profile on the gain and noise of very low k_{eff} materials has been examined. In addition, a SAM APD combining AlGaAsSb as low noise avalanche material with InGaAs for absorption at telecommunication wavelengths has been studied.

Gain and excess noise of thin $Al_{0.85}Ga_{0.15}As_{0.56}Sb_{0.44}$ *p-i-n* and *n-i-p* diodes have been measured, for different carrier injection conditions. Very low excess noise values were obtained, corresponding to $k_{eff} \sim 0.08$ for the 200 nm *p-i-n* devices under pure electron injection. For the *p-i-n* diodes, avalanche gain decreases when moving from pure electron to mixed injection conditions, while excess noise increases. The opposite trend was observed in the *n-i-p* diodes, when moving from pure hole injection to mixed injection. This indicates that $\alpha > \beta$ in AlGaAsSb. It has been observed that, while k_{eff} values are larger in *n-i-p* devices than in *p-i-n* devices, the relationships between k_{eff} values in *p-i-n* and in *n-i-p* diodes do not follow McIntyre's local model theory. This indicates a significant dead-space effect in the devices, reducing the excess noise. Recurrence equations were used to quantify this dead-space effect, and to estimate the values of the ionisation coefficients α and β. Along with extensive electrical characterisations, material characterisations were also carried out. The four wafers were analysed using SIMS, to further determine their doping profiles.

Ion implantation in AlGaAsSb has been reported for the first time, and implanted samples were used to provide calibration for the SIMS measurements.

The study of low noise materials was continued with some theoretical work. Simulations using recurrence equations were carried out to simulate gain and excess noise characteristics in p-i-n diodes with $k_{eff} = 0.1$, 0.01, and 0.001, for different light injection profiles. The results confirmed that for mixed injection conditions, the $F(M)$ characteristics become higher than that for pure electron injection. However, for extremely low k_{eff} materials, the overall noise stays low even for the most severe case of mixed injection. The shape of $F(M)$ characteristics were investigated further using RPL model simulations to track the carriers initiating impact ionisation events in the case of pure electron injection. It was found that two different regimes can be defined. First, for gains lower than $\sim 1/k_{eff}$, most of the impact ionisation events are initiated by the carriers ionising more easily (electrons), and therefore the excess noise stays low. For gain above $\sim 1/k_{eff}$, more and more holes start to impact ionise to contribute to the gain, leading to a sharp rise of the $F(M)$ characteristics. Finally, figures of merits for optical detectors, the SNR and NEP, were calculated for low k_{eff} materials, highlighting the interest of using avalanche gain to increase the sensitivity of optical detectors, since avalanche gain reduces the effect of amplifier noise.

Finally, a SAM APD incorporating a thin (100 nm) AlGaAsSb avalanche layer and a thick (1000 nm) InGaAs absorber has been studied. Photocurrent and gain values were obtained under 1550 nm illumination (optical telecommunications wavelength). The devices showed a clear punch-through and exhibited avalanche gain, as well as reasonably small dark currents. The temperature dependence of gain, for temperatures between 77 K and room temperature was reported. A negative C_{bd} value of -49 mV/K was found, attributed to some amount of impact ionisation taking place inside the low-electric field InGaAs absorber. InGaAs is indeed known to have a negative temperature dependence for low electric fields, contrary to the vast majority of semiconductors.

7.2 Suggestions for future work

In Chap. 4, recurrence simulations have been used to estimate the ionisation coefficients of AlGaAsSb. The model used was that of *p-i-n* and *n-i-p* diodes with tapered electric field, implying a constant doping in each of the layers. The information provided from the SIMS characterisations in part 4.4 actually show a certain amount of dopant diffusion into the intrinsically doped layers, yielding a more rounded electric field profile. A fine fitting of the SIMS data for the PIN 1 wafer from Chap. 4 is presented in Fig. 7.1 (a). The fitting (blue dashed line) consists in dividing the device into 5 nm layers over which the doping assumes a constant value. The layer structure is then entered into a simulation programme outputting the electric field profile. The result is shown in Fig. 7.1 (b). It can be seen that the actual electric field inside the device is quite different from the tapered electric field profile assumed for the recurrence simulations in part 4.6. For such thin avalanche layers, small variations in the electric field profile may lead to a significant error in the ionisation coefficients. Therefore, for a precise determination of the ionisation coefficients, a Simple Monte Carlo model could be used. This model simulates precisely the scattering mechanism leading to impact ionisation. However, band structure parameters, carrier velocities, and phonon energies are required. Since these parameters are unknown at present, significant work would be required to experimentally measure these parameters. Also, if only pure injection data have been used in part 4.6, the results obtained for the two mixed injection cases (633 and 543 nm) could also be used, as they offer extra sets of data, useful for more precise simulations.

In addition, the AlGaAsSb ionisation coefficient values obtained in Chap. 4 are only valid within a limited range of electric fields, defined by the device widths. The 100 and 200 nm devices in combination cover a range from 500 kV/cm to 1.3 MV/cm approximately. The analytical expressions obtained for α and β cannot be assumed to be valid outside of the electric field range of study. To extend the range would require sets of *p-i-n* and *n-i-p* devices with thicker avalanche widths. The obtained α and β parameters shown in Fig. 4.11 show a large discrepancy at lower fields. If this trend extends towards lower fields, very small excess noise could be obtained for thicker avalanche regions, as it has been demonstrated in AlAsSb [74].

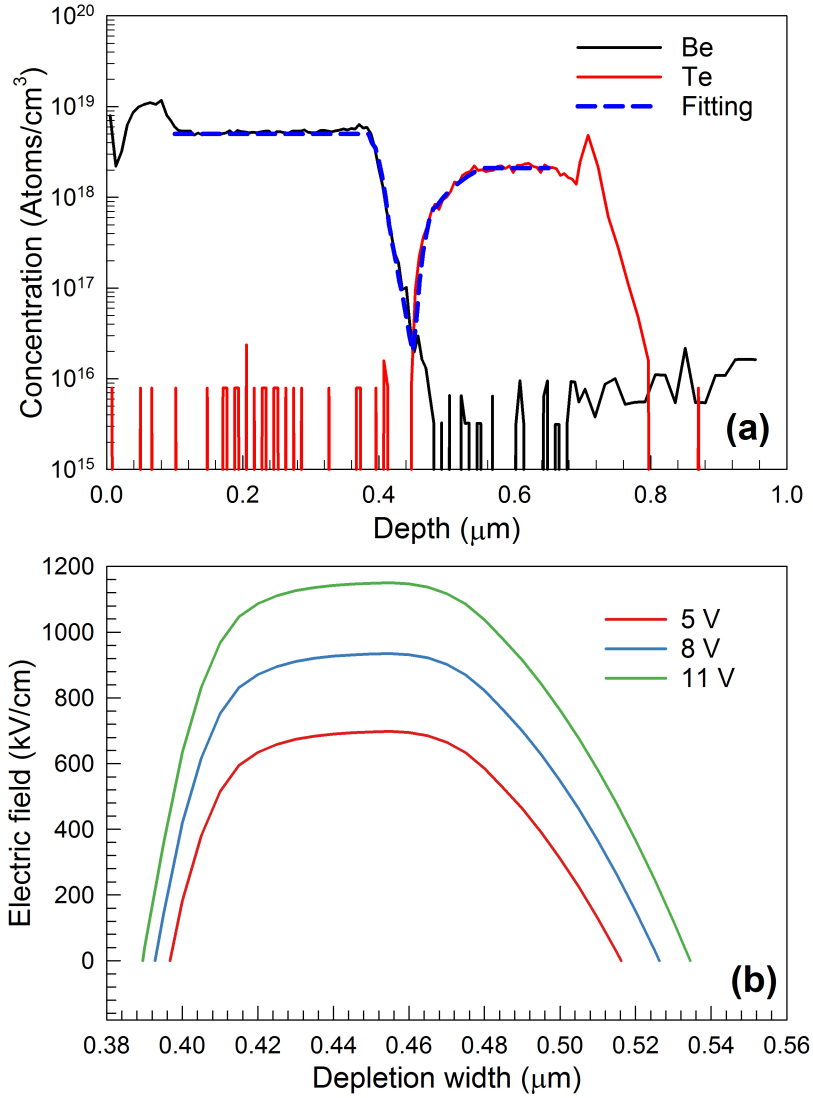

Figure 7.1: *(a) Fitted SIMS results and (b) modelled electric field profile from SIMS fitting, for PIN 1*

The unintentional background doping in semiconductor materials is due to contamination by impurities during growth, and cannot be controlled. In the case of the SAM APD in Chap. 6, the background doping in the avalanche layer and the one in the absorption layer were thought to be of different signs, preventing the full C-V analysis of the devices. This issue can be solved by intentionally doping slightly the intrinsic layers, to force the background doping to be of a certain sign. Structure of type p^+-p^--p^+-p^--n^+ can be thus obtained, ensuring only a single depletion junction inside the devices, starting from the p^--n^+ junction.

For SAM APDs, the thickness and doping of the charge sheet are critical. A

few percent error in their value can dramatically affect the electric field profile. Controlling the doping and the diffusion of doping atoms from the highly-doped charge sheet into adjacent lightly-doped layers is particularly challenging. To prevent impact ionisation in the low field absorption region, as it is the case in the devices studied in Chap. 6, more growth trials and better control over the doping in AlGaAsSb would be necessary.

In addition to the above considerations on doping, to bring the SAM APD studied in Chap. 6 closer to commercialisation, further optimisation would be required. For instance, as stated before, the undoped grading layers between the AlGaAsSb and the InGaAs layers could be made thinner to allow a greater control of the electric field around the absorption region. However, if there is some room for optimisation, the potential gains greater than 6 demonstrated are clearly encouraging, and the presented InGAs/AlGaAsSb SAM APD is therefore of good interest.

A solid set of data has been obtained for the characterisation of the InGaAs/AlGaAsSb SAM APD presented in Chap. 6. For a more complete and deepened understanding of the structure, excess noise measurements could also be performed, to study how the InGaAs absorber influences the overall excess noise.

Further developments on the InGaAs/AlGaAsSb SAM APD can include the design of planar diodes, since the vast majority of commercial devices use planar technology. In addition, it is possible to further lower dark current using planar technology. Planar devices are implanted instead of etched, and devices are defined by ion implantation pockets instead of physical mesas. Consequently, no mesa walls are created, and therefore the diodes do not present surface leakage. Fig. 7.2 shows a schematic of planar diodes realised by implantation. To obtain a planar *p*-*i*-*p*-*i*-*n* (respectively *n*-*i*-*p*-*i*-*p*) SAM APD, an *i*-*i*-*p*-*i*-*n* (*i*-*i*-*p*-*i*-*p*) structure needs to be grown, and the top intrinsic InGaAs layer needs to be *p*-doped (*n*-doped) by ion implantation. To avoid optical or electrical cross-talk between two adjacent devices, isolation trenches may be necessary to physically separate the devices.

The critical parameter in designing planar APDs is ion implantation. Numerous implantation studies are required to find the right implantation conditions, and yield the right doping profile for the implanted layer. Implantation trials and electric field simulations are needed to obtain good devices with well-confined electric field

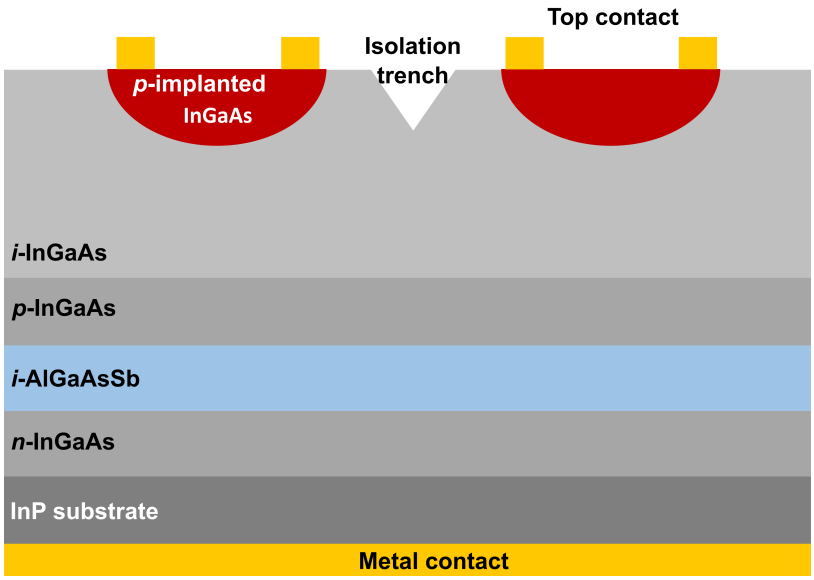

Figure 7.2: *Planar p-i-p-i-n diodes obtained by ion implantation into a thick undoped InGaAs layer*

(no leak into adjacent devices or bulk). Thermal treatment may also be required after implant to further diffuse dopants and passivate defects introduced by the implantation process. All this requires a long optimisation process. The implant trials done in Chap. 4 for SIMS analysis should thus be repeated with InGaAs. This approach also requires the design of new implant and lithography masks.

References

[1] R. J. McIntyre, "Multiplication noise in uniform avalanche diodes," *IEEE Transactions on Electron Devices*, no. 1, pp. 164–168, 1966.

[2] R. B. Gomes, C. H. Tan, J. E. Lees, J. P. R. David, and J. S. Ng, "Effects of Dead Space on Avalanche Gain Distribution of X-Ray Avalanche Photodiodes," *IEEE Transactions on Electron Devices*, vol. 59, no. 4, pp. 1063–1067, Apr. 2012.

[3] D. S. Ong, K. F. Li, G. J. Rees, J. P. R. David, and P. N. Robson, "A simple model to determine multiplication and noise in avalanche photodiodes," *Journal of Applied Physics*, vol. 83, no. 6, pp. 3426–3428, 1998.

[4] M. M. Hayat, B. E. A. Saleh, and M. C. Teich, "Effect of dead space on gain and noise of double-carrier-multiplication avalanche photodiodes," *IEEE Transactions on Electron Devices*, vol. 39, no. 3, pp. 546–552, Mar. 1992.

[5] C. H. Tan, J. P. R. David, G. J. Rees, R. C. Tozer, and D. C. Herbert, "Treatment of soft threshold in impact ionization," *Journal of Applied Physics*, vol. 90, no. 5, pp. 2538–2543, 2001.

[6] M. A. Saleh, M. M. Hayat, P. P. Sotirelis, A. L. Holmes, J. C. Campbell, B. E. A. Saleh, and M. C. Teich, "Impact-ionization and noise characteristics of thin III-V avalanche photodiodes," *IEEE Transactions on Electron Devices*, vol. 48, no. 12, pp. 2722–2731, Dec. 2001.

[7] D. S. Ong, K. F. Li, G. J. Rees, J. P. R. David, and P. N. Robson, "A simple model to determine multiplication and noise in avalanche photodiodes," *Journal of Applied Physics*, vol. 83, no. 6, pp. 3426–3428, 1998.

[8] M. V. Fischetti, "Monte Carlo simulation of transport in technologically significant semiconductors of the diamond and zinc-blende structures. I. Homogeneous transport," *IEEE Transactions on Electron Devices*, vol. 38, no. 3, pp. 634–649, 1991.

[9] K. Y. Choo and D. S. Ong, "Analytical band Monte Carlo simulation of electron impact ionization in $In_{0.53}Ga_{0.47}As$," *Journal of Applied Physics*, vol. 96, no. 10, pp. 5649–5653, Nov. 2004.

[10] S. A. Plimmer, J. P. R. David, D. S. Ong, and K. F. Li, "A simple model for avalanche multiplication including deadspace effects," *IEEE Transactions on Electron Devices*, vol. 46, no. 4, pp. 769–775, 1999.

[11] X. Zhou, J. S. Ng, and C. H. Tan, "A simple Monte Carlo model for prediction of avalanche multiplication process in Silicon," *Journal of Instrumentation*, vol. 7, no. 08, p. P08006, 2012.

[12] Hamamatsu, "InGaAs APDs - G8931 series," Sep. 2017.

[13] Thorlabs, "InGaAs photodiode - FGA10," Feb. 2017.

[14] N. Susa, H. Nakagome, H. Ando, and H. Kanbe, "Characteristics in InGaAs/InP avalanche photodiodes with separated absorption and multiplication regions," *IEEE Journal of Quantum Electronics*, vol. 17, no. 2, pp. 243–250, 1981.

[15] R. B. Emmons, "Avalanche-Photodiode Frequency Response," *Journal of Applied Physics*, vol. 38, no. 9, pp. 3705–3714, Aug. 1967.

[16] R. Van Overstraeten and H. De Man, "Measurement of the ionization rates in diffused silicon *p-n* junctions," *Solid State Electronics*, vol. 13, pp. 583–608, May 1970.

[17] M. H. Woods, W. C. Johnson, and M. A. Lampert, "Use of a Schottky barrier to measure impact ionization coefficients in semiconductors," *Solid-State Electronics*, vol. 16, no. 3, pp. 381–394, Mar. 1973.

[18] T. Kaneda, H. Matsumoto, and T. Yamaoka, "A model for reach-through avalanche photodiodes (RAPD's)," *Journal of Applied Physics*, vol. 47, no. 7, pp. 3135–3139, 1976.

[19] V. M. Robbins, T. Wang, K. F. Brennan, K. Hess, and G. E. Stillman, "Electron and hole impact ionization coefficients in (100) and in (111) Si," *Journal of Applied Physics*, vol. 58, no. 12, pp. 4614–4617, 1985.

[20] J. S. Ng, C. H. Tan, J. P. R. David, G. Hill, and G. J. Rees, "Field dependence of impact ionization coefficients in $In_{0.53}Ga_{0.47}As$," *IEEE Transactions on Electron Devices*, vol. 50, no. 4, pp. 901–905, April 2003.

[21] A. Marshall, Chee Hing Tan, M. Steer, and J. David, "Extremely low excess noise in InAs electron avalanche photodiodes," *IEEE Photonics Technology Letters*, vol. 21, no. 13, pp. 866–868, Jul. 2009.

[22] F. Capasso, W. Tsang, A. Hutchinson, and G. Williams, "The superlattice photodetector: A new avalanche photodiode with a large ionization rates ratio," in *International Electron Devices Meeting, 1981*, vol. 27, 1981, pp. 284–287.

[23] M. Ren, S. Maddox, Y. Chen, M. Woodson, J. C. Campbell, and S. Bank, "AlInAsSb/GaSb staircase avalanche photodiode," *Applied Physics Letters*, vol. 108, no. 8, p. 081101, 2016.

[24] G. J. Rees and J. P. R. David, "Nonlocal impact ionization and avalanche multiplication," *Journal of Physics D: Applied Physics*, vol. 43, no. 24, p. 243001, Jun. 2010.

[25] C. H. Tan, J. C. Clark, J. P. R. David, G. J. Rees, S. A. Plimmer, R. C. Tozer, D. C. Herbert, D. J. Robbins, W. Y. Leong, and J. Newey, "Avalanche noise measurement in thin Si p^+-i-n^+ diodes," *Applied Physics Letters*, vol. 76, no. 26, pp. 3926–3928, Jun. 2000.

[26] P. Yuan, C. C. Hansing, K. A. Anselm, C. V. Lenox, H. Nie, A. L. Holmes, B. G. Streetman, and J. C. Campbell, "Impact ionization characteristics of III-V semiconductors for a wide range of multiplication region thicknesses," *IEEE Journal of Quantum Electronics*, vol. 36, no. 2, pp. 198–204, 2000.

[27] Y. L. Goh, A. R. J. Marshall, D. J. Massey, J. S. Ng, C. H. Tan, M. Hopkinson, J. P. R. David, S. K. Jones, C. C. Button, and S. M. Pinches, "Excess Avalanche Noise in $In_{0.52}Al_{0.48}As$," *IEEE Journal of Quantum Electronics*, vol. 43, no. 6, pp. 503–507, Jun. 2007.

[28] C. H. Tan, J. P. R. David, S. A. Plimmer, G. J. Rees, R. C. Tozer, and R. Grey, "Low multiplication noise thin $Al_{0.6}Ga_{0.4}As$ avalanche photodiodes," *IEEE Transactions on Electron Devices*, vol. 48, no. 7, pp. 1310–1317, July 2001.

[29] J. Xie, S. Xie, R. C. Tozer, and C. H. Tan, "Excess Noise Characteristics of Thin AlAsSb APDs," *IEEE Transactions on Electron Devices*, vol. 59, no. 5, pp. 1475–1479, May 2012.

[30] M. Ren, S. J. Maddox, M. E. Woodson, Y. Chen, S. R. Bank, and J. C. Campbell, "Characteristics of $Al_xIn_{1-x}As_ySb_{1-y}$ Avalanche Photodiodes (x:0.3-0.7)," *Journal of Lightwave Technology*, vol. 35, no. 12, pp. 2380–2384, Jun. 2017.

[31] J. C. Campbell, W. T. Tsang, G. J. Qua, and B. C. Johnson, "High-speed InP/InGaAsP/InGaAs avalanche photodiodes grown by chemical beam epitaxy," *IEEE Journal of Quantum Electronics*, vol. 24, no. 3, pp. 496–500, March 1988.

[32] Y. Ai-Wen, W. Ren-Fan, X. Bing, and S. Jing, "Fabrication of a 10 Gb/s InGaAs/InP avalanche photodiode with an AlGaInAs/InP distributed Bragg reflector," *Chinese Physics Letters*, vol. 30, no. 3, p. 038501, 2013.

[33] L. E. Tarof, J. Yu, R. Bruce, D. G. Knight, T. Baird, and B. Oosterbrink, "High-frequency performance of separate absorption grading, charge, and multiplication InP/InGaAs avalanche photodiodes," *IEEE Photonics Technology Letters*, vol. 5, no. 6, pp. 672–674, June 1993.

[34] T. Nakata, T. Takeuchi, I. Watanabe, K. Makita, and T. Torikai, "10 Gbit/s high sensitivity, low-voltage-operation avalanche photodiodes with thin InAlAs multiplication layer and waveguide structure," *Electronics Letters*, vol. 36, no. 24, pp. 2033–2034, 2000.

[35] S. Xie, S. Zhang, and C. H. Tan, "InGaAs/InAlAs avalanche photodiode with low dark current for high-speed operation," *IEEE Photonics Technology Letters*, vol. 27, no. 16, pp. 1745–1748, Aug. 2015.

[36] C. Lenox, H. Nie, P. Yuan, G. Kinsey, A. L. Homles, B. G. Streetman, and J. C. Campbell, "Resonant-cavity InGaAs-InAlAs avalanche photodiodes with gain-bandwidth product of 290 GHz," *IEEE Photonics Technology Letters*, vol. 11, no. 9, pp. 1162–1164, Sept 1999.

[37] R. E. Warburton, G. Intermite, M. Myronov, P. Allred, D. R. Leadley, K. Gallacher, D. J. Paul, N. J. Pilgrim, L. J. M. Lever, Z. Ikonic, R. W. Kelsall, E. Huante-Cerón, A. P. Knights, and G. S. Buller, "Ge-on-Si single-photon avalanche diode detectors: Design, modeling, fabrication, and characterization at wavelengths 1310 and 1550 nm," *IEEE Transactions on Electron Devices*, vol. 60, no. 11, pp. 3807–3813, Nov 2013.

[38] M. Huang, S. Li, P. Cai, G. Hou, T. Su, W. Chen, C. Hong, and D. Pan, "Germanium on silicon avalanche photodiode," *IEEE Journal of Selected Topics in Quantum Electronics*, vol. 24, no. 2, pp. 1–11, March 2018.

[39] Y. Kang, H.-D. Liu, M. Morse, M. J. Paniccia, M. Zadka, S. Litski, G. Sarid, A. Pauchard, Y.-H. Kuo, H.-W. Chen, W. S. Zaoui, J. E. Bowers, A. Beling, D. C. McIntosh, X. Zheng, and J. C. Campbell, "Monolithic germanium/silicon avalanche photodiodes with 340 GHz gain–bandwidth product," *Nature Photonics*, vol. 3, no. 1, pp. 59–63, Jan. 2009.

[40] W. C. Dash and R. Newman, "Intrinsic optical absorption in single-crystal Germanium and Silicon at 77°K and 300°K," *Physical Review*, vol. 99, no. 4, pp. 1151–1155, Aug. 1955.

[41] C. H. Tan, S. Xie, and J. Xie, "Low noise avalanche photodiodes incorporating a 40 nm AlAsSb avalanche region," *IEEE Journal of Quantum Electronics*, vol. 48, no. 1, pp. 36–41, Jan. 2012.

[42] J. Xie, J. S. Ng, and C. H. Tan, "An InGaAs/AlAsSb avalanche photodiode with a small temperature coefficient of breakdown," *IEEE Photonics Journal*, vol. 5, no. 4, p. 6800706, Aug. 2013.

[43] S. Xie, X. Zhou, S. Zhang, D. J. Thomson, X. Chen, G. T. Reed, J. S. Ng, and C. H. Tan, "InGaAs/AlGaAsSb avalanche photodiode with high gain-bandwidth product," *Optics Express*, vol. 24, no. 21, pp. 24 242–24 247, 2016.

[44] X. Zhou, S. Zhang, J. P. R. David, J. S. Ng, and C. H. Tan, "Avalanche breakdown characteristics of $Al_{1-x}Ga_xAs_{0.56}Sb_{0.44}$ quaternary alloys," *IEEE Photonics Technology Letters*, vol. 28, no. 22, pp. 2495–2498, Nov. 2016.

[45] S. K. Mathis, K. H. A. Lau, A. M. Andrews, E. M. Hall, G. Almuneau, E. L. Hu, and J. S. Speck, "Lateral oxidation kinetics of AlAsSb and related alloys lattice matched to InP," *Journal of Applied Physics*, vol. 89, no. 4, pp. 2458–2464, 2001.

[46] S. Abdullah, C. H. Tan, X. Zhou, S. Zhang, L. Pinel, and J. S. Ng, "Investigation of temperature and temporal stability of AlGaAsSb avalanche photodiodes," *Optics Express*, vol. 25, no. 26, pp. 33 610–33 616, Dec. 2017.

[47] S. M. Sze and K. K. Ng, *Physics of semiconductor devices*, 3rd ed. Wiley-Interscience, 2007.

[48] S. R. Forrest, R. F. Leheny, R. E. Nahory, and M. A. Pollack, "$In_{0.53}Ga_{0.47}As$ photodiodes with dark current limited by generation-recombination and tunneling," *Applied Physics Letters*, vol. 37, no. 3, pp. 322–325, 1980.

[49] K. F. Li, D. S. Ong, J. P. David, G. J. Rees, R. C. Tozer, P. N. Robson, and R. Grey, "Avalanche multiplication noise characteristics in thin GaAs p^+-i-n^+ diodes," *IEEE Transactions on Electron Devices*, vol. 45, no. 10, pp. 2102–2107, 1998.

[50] Centronic, "High speed detectors (BPX65)."

[51] K. F. Li, "Avalanche noise in submicron GaAs and InP structures," PhD thesis, University of Sheffield, 1999.

[52] X. Zhou, L. L. G. Pinel, S. J. Dimler, S. Zhang, J. S. Ng, and C. H. Tan, "Thin $Al_{1-x}Ga_xAs_{0.56}Sb_{0.44}$ Diodes With Low Excess Noise," *IEEE Journal of Selected Topics in Quantum Electronics*, vol. 24, no. 2, p. 3800105, 2018.

[53] J. F. Ziegler, M. D. Ziegler, and J. P. Biersack, "SRIM - The stopping and range of ions in matter (2010)," *Nuclear Instruments and Methods in Physics Research B*, vol. 268, pp. 1818–1823, Jun. 2010.

[54] "Fiber-Coupled LED, M420F2," Thorlabs, 2017.

[55] M. R. Lorenz, R. Chicotka, G. D. Pettit, and P. J. Dean, "The fundamental absorption edge of AlAs and AlP," *Solid State Communications*, vol. 8, no. 9, pp. 693–697, 1970.

[56] S. Zollner, C. Lin, E. Schönherr, A. Böhringer, and M. Cardona, "The dielectric function of AlSb from 1.4 to 5.8 eV determined by spectroscopic ellipsometry," *Journal of Applied Physics*, vol. 66, no. 1, pp. 383–387, Jul. 1989.

[57] S. Adachi, "Optical dispersion relations for GaP, GaAs, GaSb, InP, InAs, InSb, $Al_xGa_{1-x}As$, and $In_{1-x}Ga_xAs_yP_{1-y}$," *Journal of Applied Physics*, vol. 66, no. 12, pp. 6030–6040, Dec. 1989.

[58] F. L. Schuermeyer, P. Cook, E. Martinez, and J. Tantillo, "Band-edge alignment in heterostructures," *Applied Physics Letters*, vol. 55, no. 18, pp. 1877–1878, Oct. 1989.

[59] Y. Nakata, Y. Sugiyama, T. Inata, O. Ueda, S. Sasa, S. Muto, and T. Fujii, "InGaAs/AlAsSb Heterostructures Lattice-Matched to InP Grown by Molecular Beam Epitaxy," in *Materials Research Society Proceedings*, vol. 198, 1990, pp. 289–294.

[60] L. W. Cook, G. E. Bulman, and G. E. Stillman, "Electron and hole impact ionization coefficients in InP determined by photomultiplication measurements," *Applied Physics Letters*, vol. 40, no. 7, pp. 589–591, Apr. 1982.

[61] A. R. Pauchard, P.-A. Besse, and R. S. Popovic, "Dead space effect on the wavelength dependence of gain and noise in avalanche photodiodes," *IEEE Transactions on Electron Devices*, vol. 47, no. 9, pp. 1685–1693, 2000.

[62] T. Pearsall and M. Pollack, "Compound semiconductor photodiodes," in *Lightwave Communications Technology*, ser. Semiconductors and Semimetals. Elsevier, 1985, vol. 22, pp. 173–245.

[63] S.-T. Chou, S.-H. Huang, Z.-H. Hong, and W.-Z. Chen, "A 40 Gbps optical receiver analog front-end in 65 nm CMOS," in *2012 IEEE International Symposium on Circuits and Systems*, Seoul, South Korea, May 2012, pp. 1736–1739.

[64] A. F. Ponchet, E. M. Bastida, R. R. Panepucci, and J. W. Swart, "Low noise Si based monolithic transimpedance amplifiers for 10 Gbps, 40 Gbps and 100 Gbps applications," in *2014 International Caribbean Conference on Devices, Circuits and Systems (ICCDCS)*, April 2014, pp. 1–6.

[65] J.-D. Jin and S. S. H. Hsu, "A 40-Gb/s transimpedance amplifier in 0.18-μm CMOS technology," *IEEE Journal of Solid-State Circuits*, vol. 43, no. 6, pp. 1449–1457, Jun. 2008.

[66] M. N. Ahmed, J. Chong, and D. S. Ha, "A 100 Gb/s transimpedance amplifier in 65 nm CMOS technology for optical communications," in *2014 IEEE International Symposium on Circuits and Systems (ISCAS)*, June 2014, pp. 1885–1888.

[67] S. Pellegrini, R. Warburton, L. Tan, J. Ng, A. Krysa, K. Groom, J. David, S. Cova, M. Robertson, and G. Buller, "Design and performance of an InGaAs/InP single-photon avalanche diode detector," *IEEE Journal of Quantum Electronics*, vol. 42, no. 4, pp. 397–403, Apr. 2006.

[68] D. A. Humphreys, R. J. King, D. Jenkins, and A. J. Moseley, "Measurement of absorption coefficients of $Ga_{0.47}In_{0.53}As$ over the wavelength range 1.0-1.7 μm," *Electronics Letters*, vol. 21, no. 25, pp. 1187–1189, Dec 1985.

[69] J. S. Ng, "Impact ionisation measurement and modelling of long wavelength avalanche photodiodes," PhD thesis, University of Sheffield, 2003.

[70] S. Selmic, T.-M. Chou, J. Sih, J. Kirk, A. Mantle, J. Butler, D. Bour, and G. Evans, "Design and characterization of 1.3-μm AlGaInAs-InP multiple-quantum-well lasers," *IEEE Journal of Selected Topics in Quantum Electronics*, vol. 7, no. 2, pp. 340–349, 2001.

[71] M. S. Hybertsen, "Band offset transitivity at the InGaAs/InAlAs/InP(001) heterointerfaces," *Applied Physics Letters*, vol. 58, no. 16, pp. 1759–1761, Apr. 1991.

[72] S. Xie and C. H. Tan, "AlAsSb avalanche photodiodes with a sub-mv/K temperature coefficient of breakdown voltage," *IEEE Journal of Quantum Electronics*, vol. 47, no. 11, pp. 1391–1395, Nov. 2011.

[73] W. K. Ng, C. H. Tan, J. P. R. David, P. A. Houston, M. Yee, and J. S. Ng, "Temperature dependent low-field electron multiplication in $In_{0.53}Ga_{0.47}As$," *Applied Physics Letters*, vol. 83, no. 14, pp. 2820–2822, 2003.

[74] X. Yi, S. Xie, B. Liang, L. W. Lim, X. Zhou, M. C. Debnath, D. L. Huffaker, C. H. Tan, and J. P. R. David, "Demonstration of large ionization coefficient ratio in $AlAs_{0.56}Sb_{0.44}$ lattice matched to InP," *Scientific Reports*, vol. 8, no. 1, pp. 1–6, Jun. 2018.